Slow Atomic Beams Manipulation with Magnetic Videotapes

Dissertation

zur

Erlangung des Doktorgrades (Dr. rer. nat.)

der

Mathematisch-Naturwissenschaftlichen Fakultät

der

Rheinischen Friedrich-Wilhelms-Universität Bonn

vorgelegt von

Habib Mérimèche

aus

Mulhouse (Frankreich)

Bonn 2004

Angefertigt mit Genehmigung der Mathematisch-Naturwissenschaftlichen Fakultät

der Rheinischen Friedrich-Wilhelms-Universität Bonn

1. Referent: Prof. Dr. Dieter Meschede
2. Referent: Prof. Dr. Eberhard Klempt

Tag der Promotion: 4. März 2004

Abstract

Laser cooling methods provide the possibility to obtain very well collimated and slow atomic beams. These intense sources have attracted new interest in the manipulation of atomic trajectories. Atom optical schemes based on the optical dipole force are very attractive, for example in atom lithography where atomic beams are focused by standing wave light fields, to create periodic nanostructures. However, in applications where more complex structures are desirable or decoherence due to spontaneous emission has to be avoided, magnetic atom optical components are more attractive.
For example, flat and curved atomic mirrors with high reflectivity and low surface roughness can be built from periodically magnetized videotapes.
First, with a collimated and polarized cesium atomic beam from a Zeeman-slower apparatus, we have investigated the deflection of the atomic beam by a sinusoidally magnetized videotape with a period length of 30 μm. From these measurements we have determined the magnetic field strength at the surface to be 0.05 Tesla. The reflectivity has been found to be consistent with 100%. The very large field gradients produced by the tape can be exploited to guide atoms on curved trajectories with small radii of curvature. With a radius of 9.5 cm we have obtained a maximum deflection angle of 25° which is limited by technical constraint.
Second, we have built a setup based on a $2D$-MOT for generating a slow atomic beam with a velocity of 20 m/s. After leaving the optical collimation and the optical polarization stages, the atomic beam is reflected after one bounce onto the videotape up to angles as large as 7°. We exploited the natural curvature of our videotape and we demonstrated the focusing of the atomic beam after one and two bounces depending on the curvature of the videotape. The focal length and the angles of deflection enable to deduce the local radii of curvature. We have confronted our results by testing the focusing of the videotape with a red laser and by performing a numerical simulation which prove the consistency with the atomic beam experiments.

Contents

Chapter 1

Introduction

The manipulation of atomic beams dates back to the famous experiment carried out in the 1920s by Stern and Gerlach [1] to probe the spin of an atomic beam deflected by inhomogeneous magnetic fields. Few years later, Frisch succeeded in deflecting a beam of atoms with light [2]. However, most of experiments faced difficulties essentially due to the thermal velocity of atoms. The construction of refractive atom optical elements based on permanent magnets in the 1950s was exploited by focusing a beam of atoms with a hexapole lens [3], producing however long focal lengths and very strong chromatic aberrations. A revival appeared in the early 1980s thanks to laser cooling which allows a precise control and manipulation of atomic motions.
The field of atom optics has now a wide range of applications [4]. Among them, the imaging with atomic beams requires the development of components analogous to those of classical optics, including mirrors, lenses and beam-splitters. Although the reflection of an atomic beam from a solid surface [5] and the diffraction of atomic waves through microfabricated structures [6, 7] have been reported, most of components are based on magnetic or electric effects. Laser lights have successfully reflected [8] and focused [9] atomic beams. The use of the light force as a tool for atom optics is reviewed for example in [10, 11]. In this approach the difficulty to achieve adequate light intensity limits the components to small apertures. In order to overcome this problem, components with active area originating from inhomogeneous magnetic fields offer a suitable alternative. They have also the great advantage to be stable and free from spontaneous emission. Imaging with atomic beams with magnetic lens have been successfully realized [12, 13].

It is well-known that reflective optics eliminates chromatic aberrations compared with refractive optics, for example patterns produced with conventional lithography result from the reflection of light on reflective components. In this context, in the last decade reflective atom optics gained a surge of interest with the construction of different magnetic reflectors for the reflection of paramagnetic atoms. Among the available magnetic mirrors, the data storage media possess potentialities for imaging applications. The first experimental realization was performed with audio-tapes [14]. The idea was then extended to floppy disks [15, 16] and videotapes [17]. Besides a high magnetic field

gradient, a smooth reflecting magnetic surface produces low imaging distortions. Perhaps the best advantage of the recording media lies in its aptitude to keep any shape due to its high flexibility. This enables the correction of third-order aberrations [18] by designing the adequate geometry for the magnetic reflectors [19].
In order to control atomic beams with magnetic reflectors, the development of atomic sources is of the greatest importance. The generation of slow atomic beams with narrow distribution of velocity from a thermal atomic beam is now realized routinely [20, 21, 22, 23, 24], however with very complex setup. A new generation of atomic beams simply based on cold atoms from a vapor-loaded magneto-optical trap (MOT) [25] produces very low velocities without drastically affecting the atomic flux. From this principle, different methods have been implemented to extract the atomic beam: by drilling a hole in one of the mirrors of the MOT [26, 27], with a pyramidal mirror structure with a hole at its vertex [28, 29], with a dark hollow laser beam where atoms from a MOT experience Sisyphus cooling [30], with a static magnetic field superimposed with an optical molasses along the beam axis [31], or even with a moving-molasses MOT "MM-MOT" [32].

In the frame of the work presented in this thesis, we propose to study with a Zeeman-slowed atomic beam the reflectivity of a videotape as a magnetic mirror. We show how it is possible to find an absolute value of the magnetic field strength at the surface of the reflector. By curving the mirror, multiple reflections at the surface of the videotape permit the deflection of atoms without being lost at very large angles.
Due to the low magnetic barrier at the surface of the videotape, we decided to build a source of cold atoms from a 2-dimensional MOT ($2D$-MOT) [33] with a laser beam as optical pusher for extracting the atoms from the optical trap. This enables the reflection of atoms at larger angles after one bounce compared with the previous Zeeman-slowed atomic beam. Thus, we show for the first time the imaging with a concave magnetic videotape of a collimated atomic beam at different angles of incidence.

In Chapter 1, we review briefly the magnetic mirrors constructed to date. Chapter 2 is devoted to the experiments realized with the Zeeman-slower apparatus. In Chapter 3, the experimental realization of the $2D$-MOT atomic beam is presented and finally Chapter 4 deals with the focusing of the atomic beam with the curved magnetic videotape.

Chapter 2

Reflective magnetic components

A mirror that reflects atoms or molecules has many potential applications. It is an essential element in atom optical experiments based on the De Broglie wave of atoms, such as interferometry or even for the construction of a Fabry-Pérot resonator. It allows also the manipulation of atomic beam and can be used to reflect and to focus a beam of atoms. This possibility will open new perspectives in imaging with atomic beams especially in neutral atomic lithography. Nanometer scaled patterns can be created by precisely depositing atoms on a substrate [34].
In this chapter, we will first briefly recall the magnetic force responsible for the deflection of atoms in an inhomogeneous magnetic field and then we will report on the mirrors which have been recently built. We will emphasize in particular the curved mirror which allows to focus atoms.

2.1 Stern-Gerlach force

Let's consider an atom with a magnetic dipole moment $\overrightarrow{\mu}$ moving in a magnetic field $\overrightarrow{B}$. The magnetic dipole interaction energy is given by

$$U = -\overrightarrow{\mu} \cdot \overrightarrow{B}. \tag{2.1}$$

where in general $\overrightarrow{B}$ and $\overrightarrow{\mu}$ is position-dependent.
For a slowly moving atom, the magnetic moment follows the field adiabatically and the angle between moment and field is constant. This adiabatic condition is given by [35]

$$|\overrightarrow{B} \times (\overrightarrow{v} \cdot \overrightarrow{\nabla})\overrightarrow{B}| \ll \omega_L \overrightarrow{B}^2, \tag{2.2}$$

where $\overrightarrow{v}$ is the velocity of the atom and w_L is the Larmor precession frequency. In this regime, no transitions i.e no spin-flip occur in the sublevels of the atom. The potential energy of the atom depends only on the field magnitude B and not on its direction. With this property, according to the quantum internal state atoms can be either reflected or attracted by the Stern-Gerlach force

$$\overrightarrow{F} = \nabla(\overrightarrow{\mu} \cdot \overrightarrow{B}) = -\mu_{eff} \cdot \overrightarrow{\nabla} B \tag{2.3}$$

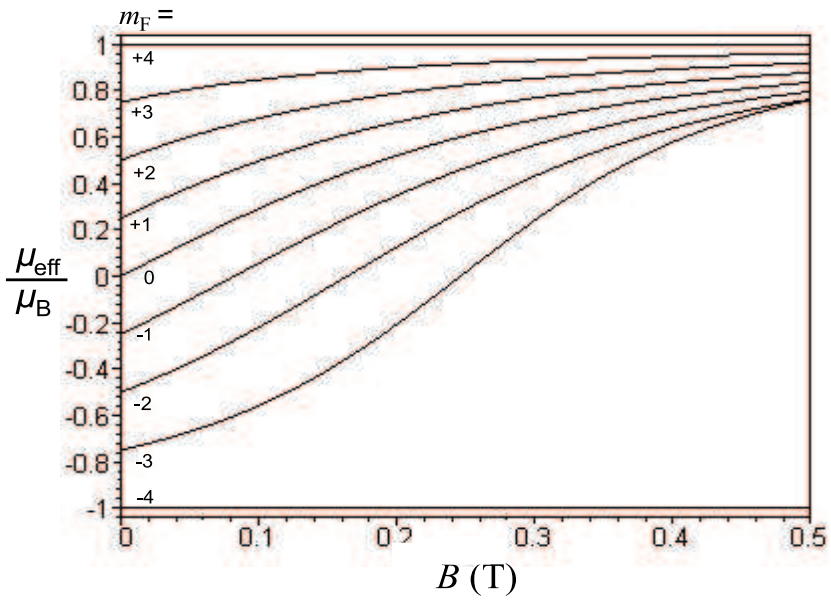

Figure 2.1: Effective magnetic moment for the $|\, F = +4 \,\rangle$ ground state of Cs according to Breit-Rabi formula.

arising for example from the field gradient of a magnetic surface. μ_{eff} is the resulting effective magnetic dipole moment of the atom in a magnetic field.
In general, an exact analytical solution of the energy levels and hence the magnetic moment of alkali atoms can be calculated and leads to the Breit-Rabi formula [36, 37]. Figure 2.1 shows the Breit-Rabi diagram for ^{133}Cs, the atomic element we used in our experiments. If the field is less than $\sim$ 300 G the hyperfine sublevels split due to the linear Zeeman shift. In this regime, the magnetic moment is independent of B and the interaction force is

$$\overrightarrow{F} = -m_F g_F \mu_B \overrightarrow{\nabla} B, \tag{2.4}$$

where m_F is the magnetic quantum number, g_F is the Landé factor of the hyperfine level F and μ_B is the Bohr magneton.
For $g_F > 0$, atoms in negative magnetic states m_F are attracted (high-field seeking states) while atoms in positive magnetic states m_F are repelled (weak-field seeking states) from regions of increasing field magnitude. This last property forms the basic principle of the magnetic mirror. For all ground state alkali atoms, the largest magnetic moment occurs for $|\, F, m_F = F \,\rangle$ where the repulsive force exerted on atoms is the largest and independent of the field magnitude B.

2.2 Magnetic reflectors

The analogy between light optics and atom optics for refractive components led to the extension of the concept to the reflective components. Perhaps, the notion of reflecting

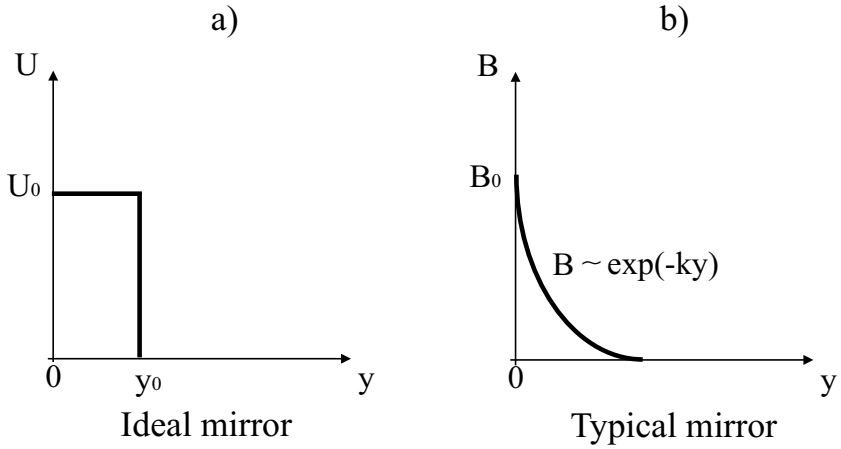

Figure 2.2: Magnetic potential for retro-reflecting atoms.

photons is most known in astronomical optics in which reflective elements have been intensively examined and developed for a long time [38]. Using the basic concepts and having in mind that atoms can be repelled in an inhomogeneous magnetic field, we attempt to find a configuration for the magnetic field equivalent to the hard wall function used to reflect photon as sketched in Figure 2.2 a). This is however the ideal component for atom optics which cannot be fabricated.
For realistic experiments, the idea for a practical realization of magnetic reflectors was first proposed by Vladimirskii in the sixties [39] in order to reflect cold neutrons. Opat extended this principle to electric and magnetic mirrors [40]. The best known configuration for a magnetic reflector close to the ideal hard wall corresponds to the exponential decay of the magnetic field as shown in Figure 2.2 b). However, the low energy barrier of the reflector limits the reflection to atoms with small kinetic energy. The turning point of the atom in the reflector corresponds to the position where atoms are repelled. For the maximum magnetic potential, we have

$$\frac{1}{2}mv^2 = \mu_{eff}B_0 \tag{2.5}$$

where v is the velocity of the atom, m is the mass of the atom and B_0 is the magnetic field at the surface of the mirror. For $B_0 = 500$ kG, we find $v = 6.5$ m/s for Cesium. We see how it is essential to develop magnetic reflectors with large surface fields in order to reflect thermal atomic beams. By considering the longitudinal v_ℓ and normal v_t components of the atomic velocity, the maximum angle of reflection is given by

$$\sin\ \alpha_{max} = \frac{v_{t_{max}}}{v_\ell} = \sqrt{\frac{2\mu_{eff}B_0}{mv_\ell^2}}. \tag{2.6}$$

where $v_{t_{max}}$ is the maximal allowed transverse velocity which can be reflected by the magnetic mirror. Strength of the surface field, steepness of the magnetic field and flatness of the mirror are the crucial parameters to control in the development and optimization

of magnetic reflectors. In the following, we present main the magnetic mirrors which have been realized in the laboratories.

2.2.1 Macroscopic permanent magnets

An infinite periodic array of magnets with an alternating uniform magnetization $M(x, y) = +M_0$ and $-M_0$ in the y direction with a periodicity a along x as shown in Figure 2.3 generates the magnetic field [41]

$$B(x, y) = B_0 e^{-ky}[1 + \frac{1}{3} e^{-2ky} \cos 2kx + ...], \tag{2.7}$$

where $k = 2\pi/a$ and $B_0 = 2\mu_0 M_0/\pi$. The first term in Equation (2.7) shows an exponentially decaying magnetic field which is independent of x. The second term depends on the coordinate x and leads to a corrugation of the mirror. This contribution decays more rapidly with y than the first term and can be neglected for sufficiently large distances $y \gg a/2\pi$. In this condition, only the first harmonic component $B_0 e^{-ky}$ remains important.
The expression (2.7) can be generalized to an ensemble of magnetization whose direction rotates with an angle $2\pi/S$, S giving the number of different magnetization directions for a period a. For a given mirror configuration S, we can write [42]

$$B^S(x, y) = B_0 e^{-ky}[1 + \frac{1}{S+1} e^{-2ky} \cos Skx + ...], \tag{2.8}$$

with $B_0 = \mu_0 M_0[\sin(\pi/S)/(\pi/S)]$.
The corrugated term in (2.8) decreases with S and at the same time the effective magnetic field B_0 increases at the surface of the mirror. The case $S = 2$ corresponds to Equation (2.7), whereas with $S \to \infty$, the second and higher order terms disappear and we obtain the ideal magnetic mirror with a continuous rotating magnetization,

$$B(y) = B_0 \ e^{-ky}. \tag{2.9}$$

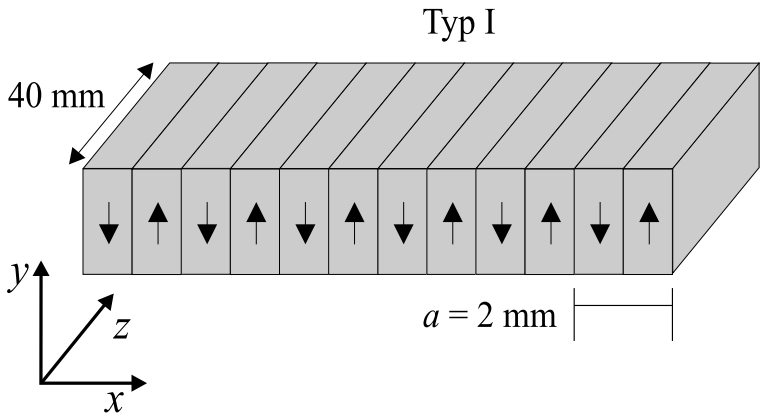

Figure 2.3: Assembly of alternated permanent magnets.

Two groups have constructed such mirrors configurations sketched in Figure 2.3 by assembling rare-earth permanent magnets. In Melbourne, researchers [41] realized a mirror of alternated magnetization ($S = 2$) from neodymium-iron-boron (Nd-Fe-B) with 18 slabs each 1 mm wide, 20 mm long and 12 mm deep. The magnetic field B_0 at the surface is about 4.2 kG and the period $a = 2$ mm. To compensate for end effects at the center of the mirror, two 0.5 mm-wide magnets with opposite magnetization where added at the ends of the array.
In our group [42] a mirror of samarium-cobalt (Sm-Co) has been constructed in a $S = 4$ configuration, i.e. with a rotating magnetization in 90° steps. The 90, 1 mm-wide, 90 mm-long and 5 mm-deep slabs generate a magnetic field of 1.1 T and the spatial period is 4 mm. By adding pieces of soft iron at each end sides, the influence of end effects on the whole mirror is compensated. With such a structure, the surface magnetic field has been increased to $B_0 = 1.18$ T while the magnetic field roughness in Equation (2.8) decreased.
In these macroscopic approaches, the magnitude of the surface field is large enough so that atoms with large angle of incidence can be reflected. However the main disadvantage arises from the long period of the mirrors which inevitably destroys the imaging quality of a reflected atomic beam.

2.2.2 Microscopic magnetic materials

The macroscopic approach shows that non-negligible contribution of fringe fields from the end sides arises at the center of the mirror. The difficulty to control roughness components, which scale over millimeter distances stimulated some groups to examine the benefits of micro-magnets mirrors.

Videotapes

A sine wave magnetization $M = M_0 \cos kx$ is considered along x, $k = 2\pi/a$ being the wave number and a the period of the magnetization. The magnetic field above the mirror can be easily calculated as [43]

$$B(y) = B_0(1 - e^{-kd})\ e^{-ky}, \tag{2.10}$$

where B_0 is the strength of the surface field and d is the thickness of the mirror. Generally the pattern recorded in the magnetic medium is not a perfect sine wave. Higher harmonics have to be taken into account and the field can be expressed as

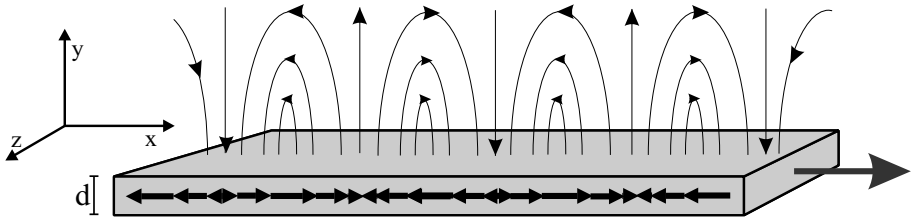

Figure 2.4: Sinusoidal magnetization along the x-axis in a videotape.

$$B(x,y) = B_1 e^{-ky}\{1+\frac{1}{2}\sum_{n>1}\frac{B_n^2}{B_1^2}e^{-2(n-1)ky}+\sum_{n,m\neq n}\frac{B_n B_m}{B_1^2}e^{-(n+m-2)ky}\cos((n-m)kx+\delta_n-\delta_m\}, \tag{2.11}$$

where B_n is the field amplitude of the nth harmonic at the surface of the mirror, δ_n is the phase of the magnetization. The first term in brackets is the fundamental corresponding to Equation (2.10). The second term is a slight correction to the exponential form of the field. The last term contains all corrugations between different harmonics. We see that the corrugations of longest range decay as e^{-ky} and corresponds to the beat between the fundamental and the second harmonic. All other terms decay faster and are less important
Recording a sinusoidal pattern in storing medium enables to use them as magnetic reflectors. The direction of the magnetization lies in the plane of the mirror. It was first demonstrated with audio-tape [14], then extended to floppy disks [15, 16] and videotapes [17]. Recent experiments have been realized with a magnetic reflector fabricated from commercial half-inch videotape (Ampex 398 Betacam SP). The measured magnetic field at the surface is as high as 0.1 T with a spatial period of 13 μm. End effects are very small due to the centimeter-sized mirror and to the micrometer wavelength.
Magnetic videotapes are prominent candidate in the family of potential reflectors because the roughness is very low. Dropping a cold cloud of atoms onto the surface turns out to be very efficient for the number of reflected atoms, however the small surface field strength turns out to be problematic for the reflection of an atomic beam limited often to grazing incidence. We will see in this work how we can overcome this difficulties.
To improve the performances of magnetic tapes as mirror for atom optics, new challenges can be achieved with perpendicular magnetic recording as an alternative to the longitudinal magnetization [44, 45].

Magneto-optical materials

Another alternative to the videotape are magneto-optical ferrimagnetic films, which possess a low Curie temperature. Magnetic structures can be written by focusing a laser beam in the presence of an external magnetic field. The large crystalline magnetic anisotropy presents an easy magnetization direction perpendicular to the plane of the film. The Equation (2.7) is generalized to this case, in which the period has microscopic dimensions. Thus, all higher harmonic terms have small contributions.
The group of Hannaford developed such mirrors with a film of TbFeCo [46]. The remanent magnetic field in the material reaches 0.24 T, but the film thickness produces only an effective magnetic field of 0.08 T at the surface of the mirror. The period of the structure is 2.1 μm. The observation of reflection of cold atoms was reported to be up to about 80 %.
Magneto-optical materials are very promising as magnetic reflectors because of the flexibility to write complex magnetic patterns like cylindrical mirrors.

2.2.3 Current-carrying wires

For an infinite array of wires carrying alternated electric currents of equal magnitude I in opposite directions, we obtain for the magnetic field an expression similar to Equation (2.7)

$$B(x, y) = B_0 e^{-ky}(1 + e^{-2ky} \cos 2kx + ...), \tag{2.12}$$

where $k = 2\pi/a$, a being twice the spacing between the wires, μ_0 is the magnetic permeability in vacuum and $B_0 = 2\mu_0 I/a$.
The corrugated term, which corresponds also to the second term in Equation (2.12), is three times larger than the coefficient in Equation (2.7). But this device offers a lot of possibilities like variation, switching or modulation of the magnetic field by altering the current flowing through the wires. Each element of the array carries exactly the same current and produces the same magnetic flux.
Using photolithography and electroplating techniques, two groups generated micro-electromagnet mirrors with micrometer-sized wires onto a substrate. The first group, that of Hannaford [47] deposited gold on a polished silicon substrate bonded to a molybdenum heat sink. The resulting mirror consists of 42 parallel wires, each 60 μm-wide, 8 mm-long and 10 μm-thick. The period of the array is $a = 330$ μm, the active area 7 mm $\times$ 8 mm. To generate the magnetic field, current pulses of duration $10 - 12$ ms are applied with a typical pulsed current of 3 A, which corresponds to a magnetic field $B_0 = 20$ mT. The field distribution of a finite number of wires approximates Equation (2.12) by adding two wires carrying half the current to each end of the mirror at half the normal spacing.
The second group at Harvard constructed magnetic mirrors with deposited gold wires on a sapphire substrate which are cryogenically cooled [48]. The specifications of the mirror used are cited in [49]. The serpentine consists of 101 lines with a period $a = 200$ μm and an active area 1×1 cm^2. An additional wire at the end of the mirror permits to enhance the number of wires to an odd number and hence to reach the condition of the ideal mirror in Equation (2.9). In order to preserve the quality of the mirror, only pulsed currents up to 3 A were used at liquid nitrogen temperatures, which corresponds to fields

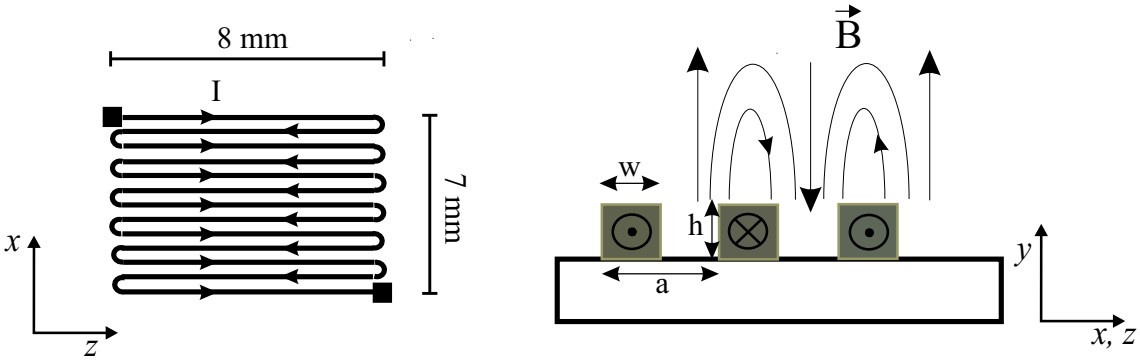

Figure 2.5: Flow of a current I through a snake-formed wire. A side view of the device shows the periodicity of the current, which generates the magnetic field.

up to ~ 0.3 T at the surface of the wires.
In this scheme the surface field is mainly limited by the maximum current supported by the wire. The small active area of the mirror enables to reflect samples of laser-cooled atoms and the reflection of an atomic beam at grazing incidence (1 mrad) has been also reported [50].

2.2.4 Natural crystals

Ferromagnetic materials present natural domain structures resulting from the minimization of the stray field to the free energy. This field is exploited in order to realize a magnetic mirror. Different techniques, like optical, magneto-optical as well as mechanical micro-scanning techniques, allow to observe the domains at the surface of samples. However, there is no way up to know to observe directly the interior domains [51].

Cobalt single crystal

The Co-single crystal has a diameter of 10 mm and a height of 1 mm. The crystal is polished on one side and the orientation of the surface with respect to the crystal axis is as good as 1°. The organization of the domain patterns reveals a high degree of regularity in the width of the domains. Similarly to macroscopic permanent magnets, alternating domain intensities in Figure 2.6 shows an alternating magnetization in one dimension.
The remanent magnetization in the bulk material is 1.2 T, but the surface field is about 0.7 T. The mean extension of the domains d (μm) in the Co-single crystal is related to the height h (μm) by $d = 0.3h^{0.66}$ [53]. The periodicity deduced from the domain width in

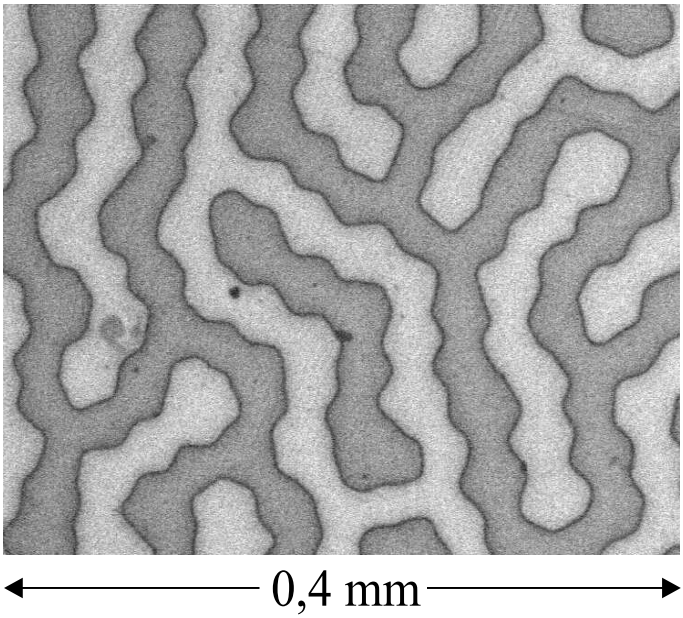

Figure 2.6: Domain pattern of a Co single crystal (from [52]).

Figure 2.6 is 31 μm. This value is in good agreement with that deduced from the previous formula.
By dropping cold atoms of rubidium onto the surface of the crystal, it has been possible to determine the surface roughness of the reflector corresponding to an angular variation of 3 mrad [52].

Sintered Nd-Fe-B

In the crystal the proportion of each element is $Nd_2Fe_{14}B$ which is strongly magnetic. Due to the high magneto-crystalline anisotropy, the domain are largely oriented and in this material they are magnetized by the processus of fabrication perpendicular to the surface. The spontaneous magnetization of a domain is 1.63 T [54]. The typical dimension of the domains at the surface is 1 μm.
A closer examination with a polarization microscope and a MFM (magnetic force microscope) shows that the domains are almost exclusively magnetized perpendicular to the surface and they present a mean width of 1 μm [42]. For measurements with the MFM-tip at large distances from the surface, the spatial resolution decreases. This is an indication that the stray field decreases very fast and its strength depends however on the orientation of the crystallite axis and the normal of the surface.
An atomic beam with a longitudinal velocity of 59 m/s has been reflected onto the surface of the crystal. The investigation showed that the measured magnetic field is 0.9 T while the given remanent magnetization is 1.2 T.

Grooved structures

Using electron-beam lithography techniques, small periodic grooves in a ferromagnetic material generate a magnetic field distribution above the surface which is equivalent to an array of alternating magnetization. The periodicity ranges from 0.7 μm to 10 μm.
The best results have been obtained with nickel which shows a strong surface field [55].

Ferromagnetic structures as mirrors for atom optics seem to be a powerful tool for

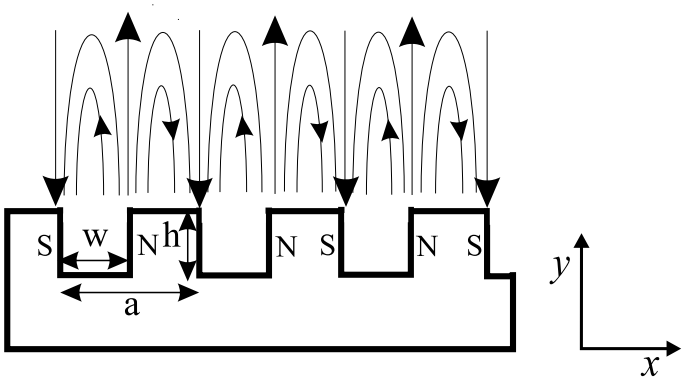

Figure 2.7: Microfabricated grooved structure.

the long term under the condition that it would be possible to have full control on the dynamics of the domain not only in thin films as it has still been shown [56] but also in bulk materials.
In Table 2.1 we have reported the relevant parameters of the main magnetic mirrors discussed above. The period a determine the gradient of the magnetic field while the surface field strength B_0 allows to reflect atoms with a large velocities. The roughness governs the flatness of the reflector and enables to reduce the diffusive component of the reflection. The reflectivity of the mirrors has been tested with a cold cloud of atoms (MOT) as well as with an atomic beam (AB).

Type of mirror	Period a (μm)	B_0 (T)	Roughness (mrad)	v_{tmax} (m/s)	Element	Type of experiment
Nd-Fe-B slabs	2000	0.42	low flatness	5.9	Cs	AB
Sm-Co slabs	4000	1.10		9.6	Cs	AB
Video tape	13	0.10	6	2.9	Rb,Cs	MOT, AB (this work)
TbFeCo	2.1	0.08		2.6	Cs	MOT
Au wire,Si substrate	330	0.02		1.3	Rb	MOT, AB
Sapphire substrate	200	0.03	13	1.6	Cs	MOT
Co-crystal	30	0.70	54	7.7	Cs,Rb	AB, MOT
Sintered Nd-Fe-B	1-10	0.90		8.7	Cs	AB

Table 2.1: Relevant parameters of the main magnetic mirrors.

Even if macroscopic mirrors can repel high atomic velocities, they suffer however of high imaging distortions. Microscopic magnetic-based materials show better atom optical quality. In particular, magnetic video tapes offer features like focusing that are not attainable with other magnetic reflectors.

2.3 Imaging above a spherical mirror

Contrary to flat magnetic mirrors discussed above, a spherical reflecting surface has image-forming properties similar to those of a magnetic refractive lens. In some way, the imaging from a spherical mirror is superior to that from a magnetic lens, notably in the absence of chromatic effects due to dispersion that always accompany the "refraction" of an atomic beam. Because of the simplicity of the law of reflection compared with the law of refraction, the quantitative study of the image formation by mirrors is easier than for lenses. Many features are the same, like focal point or focal length, which are emphasized in the next.
A description of the imaging of an atomic beam is calculated in detail in Appendix A.
To date only one experiment has been realized with a curved reflector. In the Hind's group, achromatic imaging has been achieved with a sample of cold Rb atoms. The principle is sketched in Figure 2.8 where an atomic cloud bounces freely on a concave magnetic atom mirror with a radius of curvature R. A curved videotape has been used as magnetic reflector. The initially compact cloud dropped from a height $R/4$ is alternately

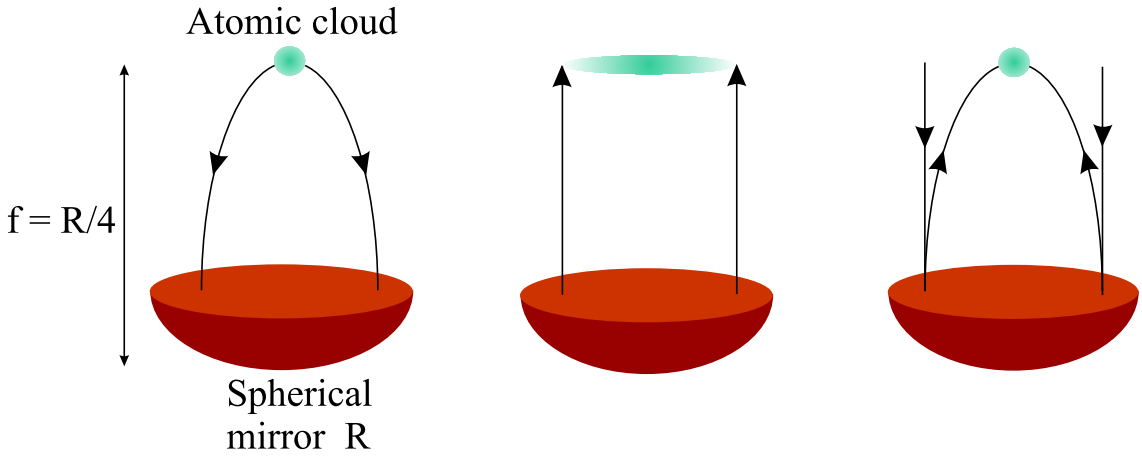

Figure 2.8: Achromatic imaging of a cloud of cold atoms.

collimated and brought back to a focus. The height $R/4$ is the focal plane of the mirror, a factor 2 different from classical optics because the atoms fall under gravity on parabolic trajectories [16]. In this experiment, the imaging of cold atoms has been realized by means of a reflector which is free of abberations. However this approach cannot be used in atomic lithography due to the low flux of atoms.
In our work, we will investigate the imaging properties of an atomic beam by using the same videotape as reflector and will show that potential applications towards neutral atomic lithography is possible.

Chapter 3

Whispering gallery mirror for atom beams

Among the reflectors presented in Chapter 2, we have chosen the magnetic videotape because of its simplicity. Also its flexibility enables to find easily any geometrical shape for applications in magnetic reflective atom optics.
In this Chapter, we study the reflection properties of a Zeeman slowed atomic beam and show that videotapes are potential candidates for imaging with atomic beams [57].

3.1 Zeeman-slowed atomic beam

Laser cooling methods provide the possibility to obtain very well collimated and slow atomic beams. Different approaches can be implemented for decelerating a thermal atomic beam largely described in [58]. With these intense sources, we investigated the deflection of a polarized Cesium atomic beam by a magnetic mirror.

3.1.1 Principle of operation

It is well known that a laser beam exerts a radiation force on free atoms and can be used for radiative deceleration of an atomic beam. One way is to direct a laser opposite to the motion of an atomic beam. However as the atoms in the beam slow down, their changing Doppler shift take them out of resonance. To overcome this problem, two different methods can be used. The first, by sweeping the laser beam frequency to keep it in resonance with the atomic-resonance [59]. The second, the method we have chosen consists in varying the atomic resonance frequency with an inhomogeneous magnetic field to keep the slowed atoms in resonance with the fixed frequency of the laser [60].
The Zeeman-slowed atomic beam shown in Figure 3.1 has been fully described and characterized in [42, 22]. A thermal atomic beam enters the region of strong magnetic field, where atoms are cooled along the beam axis. A σ^+-polarized laser beam counter-propagates the atomic beam and slows atoms by momentum transfer. During the decelerating process, the absorption probability in the moving coordinate frame of atoms decreases due to the

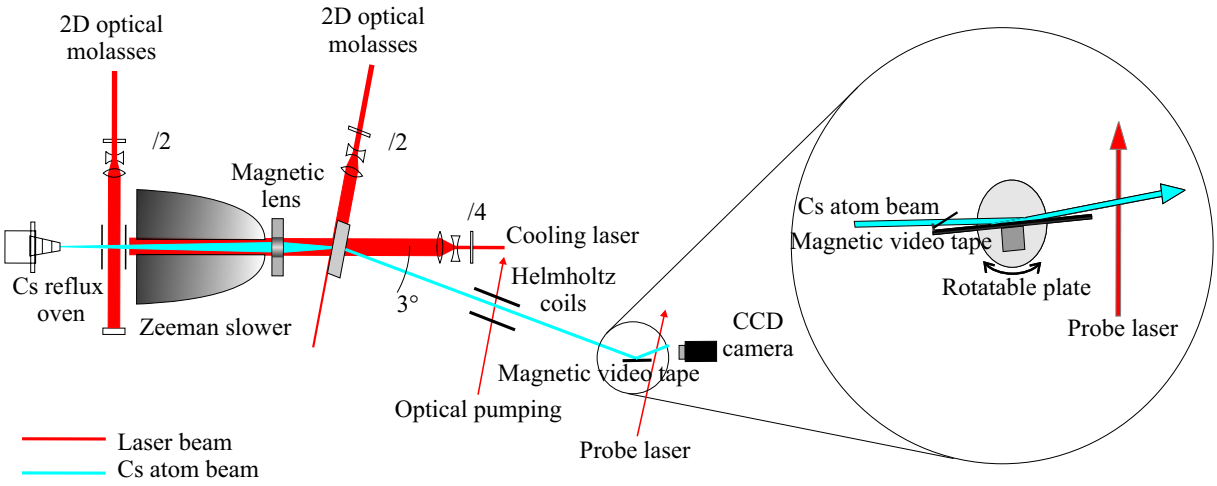

Figure 3.1: Zeeman slower set-up.

Doppler shift of photons to the red. But the tailored magnetic field compensates for the Doppler shift by imposing a Zeeman shift on the atomic energy levels and hence keeps atoms in resonance along the axis. For a uniform deceleration a the appropriate magnetic field profile is given by

$$B(z) = B_0\sqrt{1-\frac{z}{z_0}} \tag{3.1}$$

where z_0 is the slowing distance. This length is determined essentially by the initial velocity of atoms and $z_0 = v_0^2/2a$ where v_0 is the maximal longitudinal velocity that can be slowed.

3.1.2 Atomic beam apparatus

Atoms in the thermal atomic beam emerge from a reflux oven [61]. This thermal source is based in the possibility to recycle atoms which do not escape the hot region. Thus, the loading time of the thermal atomic beam is greatly enhanced compared with the traditional oven, cooled with liquid nitrogen. In all our experiments, we use ^{133}Cs atomic element. The melting point is given by 28.44° while the boiling point is 671° [62]. To optimize the flux of the thermal atomic beam, we heated the oven to up to 130°. The longitudinal velocity distribution of the atomic beam is deduced from the Maxwell-Boltzmann distribution [37] with the mean velocity $\overline{v} = 3/4\sqrt{\pi}v_p \approx 298$ m/s, where $v_p = \sqrt{2kT/m} = 224$ m/s is the most probable velocity, $T = 403$ K is the oven temperature and k the Boltzman constant. To slow down such thermal velocity to few hundreds of mK, a laser system is required. Most of the lasers used in our experiments are semiconductor laser diodes emitting powers of 100 mW or 50 mW with at the 852.3 nm wavelength. The collimated laser beams are linewidth-narrowed by optical feedback from an external grating mounted in the Littrow configuration. A small fraction of laser light is used for laser frequency stabilization by electronic feedback from Doppler-free saturated absorption spectroscopy and polarized

absorption spectroscopy in Cs cells [63, 64, 65].
Our reference laser provides a narrow linewidth ($\sim$ 10 kHz) by resonant feedback from an external confocal cavity. A thin glass in front of the laser chip enables to select a given longitudinal laser mode and hence to lock it at the given optical transition with a standard polarization spectroscopy [66]. The decelerating laser is stabilized to the reference laser through an heterodyne phase-locked loop [67], owing a blue detuning frequency up to 250 MHz. This allows us to choose the end velocity of the slowed atomic beam by tuning the frequency of the laser beam. Beside a small longitudinal velocity of the atomic beam, a small atomic angular spread is desired for experiments in reflective atom optics. The preparation of the slow atomic beam with small transverse velocity requires the implementation of transverse cooling processes at different stage of the experimental setup.

3.1.3 Preparation of the atomic beam

Before the atomic beam arrives in the experimental stage, different transverse manipulations have been realized. These have been reported in [42, 68], we will outline here the main results.

Transverse optical collimation

The transverse expansion of the thermal atomic beam leaving the oven proved to be unsuitable for a good longitudinal slowing process in the inhomogeneous magnetic field. To solve this problem, a molasses with elliptically shaped light fields (5×45) mm in a *lin* $\perp$ *lin* configuration ensures a sub-Doppler transverse cooling along the atomic beam axis [69, 70, 71]. Two apertures ($\varnothing = 3$ mm) are inserted between the oven and the slowing zone to reduce the divergence of the atomic beam as well as to stop the uncollimated fast atoms. The velocity capture range of the laser beam is larger than the maximal transverse velocity of the atomic beam so that all atoms are transversally cooled below the Doppler limit i.e down to 5 cm/s. This has also the advantage of increasing the atomic beam flux before the longitudinal deceleration.

Deflection and transverse collimation

At the end of the decelerating stage strong permanent magnets decouple atoms from the slowing process so that atoms leaving the slowing stage in the $\left| 6^2S_{1/2} \right\rangle$ scatter very few photons ground state which do not contribute to a longitudinal spread of the atomic beam. Additional heating from the randomly scattered photons results in the transverse spread of the atomic beam. In order to compensate this effect, a magnetic hexapol lens from permanent magnets [13] focus the atomic beam in the magnetic hyperfine sub-level $| F = +4, m_F = +4 \rangle$ inside a $2D$ optical molasses module formed by four mirrors onto an aluminum frame, which retro-reflects a single laser beam allowing a *lin* $\perp$ *lin* configuration for sub-Doppler cooling. The compression set-up is tilted by 3° with respect to the slowing axis in such a way to separate the slow atomic beam from the on-axis cooling laser beam and to eliminate the unslowed atoms from the atomic beam.

Optical pumping

During the optical collimation and deflection process, atoms interacting with the light field lead to a given distribution of the hyperfine states $|\,F=4,m_F\,\rangle$. The magnetic interaction with an external field, as seen in Chapter 2, produces a magnetic force whose magnitude depends on the m_F Zeeman-states. For Cs atoms, the maximum force is reached when the atoms are in the $|\,F=+4,m_F=+4\,\rangle$ state. This condition is required for most of our experiments with magnetic mirrors in order to reflect atoms at large angle of incidence. Two main schemes might be used to polarize the atomic beam.
The first uses a σ^+-polarized laser beam tuned to the $6^2S\,|\,F=4\,\rangle \rightarrow 6^2P\,|\,F'=5\,\rangle$ transition of Cs. A second laser in the $|\,F=3\,\rangle \rightarrow |\,F'=4\,\rangle$ transition pumps the atoms back to the $|\,F=4\,\rangle$ hyperfine level. After few absorption-emission cycles, most of atoms are in the $|\,F=+4,m_F=+4\,\rangle$ sub-level. However during this process atoms scatter light and are heated leading to a longitudinal and transversal spread of the atomic beam and a slight depolarization due to reabsorption of light scattered during the optical pumping process occurs [72]. To solve this problem, the atoms in the beam travel through a second laser beam whose intensity is very small but high enough to ensure a complete polarization of the atomic beam [42].
Another approach, which we use, for pumping atoms in the desired magnetic state consists to exploit the decoupling of atoms in a light field as shown in Figure 3.2. We consider a pair of σ^+-polarized laser beams resonant with the $|\,F=+4\,\rangle \rightarrow |\,F'=+4\,\rangle$ and the $|\,F=3\,\rangle \rightarrow |\,F'=4\,\rangle$ transitions. Atoms decaying from the excited states $|\,F'=+4,m_F=+3\,\rangle$ and $|\,F'=+4,m_F=+4\,\rangle$ into the $|\,F=+4,m_F=+4\,\rangle$ dark state stop to interact with the laser beams so that the atoms are not pumped anymore. This state is called a dark-state and the atomic beam is totaly polarized. Contrary to the previous discussed method the atomic beam do not suffer of reabsorption causing a

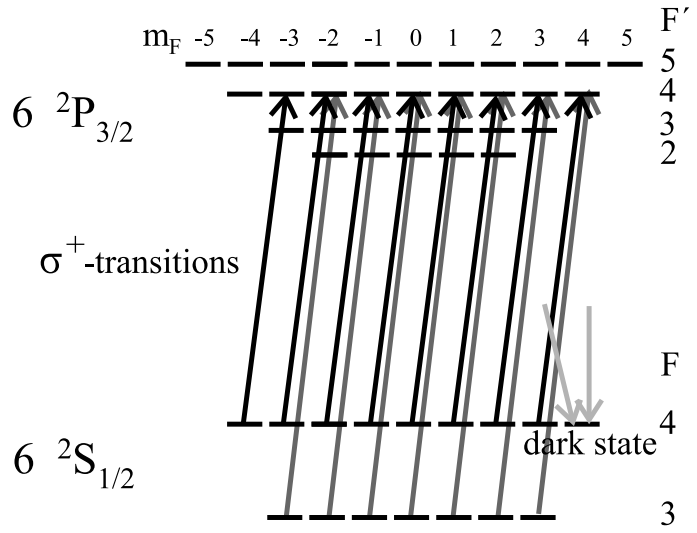

Figure 3.2: Optical pumping principle of the Cs atom in the dark state $|\,F=+4,m_F=+4\,\rangle$. The σ^+ laser beams provide a polarized atomic beam.

depolarization of the atomic beam. Once atoms are in the dark state, they stay there and leave the interaction region undisturbed.
To probe the efficiency of the atomic beam polarization, a small magnet of NdFeB is mounted on a translation stage perpendicular to the atomic beam. Without optical pumping the unpolarized atomic beam is divided into nine different atomic beams corresponding to the different m_F magnetic states. Turning on the polarizing beam more than 90 % of atoms are pumped in the $m_F = +4$ state.

The collimated and polarized atomic beam arrives in the experimental zone with typical tunable velocities ranging in the domain 40-100 m/s. However, the atomic beam flux decreases for slow velocities. The atomic beam cross-section is $\varnothing = 4$ mm for velocities ranging from 70 m/s to 85 m/s while the transverse velocity is $v_t = 0.05$ m/s.

3.2 Preparation of the reflector

Magnetic materials with large active area have the advantage to minimize boundary field effects at the center of the mirror. Commercially available videotape type AMPEX 398 Betacam SP offers this possibility. Beside a remanent field of 2.3 kG, the 12 mm-wide tape consists of a superposition of three layers: a Polyethylene foil, a 3.5 μm magnetic film containing small particles ($\sim$ 100 nm long, $\sim$ 10 nm diameter) and a graphite back coating [73].

3.2.1 Magnetic recording

Using a standard data storage tape drive, a custom-made recording head enables to write the a sine wave pattern in the videotape. The head has a gap of 12 μm and is 12.7 mm long, so that the entire width of the tape can be recorded. With a 2 kHz signal and a tape speed of 6 cm/s, a magnetization M

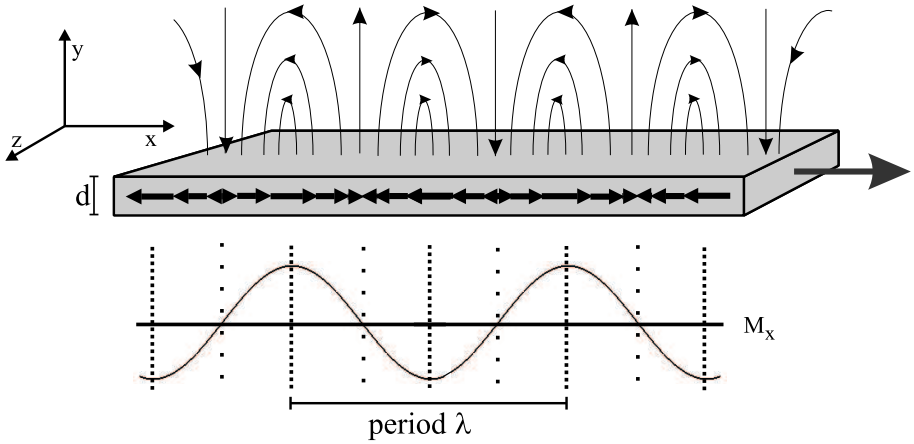

Figure 3.3: Periodically magnetized videotape, where the magnetization lies along the x direction.

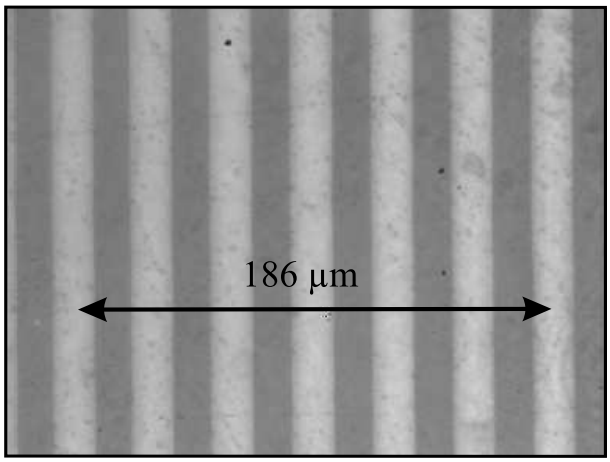

Figure 3.4: Photograph of the magnetized videotape taken through a thin film of garnet with a polarization-sensitive microscope. The periodicity of the magnetic videotape is clearly visible.

$$M = M_0 \cdot \sin kx, \tag{3.2}$$

is written where the spatial period is $\lambda = 2\pi/k$, as shown in Figure 3.3. During the recording process, a read head controls the writing stage. The period of the magnetization depends on the velocity of the motor pulling the tape: small periods are achieved with low tape velocity [74].

Period of magnetization

The period was checked by using a thin film of lutetium bismuth iron garnet (Bi:LuIG) [75] placed onto the surface of the tape. Depending on the magnetic field, the polarization of light passing through the crystal is rotated, due to the induced birefringence. With a polarization-sensitive microscope, the magnetic field at the surface of the tape is detected as a pattern of intensity fringes, shown in Figure 3.4. The alternating intensity is not sinusoidal because the magnetic field saturates the non-linear crystal. From Figure 3.4, we deduce a period of 31 μm.

Field surface

With Equation (2.10) mentioned in Section 2.2.2 of the last chapter, we can estimate the value of the surface field B_0. The maximal magnitude of M_0 is given by the remanent magnetization of 180 kA/m. Consequently, from the period of the magnetization and the thickness of the magnetic material, the largest B_0 for this tape is 58 mT. By choosing convenient parameters of the amplitude and frequency of the current in the recording head as well as the tape speed, the sinusoidal magnetization is maintained so that the maximum coincides with the magnetic saturation in the tape. Otherwise, over-saturation of the tape generates high harmonic components in the magnetic field and hence lead to

a rough mirror.
Standard probe techniques does not allow a measurement of the field at the surface because it varies on a microscopic length, whereas standard microscopic analysis methods deliver only relative field measurements. However, we will report in the next chapter how it is possible to determine a precise absolute value of B_0.

3.2.2 Mechanical construction

The tape used in all our experiments have been glued to a strip of commercial 35 mm photographic film with a slow-drying, low-viscosity epoxy (two components glue: Bylapox 7285 [76]). The film is fixed emulsion side down to a 3.4 mm thick sheet of float glass, placed on a flat aluminum baseplate. We applied a small quantity of glue onto the back side of the film, which proves to be extremely smooth. After waiting 10 min to eliminate the air bubbles and taking care not to trap them, the tape is laid on the glue. A "sandwich" is build-up by adding further layers of photographic film, glass and aluminium, and then clamped under very high pressure for 24 hours while the glue dries. All the operation has been realized in a clean laminar flow box in order to avoid dust.
The resulting film-tape system is strongly bound, presents a very smooth surface and even allows enough flexibility to be curved. The reflector is supported by different substrate. We glued the film-tape on a simple glass plate or on a flexible phosphor bronze sheet in order to make a cylindric mirror of variable curvature. The ends of the reflector are bent and glued around the end of the substrate, rather than being cut. It turns out to be essential for experiments, because the atoms arriving at grazing incidence on the mirror see a smooth magnetic field and not an ill-defined fringe field region.

3.2.3 Optical examination

The mechanical roughness was checked first with an atomic force microscope. We choose by eyes the worst region to be explored. The surface of the tape is scanned by a tip over an area of 1 μm^2 providing a rms height variation of only 7 nm. The exploration of the surface roughness was extended over a larger scale in order to confirm the flatness of the reflector. Using the method of coherence radar [77], the group of Häusler in Erlangen was able to map the roughness of a flat as well as a curved section of tape. The measurements showed that the resolution of the setup is limitated to 1 μm. This means that the detection of height variations below than 1 μm is not possible. We deduce that the tape has a surface quality in the submicrometer domain.

3.3 Atomic beam magnetometer for surface fields

In order to determine the magnetic field strength at the surface of the videotape we reflect the atomic beam from our magnetic mirror. From Equation (2.6) the maximum angle of reflection $\sin\alpha_{max}$ is inversely proportional to the longitudinal velocity v_ℓ of the atomic beam. With v_ℓ ranging from 40 to 100 m/s, the angles α_{max} are at grazing incidences.
For Cs atoms, which undergo a repulsion from the magnetic barrier, the maximum kinetic

energy is compensated by the maximum potential energy at the turning point which is very close to the surface and hence we can deduce the surface field B_0 from

$$B_0 = \frac{1}{2}\frac{m}{\mu_B}v_t^2. \tag{3.3}$$

We see that the determination of the atomic beam velocity will allow us to find the effective magnetic field B_0 at the surface of the mirror.

3.3.1 Experimental realization

For this experiment, we prepared a 11 cm-long mirror by the same procedure described in Section 3.2. The magnetic reflector was fixed on a table, which was rotated with a motor. The whole set-up was mounted in turn on a translating feedthrough, which provides the necessary mechanical adjustment for bringing the atomic beam onto the video tape. We investigated the reflection of the polarized atomic beam with Cs atoms in the $|\, F = +4, m_F = +4 \,\rangle$ state with the arrangement shown in Figure 3.5.

Atom beam velocity

The velocity of the atoms is adjustable and is measured by Doppler effect with a laser beam propagating at 155° with respect to the atomic beam axis. This laser induces a resonance fluorescence on the transition $|\, 6^2S_{1/2}, F = 4 \,\rangle \rightarrow |\, 6^2P_{3/2}, F = 5 \,\rangle$ of atoms. By detuning the frequency over the transition, the maximum intensity fluorescence gives the central velocity in the velocity distribution. With this method, the determination of the longitudinal velocity spread Δv_ℓ is limited to a resolution of $\Delta v_\ell \sim 4.5$ m/s for Cs [22] due to the natural linewidth of the excited state. A better resolution can be achieved with the time of flight technique (TOF). In our case we found a central velocity of 75 m/s with a full width at half maximum about 10 m/s. However, from former TOF measurements we know that $\Delta v_\ell = 0.7$ m/s.

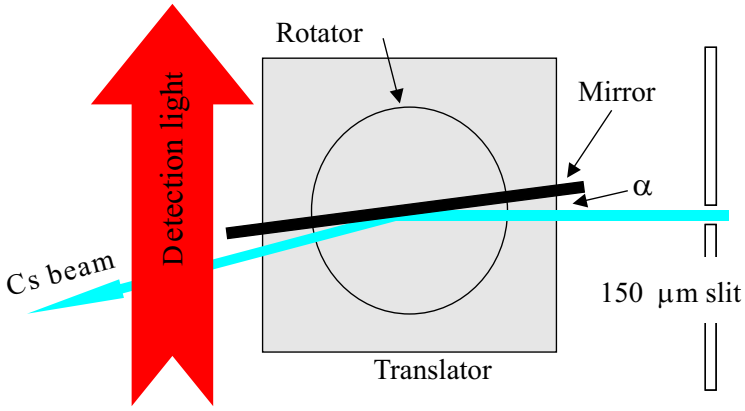

Figure 3.5: Experimental set-up for investigating reflection of atoms.

Effective surface of the mirror

The physical width of the atomic beam is limited by a first slit S_1 150 μm wide situated 20 cm upstream from the center of the mirror, and with a second slit S_2 of 700 μm located 95 cm away from the mirror, the geometrical angular spread is constrained to 0.6 mrad. The maximum transverse velocity allowed in the atomic beam after S_1 is a sub-Doppler velocity of 4.5 cm/s. The minimum mirror angle α required to reflect the whole atomic beam is $\alpha = 3$ mrad.

Reflection angle calibration

A helium-neon (He-Ne) laser adjusted to the both slits defines the incident atomic beam axis. The atom reflector mounted on a motor-controlled stage described in the previous chapter, is translated laterally towards the parallel red laser light and crosses it. The mirror angle α is changed until the He-Ne laser beam extends over the mirror surface and a fraction of light is still observable through the slit S_2. Therefore a red line on the dark mirror surface can be distinguished. There, the orientation of the mirror corresponds to our reference angle $\alpha_0 = 0$ where no reflections of atoms occur.
The quality of this adjustment can be controlled by cutting laterally the atomic beam with the mirror, which lower the beam fluorescence intensity up to half its maximal value. Moving the rotator to few degrees in the opposite direction symmetrically to α_0 decreases the fluorescence intensity to a same level.

The reflected atoms are detected by passing through a resonant vertical light sheet with a power of 2 mW, where they fluoresce. By mean of a cylinder lens, the laser beam is focused in the vertical plane to few millimeter in the vertical plane. A charge-coupled device CCD camera collects the scattered light from the atomic beam. The intensity of the fluorescence gives the relative intensity of the reflected atoms.

3.3.2 Results

Surface strength field of the videotape

Figure 3.6 shows the relative number of atoms that are reflected onto the magnetic mirror as a function of the incidence angle α. The data point marked by a circle at $\alpha_0 = 0$ corresponds to the fluorescence from the direct beam with the reflector moved at one side. This reference intensity is called unity. All the atoms are reflected for angles below 20 mrad however about 10 mrad the number of reflected atoms decreases which is probably due to a drift of the laser frequency. The signal drops as the angle is increased further, reaching low level by 30 mrad. The small residual signal at higher angles is due to a weak low-velocity tail in the velocity distribution of the atomic beam which is not affected by the Zeeman-slowing process added to a low stability of the lasers. The reflectivity decreases because atoms with high transverse velocity penetrating the repulsive magnetic barrier stick onto the surface. These atoms are lost from the beam. The grazing angle α has the value 28 ± 1 mrad at 50 % reflectivity, the error is based on the spread of the data points.

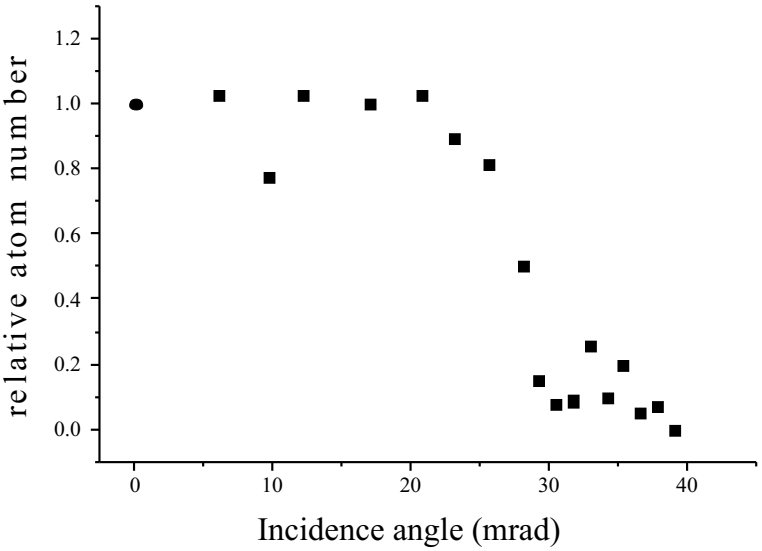

Figure 3.6: Relative flux of atoms that have been reflected from the tape as function of the angle of incidence at longitudinal velocity of 75 m/s. The reflectivity starts to decrease for angles larger than $\sim 20°$. This provides information on the magnetic field at the surface.

Thus, the normal velocity is $v_t = v_\ell \sin\alpha = 2.1 \pm 0.1$ m/s. From Equation (3.3) we deduce the surface field of our reflector being $B_0 = 53 \pm 5$ mT. The value is slightly less than the expected value 58 mT of the saturated magnetization.
The major contribution to the width of the step originates from the velocity distribution of atoms in the beam. The effect of the angular spread is negligible and no evidence of excess width have been observed due to the roughness of the mirror.
The flat grazing incidence mirror works as expected: all atoms are reflected and the measured surface field B_0 is in good agreement with the calculated value.

3.4 Whispering gallery

The previous experiment shows that we are faced with a typical problem known in x-ray optics, where reflections occur at grazing incidence. Multiple grazing incidences in a whispering-gallery geometry enable to deviate the atomic beam at large angles.

3.4.1 Multiple bounces

Resulting potential

The circular path followed by an atom on an arc of radius R, shown in Figure 3.7 generates a centrifugal force

$$F = m\frac{v_\ell^2}{R}, \tag{3.4}$$

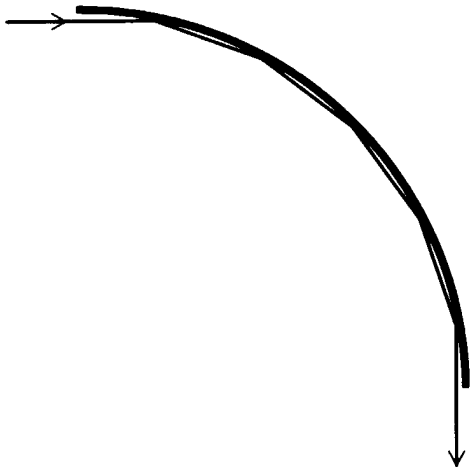

Figure 3.7: The whispering-gallery geometry.

which give rise to a pseudopotential at a small distance y from the surface of the mirror. Together with the magnetic potential from the tape, the total potential $U(r)$ is

$$U(r) = \mu_B B_0 e^{-kr} + m\frac{v_\ell^2}{R} r. \tag{3.5}$$

The pseudopotential is plotted in Figure 3.8 in radial coordinates. For this calculation we have taken $B_0 = 53$ mT as measured in the last section, the velocity v_ℓ is 60 m/s also used for this experiment, the radius of curvature $R = 9.6$ cm is limited by our mechanical

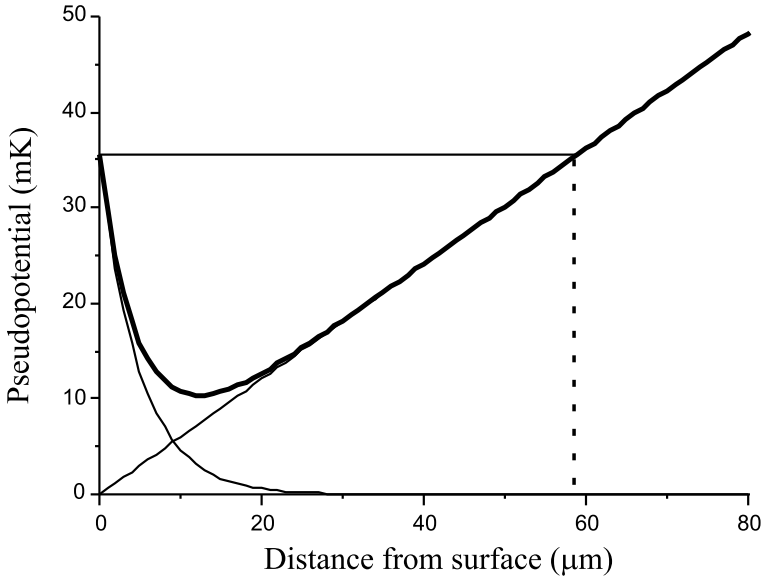

Figure 3.8: Pseudopotential for radial motion of the atoms.

construction.
In principle, the minimum radius of curvature R_{min} still allowing a transmission of atoms in the whispering-gallery is given, when the centrifugal force mv^2/R_{min} is equal to the maximum magnetic force $k\mu B$,

$$R_{min} = \frac{mv^2}{k\mu B}. \tag{3.6}$$

We find $R_{min} = 8.2$ mm with $v = 60$ m/s, $B = 0.05$ T, $k = 2\pi/a$, $a = 31$ μm and $\mu_B/m = 42$.
Atoms with velocity $v_t = 0$ experience radial oscillations in the potential shown in Figure 3.8. Atoms incident with impact parameters higher than 59 μm collide onto the surface and are lost from the atomic beam, due to their relative higher centrifugal energy than the magnetic energy at the surface (36 mK) needed to reflect them. Thus the channel-width of the whispering gallery is narrower than the 330 μm width of the atomic beam. However the angular acceptance of ± 35 mrad (at the center of the channel) allows radial velocity of 2.1 m/s, which is much larger than the angular spread 0.6 mrad of the atomic beam.

Counting reflections

For atoms arriving with angles close to zero, the entire width is filled and the ensemble presents a broad range of radial oscillation frequencies because the potential is highly anharmonic. Figure 3.9 points out the broad distribution in the number of reflections. Thus, the output beam has a wide angular dispersion. But if atoms enter the channel at a non-zero angle in such a way that their initial velocity is slightly less than the maximum allowed velocity for a reflection (2.1 m/s), only those coupled near the minimum y_{min} of the potential in Figure 3.8 survive their first oscillation. The oscillation frequency is well

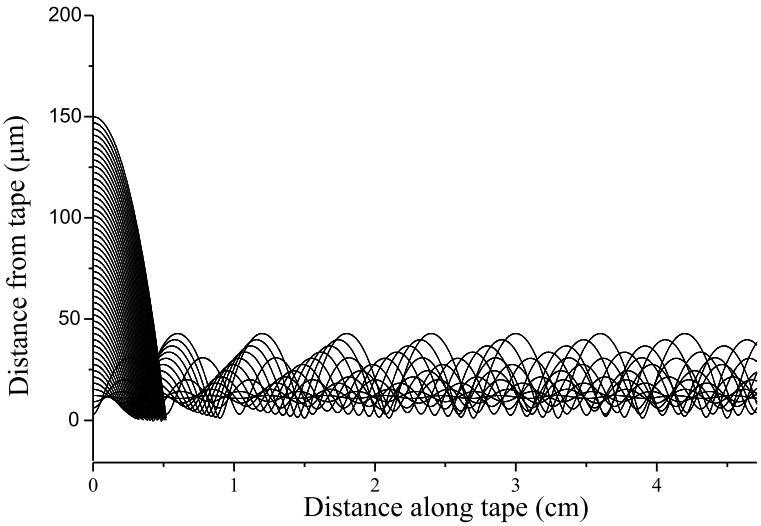

Figure 3.9: Strong dispersion in oscillation frequencies, which leads to a spatial spread of the output beam.

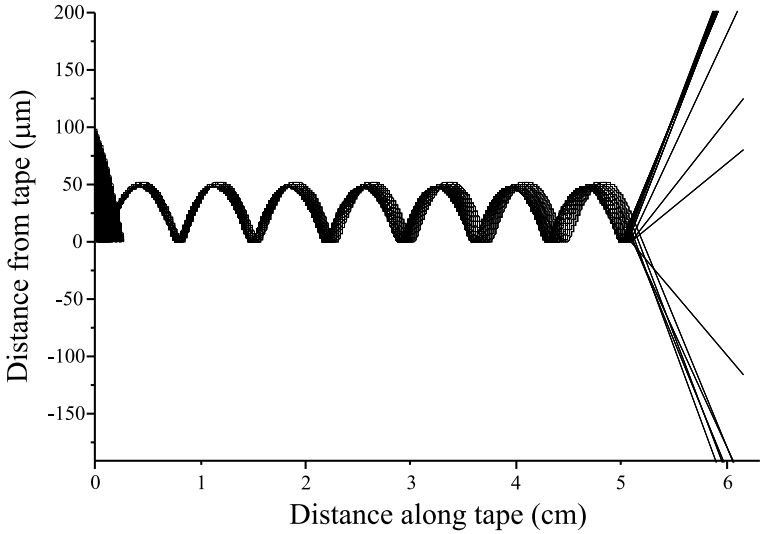

Figure 3.10: Trajectories of the atoms along the reflector calculated for 7 and 8 bounces.

defined for this small part of phase space. A calculation of trajectories is shown in Figure 3.10, where the incidence angle of atoms is $\alpha = 28$ mrad, i.e. with an initial velocity of 1.7 m/s. We remark in the simulation that the dispersion in oscillation frequency is quite small and a group of atoms bounces 7 times while the other group bounces 8 times. In the calculation, the radius of curvature is $R = 9.0$ cm so that some of the atoms are still reflected at the extremity of the tape, whereas others are missing the eighth bounce.
The inner part of the pseudopotential is approximated as a hard wall by only taking into account the centrifugal acceleration v^2/R. All atoms have almost the same maximum amplitude y_{max}. The bounce time t follows as

$$y_{max} = \frac{1}{2}\frac{v^2}{R}t^2, \tag{3.7}$$

therefore the oscillation period is

$$T = \sqrt{\frac{8y_{max}R}{v^2}}. \tag{3.8}$$

The travel time along the whispering-gallery is L/v, where L is the 5.3 cm-length of the tape. With Equation (3.8), the number of reflections N is

$$N = \frac{L}{v}\sqrt{\frac{v^2}{8y_{max}R}} = \frac{L}{\sqrt{8y_{max}R}}, \tag{3.9}$$

which has the value 7.9 when the radius is 9 cm.

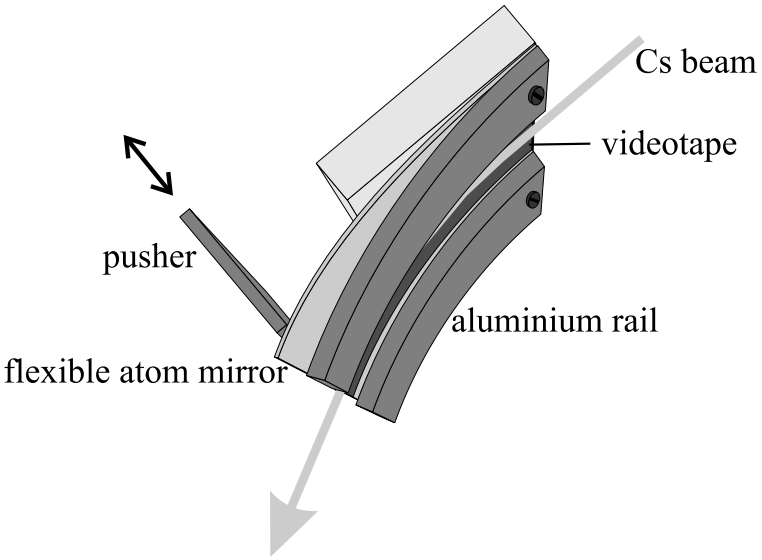

Figure 3.11: The sinusoidally recorded tape is glued to a metal strip that can be bent into a curve by pushing on the end as shown. The slow atomic beam can be deflected by multiple bounces through angles as large as 23°.

3.4.2 Experimental realization

The experiment conditions are the same as mentioned in Section 3.3, but the velocity is now adjusted to 60 m/s. Starting with the simple plane mirror configuration, the flexible phosphor bronze strip is pressed at one extremity and enables smooth variable curvature radius R. The reflector assembly is shown in Figure 3.11, where the flexible atom mirror is clamped between a flat aluminum block and a pair of curved aluminum rails. The curvature of the videotape can be slowly changed by pressing on the back of the flexible sheet as indicated in the figure. The maximum angle reached is 22° because it is limited by the 9.6 cm curvature of the outer rails radius.
The atoms surviving the multiple reflections arrive in the probe laser which is tuned off-resonance up to -28 MHz in order to enhance the fluorescence of the path followed by the atoms and hence recorded by a CCD camera.

3.4.3 Results

Multiple bounces

By translating the reflector set-up inside the atomic beam and by rotating the mirror i.e. changing the incident initial angle α, the distribution of the output beam presents different behavior. A broad atomic beam is observed for angles close to zero. This corresponds to the many different oscillation frequencies of atoms in the pseudopotential plotted in Figure 3.9. For larger input angle α, we rotate the whispering gallery around the vertical axis through the input end until the flux of deflected atoms in the beam drops to ~ 3 % of the undeflected beam. As the curvature is varied, the output beam leaves the magnetic

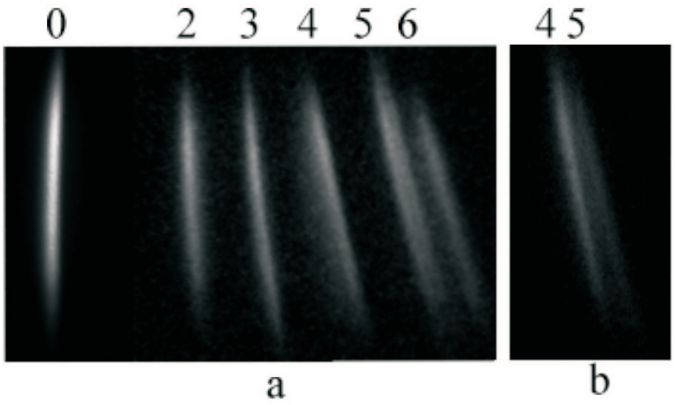

Figure 3.12: (a) Superimposed images of the deflected atomic beam for two, three, four, five and six reflections from the curved tape. The track labeled 0 is made by undeflected atoms.(b) A single image showing the double beam produced when some atoms have four reflections while others have five.

reflector at high angles, which reveals an increase in the number of reflections in the whispering gallery up to a maximum of eight producing a total deviation of 23°. Figure 3.12 a) is a sequence of six CCD images, corresponding to output beams after two, three, four, five and six reflections as well as the straight-through beam labeled 0.

The whispering gallery proves to be more suitable for large angular deviations than the planar mirror. In addition, the intensity of the deflected beam does not depend on the radius of curvature R, confirming that the reflectivity is unity after each bounce on the

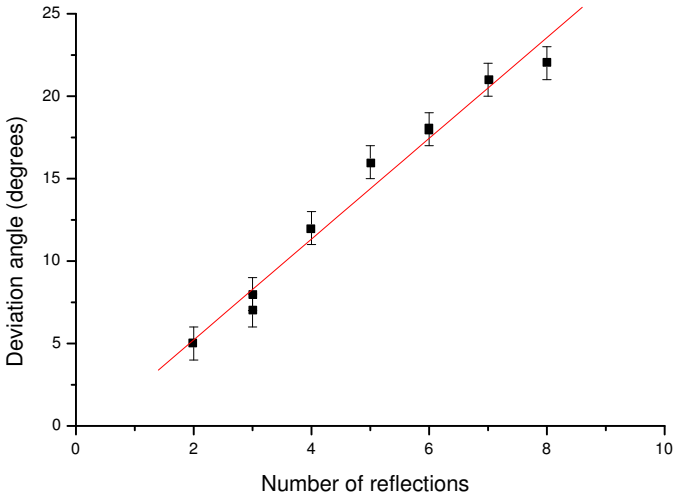

Figure 3.13: Plot of number of bounces vs deflection angle.

surface of the reflector. At some given curvatures, a structure in double output beams is found where some of the atoms undergo a certain number of reflections while others bounce one time less, as calculated in Figure 3.10. The picture in Figure 3.12 b) represents the case for four and five bounces.
Assuming the cylindrical mirror as a hard wall, each new reflection in the whispering gallery increase each time the angle of deviation to 2α. With the CCD camera, we can record the tracks produced by the deflection and measure directly the angles. These are taken just before the double beam appears. Figure 3.13 shows the deviation angles as a function of the number of reflections. The data points are approximated with a least-square linear fit. We deduce 2α from the slope and hence the value $\alpha = 25.3$ mrad corresponding to a single bounce in the whispering gallery. This is very close to the expected value of 28 mrad for complete extinction.

Bias magnetic field

As the atoms fly along the surface of the mirror they experience the spatially periodic magnetic field as a temporal oscillation at $\nu = v_\ell/\lambda = 2.5$ MHz. This has the possibility of driving transitions between the magnetic sublevels, resulting in a much reduced reflectivity for the mirror. In order to avoid this effect, a homogeneous magnetic field $\overrightarrow{B}_z$ of 10 G from a Helmholtz configuration is applied along the z direction as indicated in Figure 3.14. All our experiments as well as the data in Figure 3.15 are realized with this bias field. Without any bias, the intensity of the reflected beam is much smaller. The minimum intensity of the bias field needed to maintain a splitting between sublevels that is larger than the 2.5 MHz oscillation frequency, is given by

$$B_z = \frac{h\nu}{\mu_B g_F}, \tag{3.10}$$

where $h/\mu_B = 1.4$ MHz/Gauss. Thus, the field needs to exceed 7 G and this is the reason why we used 10 G.
In Figure 3.15, we reported the reflectivity of the atomic beam depending on the intensity of the bias field. The measurement corresponds to a deflection of the atomic beam at 17.3°. The intensity of the reflection has been normalized with respect to the incident atomic

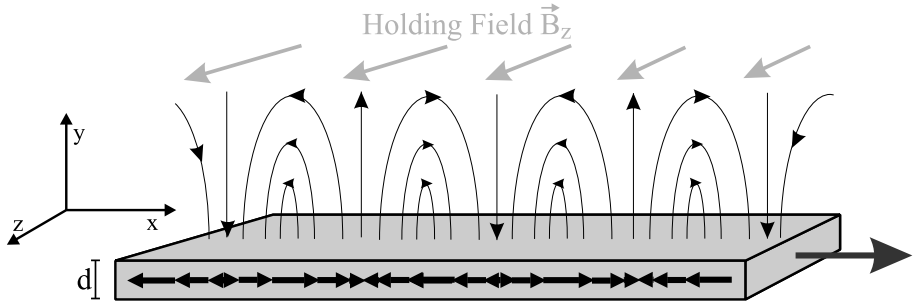

Figure 3.14: Additionally to the field from the mirror, a bias field B_z is applied in the z direction to avoid spin-flip of atoms in magnetic sublevels $m_F \neq +4$.

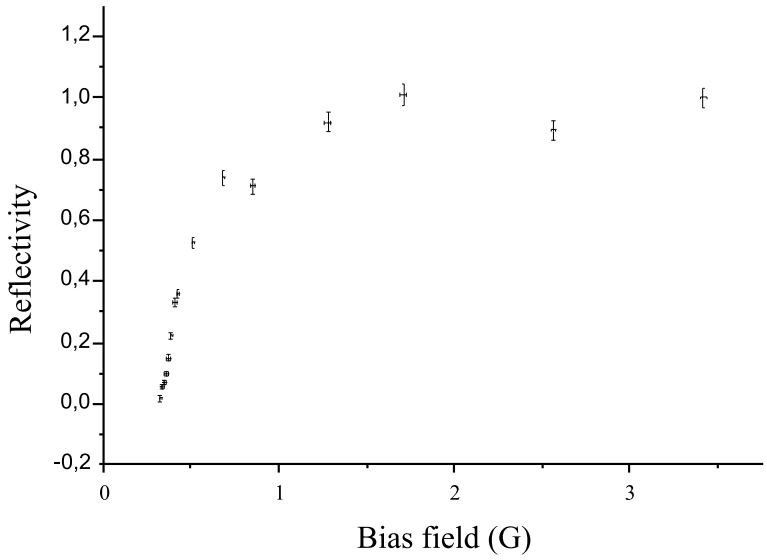

Figure 3.15: Relative reflectivity of the atomic beam as a function of the bias field. The reflectivity is still 1 for values as low as 2 G.

beam. The data point show that a smaller bias field of only 2 G still works compared with the 10 G applied magnetic field i.e all atoms incident on the magnetic mirror are reflected. The reason of this discrepancy from the theoretical expected value is not known yet and a deeper investigation of this effect will be carried out in the future [78].

Chapter 4

A cold atomic beam from a $2D$-MOT

In the last chapter, we demonstrated the possibility to deflect an atomic beam at large angles by multiple reflections. However angles of incidence were restricted to the grazing incidence regime, well-known in x-rays optics. In this condition, we were not able to observe the image formation of the Zeeman-slowed atomic beam at grazing incidence after the reflection onto the single reflector.
To overcome this difficulty, atomic beams with large angles of incidence are required. This implies either the development of new magnetic materials presenting higher magnetic energy at the surface of the mirror or to reduce the longitudinal velocity of atoms in the atomic beam. The second option has been chosen because videotapes have the advantage to keep easily any geometrical shape allowing us to design, if possible an abberation-free system. In the following chapter, a $2D$-MOT is built as a source of our slow atomic beam which is first optically collimated and then optically pumped, for further experiments with magnetic videotapes.

4.1 Principles of operation

4.1.1 $3D$ Magneto-optical trapping

We consider first a gas of atoms irradiated in one dimension by two counterpropagating laser beams with a wave number $\overrightarrow{k}$. The laser frequency ω_L is tuned just below the atomic resonance ω_0 ($\Delta = \omega_L - \omega_0 < 0$ red detuning), which causes an atom moving with a velocity $\overrightarrow{v}$ to absorb more light from the counterpropagating wave than from the copropagating wave due to the Doppler shift. The laser exerts a radiation pressure on the atom and leads to a damping of the atomic velocity [79].
This basic idea has been extended to a large range of new applications to influence the atomic velocities and the phase space density.

In optical molasses, atoms are cooled but not confined because the damping force

is not spatially-dependent. The Doppler cooling principle is extended by adding an inhomogeneous magnetic field in order to trap atoms [25].
Let's consider an atom with a transition ($J = 0 \rightarrow J' = 1$) in a one dimensional $\sigma^+ - \sigma^-$ polarized standing wave. An inhomogeneous magnetic field splits the Zeeman energy levels by the amount $\Delta E = g_J m_J \mu_B B(z)$, where $m_J = -1, 0, +1$. Atoms moving in the **z** direction scatter more light from the σ^- laser beam than from the σ^+, because the laser frequency is closer to the $\Delta m = -1$ transition, as depicted in Figure 4.1 a). The atom undergo hence a force $F_\pm$ towards the origin ($B(z) = 0$) as

$$F_\pm = \pm\hbar k \frac{\Gamma}{2} \frac{s_0}{1 + s_0 + [2(\Delta \mp kv \pm g_J \mu_B B(z)/\hbar)/\Gamma]^2}, \tag{4.1}$$

where the saturation parameter $s_0 = I/I_0$ is the ratio of the light intensity I to the saturation intensity I_0 ($I_0 = 1.1$ mW/cm^2 for Cs) and Γ is the linewidth of the transition, for Cs $\Gamma = 2\pi \cdot 5.18$ MHz. For small a velocity $kv \ll \Gamma$ and a weak magnetic field $g_J \mu_B B(z)/\hbar \ll \Gamma$, the net force

$$\overrightarrow{F} = -\alpha \overrightarrow{v} - \beta \overrightarrow{z}, \tag{4.2}$$

where α and β are respectively the friction and the spring coefficient

$$\alpha = -4\hbar k^2 \frac{I}{I_0} \frac{(2\Delta/\Gamma)}{[1 + (2\Delta/\Gamma)^2]^2}. \tag{4.3}$$

and

$$\beta = -4\hbar k \frac{I}{I_0} \frac{(2\Delta/\Gamma)}{[1 + (2\Delta/\Gamma)^2]^2} g_J \frac{\mu_B}{\hbar} \frac{\partial B}{\partial z}. \tag{4.4}$$

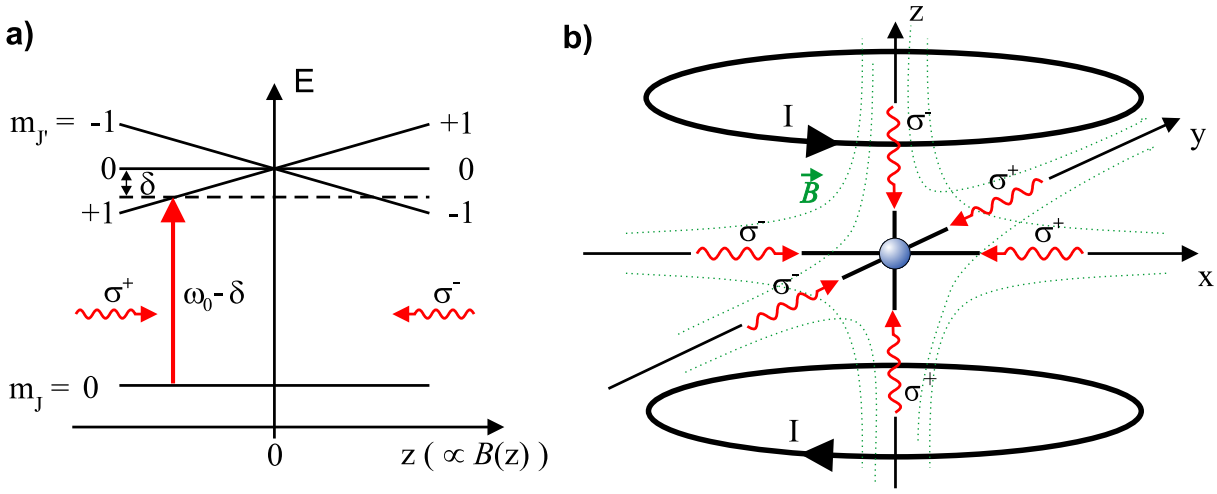

Figure 4.1: Principle of a Magneto-optical trap (MOT). a) The one-dimensional picture. Due to the Zeeman shifts of the atomic transitions in the inhomogeneous magnetic field, atoms at $z < 0$ are closer to resonance with the σ^+ laser beam than with the σ^- laser beam and are pushed toward the center of the trap. b) Extension to the three dimensional case. A quadrupole magnetic field is generated by coils in anti-Helmholtz configuration.

The damping force combined with the restoring force permits to cool and trap atoms in the minimum $B = 0$ of a 3-dimensional magnetic field, schematically shown in Figure 4.1 b). For further details see e.g. [80, 81, 82].

4.1.2 Atomic beam generation from a $2D$-MOT

Using the basic concept described above, one way to extract atoms from a magneto-optical trap is to use a $2D$-MOT configuration. The principle is sketched in Figure 4.2.
The atoms are loaded into the trap from a background gas [83]. Two pair of counterpropagating σ-polarized laser beams cross each other in the minimum field created by wires carrying alternated electric currents. The magneto-optical force exerts a restoring force on atoms toward the symmetry axis defined by the zero magnetic field. Atoms from the vapor entering the cooling region are transversely confined under the condition that the collisional process with the background gas in low enough and that the radial velocities (perpendicular to the z-axis of the zero magnetic field) are smaller than the maximum transverse capture velocity given by $v_{cap} \approx \Gamma\sqrt{1+s_0}/k = 4.5\sqrt{1+s_0}$ m/s.
The transverse capture of atoms in the $2D$-MOT leaves the atoms free to move along the z-axis (see Figure 4.2) and generates a continuous flux of slow atoms in the two antiparallel directions along the zero magnetic field. This produces a thin and dense atomic beam propagating along the z-axis. The generated atomic beam is delimited by a geometrical hole located in the $+z$ direction which enables to extract only slow atoms from

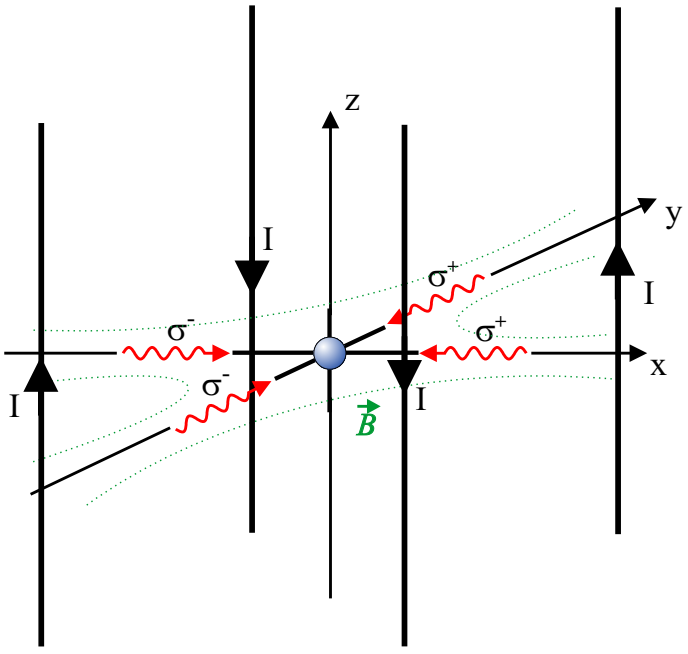

Figure 4.2: Scheme of the two dimensional MOT ($2D$-MOT). Alternating currents produce a two dimensional magnetic field in the $x-y$ plane. Atoms are free to move along the z-direction since they are not subject to a restoring force.

the background gas. Atoms with high longitudinal velocity v_ℓ which are not sufficiently transversely cooled are filtered by the aperture. Elliptically shaped laser beams increase the interaction time of atoms in the 2D light field and hence enhance the flux of atoms in the atomic beam. However this is done at the expense of a higher longitudinal velocity of the atomic beam and a broader longitudinal distribution of the velocity [33]. By applying a laser beam along the $+z$ direction called pusher laser beam as sketched in Figure 4.3, the width of the distribution of velocity is reduced because atoms with low velocities in the distribution are shifted towards higher value. This enables also to increase the flux of the atomic beam by cooling atomic motions propagating in the $-z$ direction until their trajectories are reversed in the $+z$ direction. The longitudinal velocity of atoms is determined by the intensity of the pushing beam, which accelerates the atoms in the two dimensional cooling and trapping potential. The atomic and laser beams overlap up to the optical collimation region, where they are separated for example by tilting the pusher beam. This prevents atoms to be more accelerated and also eliminates all heating

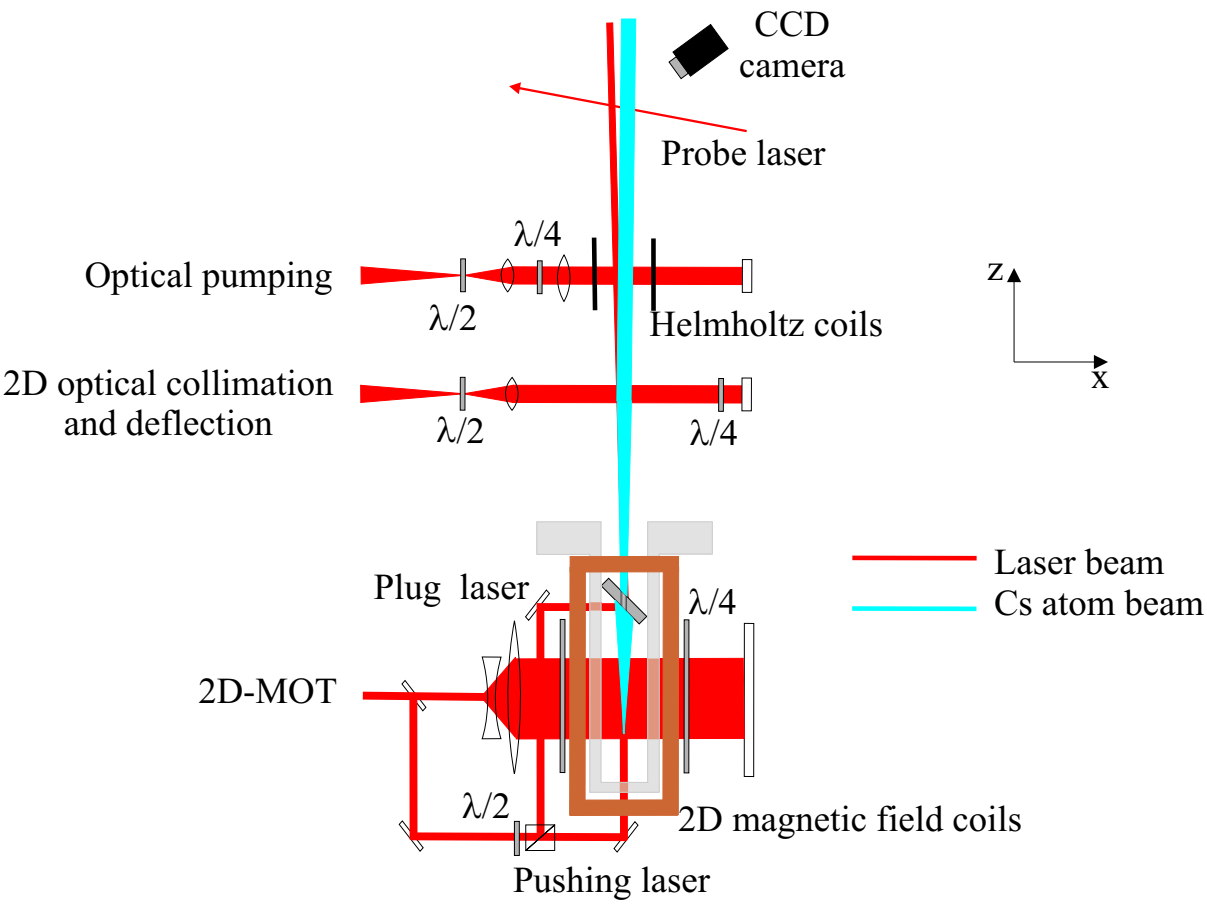

Figure 4.3: Sketch of the slow atomic beam originating from a 2D-MOT. The plug laser beam shuts off the atomic beam and enables the optimization of the atomic density in the 2D-MOT.

effects leading to a transverse spread of the atomic beam. In our setup the pushing beam polarization (σ^+) and intensity (2.96 mW/cm^2) was adjusted so that the atomic beam flux is maximum. In principle, reducing the intensity as well as changing the detuning of the pusher should increase the number of slow atoms in the beam as outlined in [26, 33]. In order to obtain a narrow longitudinal distribution of velocity, an additional laser beam propagating in the $-z$ direction can be applied [27]. With a different laser beam intensity and a separate detuning from the $+z$-axis propagating laser beam the longitudinal velocity of the atoms is cooled and can be controlled so that slow velocity can be obtained. This can be however unsuitable in our experiments because it leads to a higher divergence of the atomic beam while a well collimated beam is desired.
The divergence of the atomic beam is defined by the geometrical hole placed along the $+z$ axis. It turns out that the pusher beam reduces the transverse spread of the atomic beam. However the divergence of most of beams extracted from a 2D-MOT (from 30 to 50 mrad) are still too large for realizing reasonable experiments with magnetic mirrors. To improve the experimental conditions, a transverse cooling stage described in details below is necessary to reduce the divergence but also to enhance the atomic density of the atomic beam.

4.2 Experimental set-up

4.2.1 Vacuum system

The vacuum chamber is based on stainless steel crosses connected to an experimental chamber, as sketched in Figure 4.4. Two six-way crosses with a 35 mm inner diameter (CF 35) needed for optical transverse collimation and optical pumping are built along the vertical direction. They are separated at the top side from the experimental stage by a valve. A four way cross CF-35, which sustains a 70 l/s turbo-molecular pump and an electrical feedthrough is attached with the upper cross. The viewports are anti-reflection coated windows at the 852.3 nm i.e. the wavelength of the Cs-D_2 transition. The lower vacuum part carries an anti-reflection coated quartz glass cell with a dimension of ($30 \times 30 \times 142$) mm. It is related to the rest of the apparatus with an adapter consisting of a circular aluminum plate pressing strongly the base ($\varnothing = 75$ mm) of the glass cell by the mean of an helicoflex seal onto a reduction flange CF-35/64. There, a hole is drilled on the side, where a flexible bulk enables Cs atoms to reach directly the glass cell without affecting the upper part of the vacuum system. In front of the atom reservoir, a 270 l/s turbo-molecular pump and a Bayard-Alpert ion gauge are positioned face to face at the ends of the four-way cross.

Aluminum mirror

Extending in the glass cell as shown in Figure 4.5, a cylinder-trapezoidal shaped aluminum mirror fixed onto a copper ring isolates the glass cell from the rest of the apparatus. The hole in the mirror has a diameter of 1 mm, through which atoms from the 2D-MOT are free to travel. To use the surface of the aluminum mirror as an optical reflector for laser

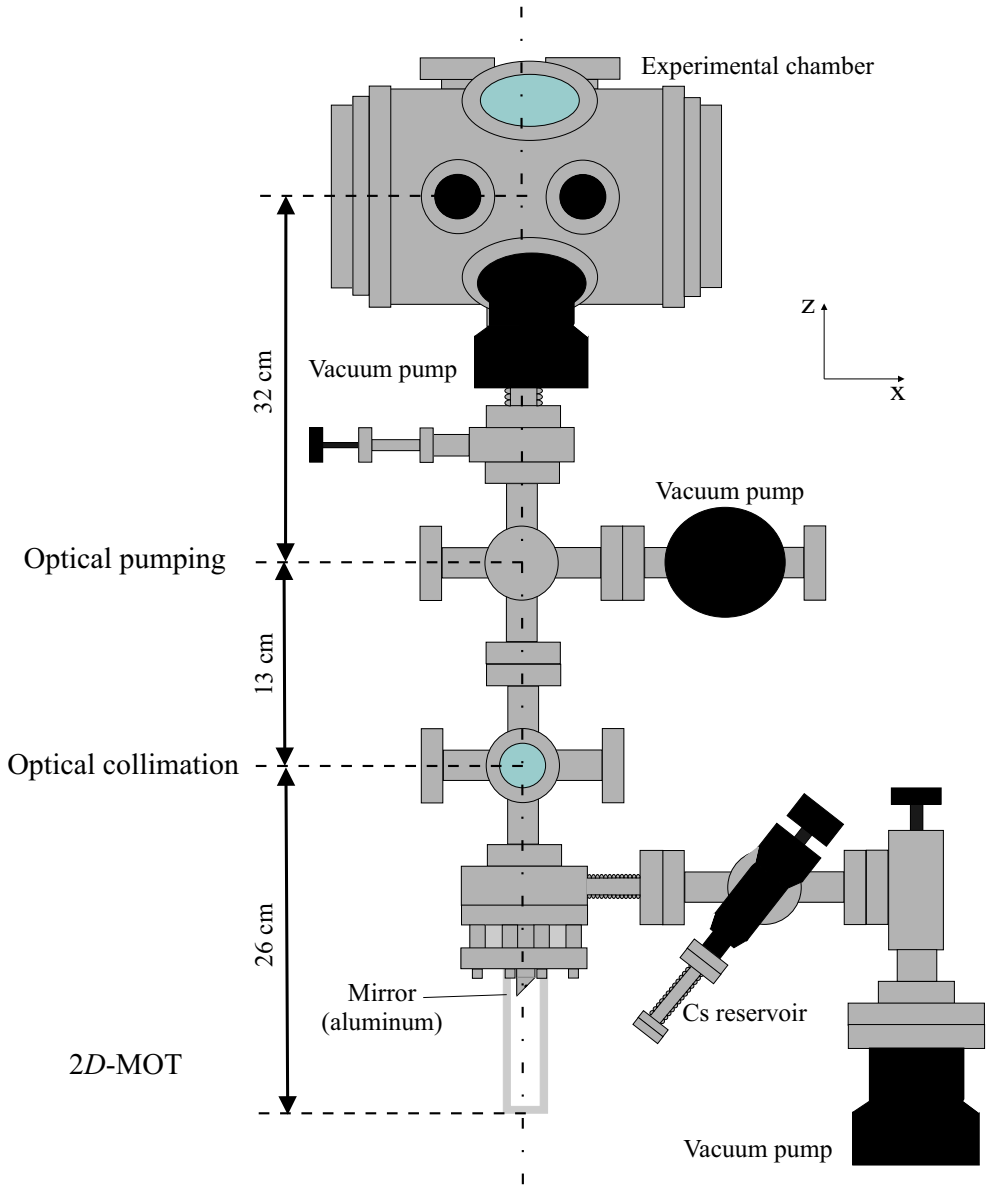

Figure 4.4: Mechanical assembly providing a low pressure environment. The differential pumping system at the bottom protects the rest of the apparatus from the Cs background pressure in the glass cell.

beams, we polished it first on rotating discs with grains of different sizes to remove material up to micrometer dimensions. Then, sub-micrometer roughness has been reached with a suspension of silicon dioxyde (SiO_2).
We tested the optical quality of the aluminum mirror by shining a helium-neon (He-Ne) laser of few milliwatts onto the surface. The reflected beam shows a diffuse behavior in the far field region but is still well collimated in the near field approximation, where the

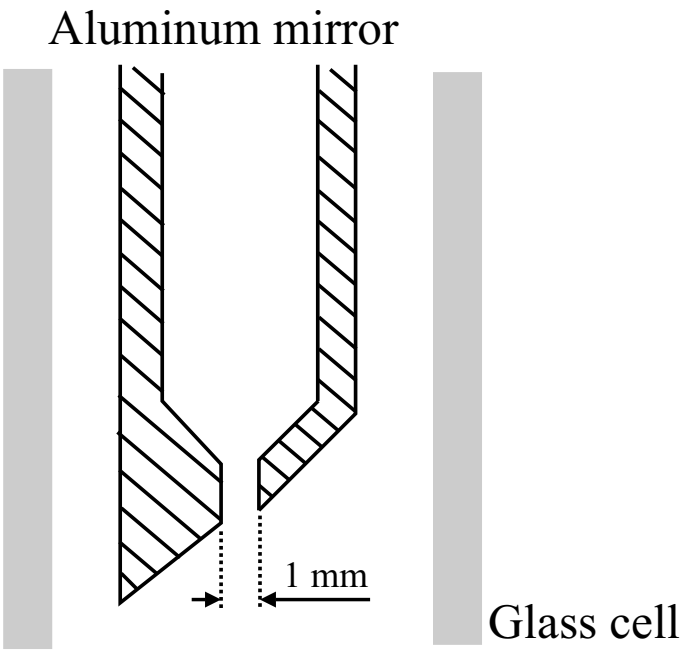

Figure 4.5: Aluminum mirror which reflects the plug beam at the center of the glass cell and enables to observe the atoms in the 2D-MOT. Without the plug beam, atoms leave the glass cell through the 1 mm hole.

intensity of the reflected laser beam is more than 70 % of the incident beam. However, the macroscopic shape of the surface is not flat as expected because during the sub-micrometer polishing process, the aluminum mirror has not been fixed very strongly.

Cesium reservoir

To feed our apparatus with Cs, we placed a Cs-ampoule in a vacuum bulk. The whole is connected to a valve, which prevents to affect the vacuum system with air by recharging the cesium reservoir. By twisting the bulk containing the cesium ampoule, the glass is broken and it permits to release cesium atoms in the apparatus. We heated the reservoir up to 50° C in order to increase the vapor pressure and thus to accelerate the evaporation of atoms. This method does not offer enough flexibility to control the background vapor pressure of Cs in the vacuum. A more suitable device can be the use of commercial dispensers (SAES Getters by example), which emit atomic cesium only when a current is applied. The flux of atoms from the dispenser can be controlled in a proper way [29].
Due to our special mechanical construction, atoms from the reservoir need few days to migrate up to the cell. The flow of atoms along the aluminum mirror in the glass cell creates a background gas. The small hole in the aluminium mirror prevents the gas to spread out in the whole apparatus. Indeed, in the upper part of the apparatus, delimited at the bottom by the hole, a high vacuum quality is maintained with typical value pressure as high as 2×10^{-9} Torr, whereas the lower chamber has a pressure of 5×10^{-9} Torr with

Cs as background gas.

4.2.2 Laser systems

The diode lasers used in this experiment have been described in details in the last chapter. We built also a laser diode with an output power of 150 mW, which is called "cooling and trapping" laser. As frequency reference, we use a master laser locked to the Cs transition $|6S_{1/2}, F = 4\rangle \rightarrow |6P_{3/2}, F' = 5\rangle$ by a polarization spectroscopy .
The laser beams are coupled into monomode polarization maintaining optical fibers. To avoid optical pumping into the hyperfine state $|F = 3\rangle$, a pump laser resonant with the $|6S_{1/2}, F = 3\rangle \rightarrow |6P_{3/2}, F' = 4\rangle$ transition is superimposed to the cooling laser by the mean of the optical fiber. For each stage as shown in Figure 4.3 a cooling and a pumping laser are needed.

4.3 2D-MOT

The heart of the experiment is the 2D-MOT, which feeds continuously the slow atomic beam with atoms. With the discussion on the 2D-MOT above, we present in the following

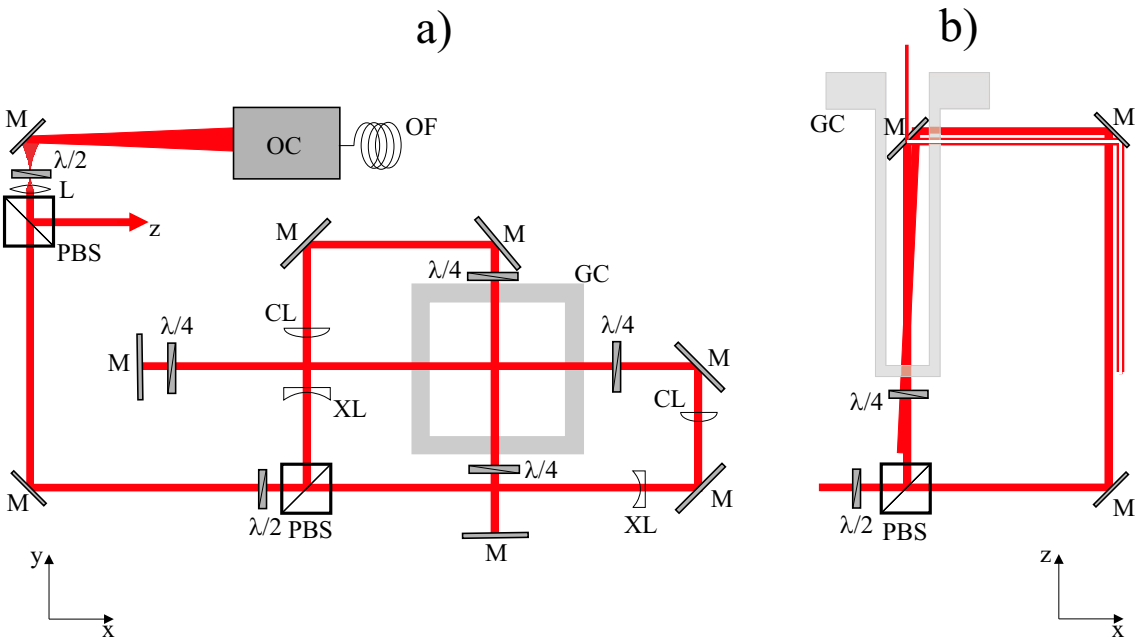

Figure 4.6: Optical setup for the 2D-MOT. The glass cell (GC) is represented. a) In plane configuration where the laser beams are expanded with cylindrical telescopes. This enables to collect many atoms along the z axis. b) The vertical configuration. The plug beam and the pusher beam are sketched as well as the generated atomic beam. OF: optical fiber, OC: fiber out coupler, M: mirror, L: lens, PBS: polarized beam splitter, XL: cylindrical divergent lens, CL: cylindrical convergent lens, $\lambda/2$: half-wave plate, $\lambda/4$: quarter-wave plate.

the practical application of the principle.

4.3.1 Optical setup

The laser system consists in a cooling laser beam $|\, F = 4 \,\rangle \rightarrow |\, F' = 5 \,\rangle$ (20 mW) superimposed to a pump laser $|\, F = 3 \,\rangle \rightarrow |\, F' = 4 \,\rangle$ (600 μW). The laser beam from the optical fiber is expanded to a diameter of 5 mm with a lens of focal length $f = 90$ mm. The well collimated beam is split into two main beams called the in-plane beam ((x, y) plane) and the vertical beam (z direction). Figure 4.6 a) shows the in-plane beam configuration. A second polarizing beam splitter gives two equally strong beams, which are expanded vertically through a telescope with cylindrical lenses ($f_1 = 150$ mm, $f_2 = -25$ mm). The 5×30 mm beams are circularly polarized and cross inside the glass cell. Each one is reflected back in the opposite direction and quarter wave plates in front of the end mirrors generate the desired polarization configuration needed to cool atoms up to the sub-Doppler regime.
The vertical laser beams are sketched in Figure 4.6 b). The laser beam reflecting first on the aluminum mirror before arriving at the center of the glass cell is called the plug beam. Since the 1 mm hole is located at the center of the aluminum mirror the plug beam is tilted to few degrees in order to observe the trapped atoms emitting fluorescence along the z-axis.

4.3.2 $2D$-MOT coils

The restoring force exerted on the atoms requires an inhomogeneous magnetic field. The Cs vapor cell from which the atomic beam is extracted is located inside four racetrack-shaped magnetic field coils. These produce a two-dimensional quadrupolar magnetic field and trap atoms along the axis of symmetry z. In this third direction, atoms are only pushed and not trapped.
In practice, a 0.75 mm diameter isolated copper wire is wound around the four faces of an aluminum holder (see Figure 4.7), which ensure a symmetric magnetic field around the z-axis. Each face holds 60 wire turns, i.e 120 wires for each racetrack. The coil setup allows a single current to flow along the edges of the holder in an alternating current configuration, and creates the desired two-dimensional quadrupolar magnetic field. The aluminum wire holder has been built in such a way as to contain the glass cell in its center part with an inner dimension of 32×32 mm. We fixed it to a mirror holder and the whole to a (x, y)-micrometer positioning system, which enables to adjust the magnetic field minimum with respect to the symmetry axis. Rather than using homogeneous magnetic fields for compensating for the zero magnetic field, we prefer to use the micrometer mechanical adjustment due to its stability. The design of the aluminum holder has been chosen, so that the wires are as close as possible to the cesium vapor cell. In this way, high gradient magnetic fields are reached with small currents.
During experiments, we applied typical currents of 2.5 A. The calculation around the minimum of the magnetic field gives a gradient field of $|\overrightarrow{\nabla} B| = 12.4$ G/cm. Experimental measurements provide a gradient field of $|\overrightarrow{\nabla} B| = (14 \pm 1)$ G/cm. Such currents induce

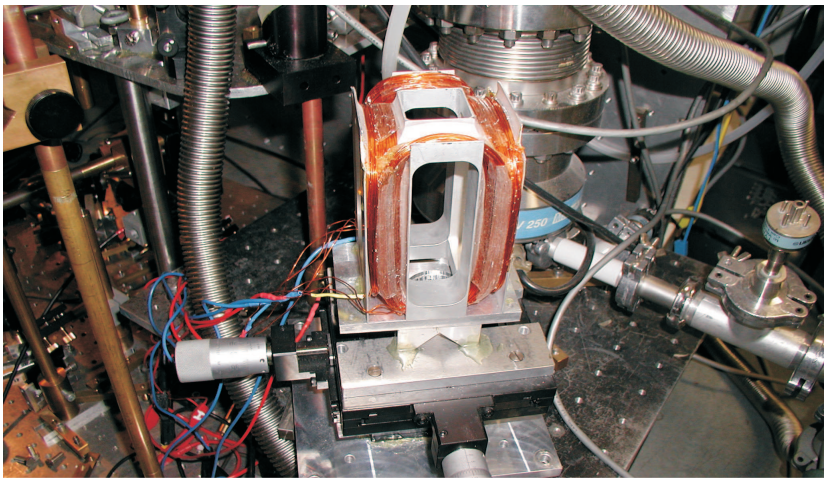

Figure 4.7: Picture of the racetrack-shaped magnetic field coil wound in the aluminum holder. The current flowing through the coil drives the resulting magnetic field on each side.

heating effect, however air flow convection between glass cell and aluminum holder is sufficient to dissipate the heat created by the coils.

4.3.3 Source of slow atoms

With the optical and the magnetic systems, we are able to observe the atoms trapped from the background gas. The fluorescence emitted by atoms was collected by a real time camera and is shown in Figure 4.8. We see an elongated atom cloud with a length of

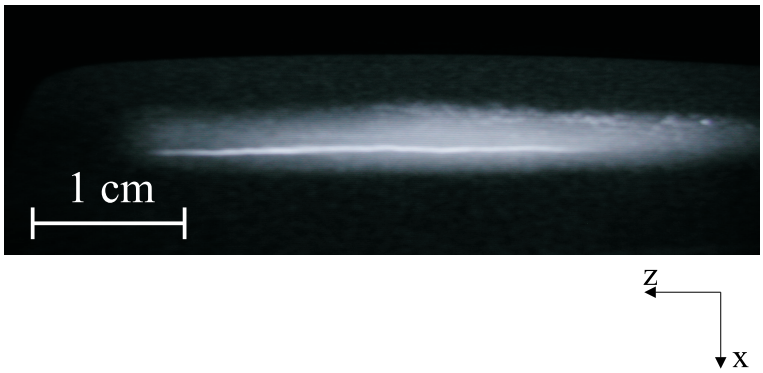

Figure 4.8: Photograph of the 2D-MOT with the plug laser beam on. In the center, the cigar formed atom cloud is surrounded by the fluorescence from the background Cs gas.

30 mm in the potential minimum created by the elliptically shaped laser light and the two-dimensional magnetic field. The maximum number of trapped atoms is obtained at a laser detuning $\delta_L = -2\Gamma$, with Γ the Cs natural linewidth and a magnetic field gradient of 12.4 G/cm.
The fluorescence intensity increases with the background atom density and then saturates. For very high densities the MOT is destroyed due to the collisions.
By blocking the plug beam, atoms are forced out of the trap so that slow atoms propagate through the 1 mm hole in the aluminum mirror and form an atomic beam. Without the plug beam, we could still distinguish atoms in the $2D$-MOT potential due to the radiation pressure of the pushing beam. To optimize the flux of atoms we easily adjust the MOT position by moving the magnetic field null point of the anti-Helmholtz coils. We detected the atoms by shining a laser beam of few mW placed 15 cm above the hole and perpendicular to the atomic beam. The emitted photons are detected by a photo-multiplier tube (PMT). We estimated roughly the atomic beam diameter and found typical diameter of $\sim 7 - 8$ mm. During the propagation the atomic beam undergoes a constant expansion and the reflected atoms cannot be separated from the incident atomic beam. To avoid such complications, we reduce the atomic beam diameter in the experimental chamber by decreasing its divergence with an optical transverse collimation. This leads also to a higher number of reflected atoms.

4.4 Optical transverse collimation

4.4.1 Principle

The expansion of our cold atomic beam along the 64 cm propagation distance turns out to be problematic for reflecting atoms onto magnetic mirrors. Indeed, atoms leaving the 1 mm diameter hole from the glass cell are subject to a transverse velocity selection through the 8 mm hole of the magnetic shielding located 29 cm downstream. These physical apertures delimit the atomic beam width. A calculation leads to a divergence of 15.5 mrad and thus to a beam diameter of 18.9 mm in the probe region. A transverse collimation with an optical molasses, 49 cm below, is realized which reduces the atomic beam diameter to 3.7 mm in the two dimensional collimation stage. This is realized by the same method described in the Zeeman-slower experiment, where atoms in a polarized standing wave are transversely sub-Doppler cooled in order to reduce strongly the divergence of the atomic beam.

4.4.2 Optical setup

The optical molasses is realized with a cooling and a pump laser in a retro-reflecting configuration. The linear polarized laser beam is expanded up to 10 mm in diameter with a lens of focal length $f = 120$ mm. A half wave plate turns the polarization direction to 45° relatively to the atomic beam axis. In a single laser beam arrangement as sketched in Figure 4.9, two pairs of counterpropagating beams cross at the center of a six-way cross. A quarter wave plate, mounted before retroreflection on the last mirror, rotates the laser

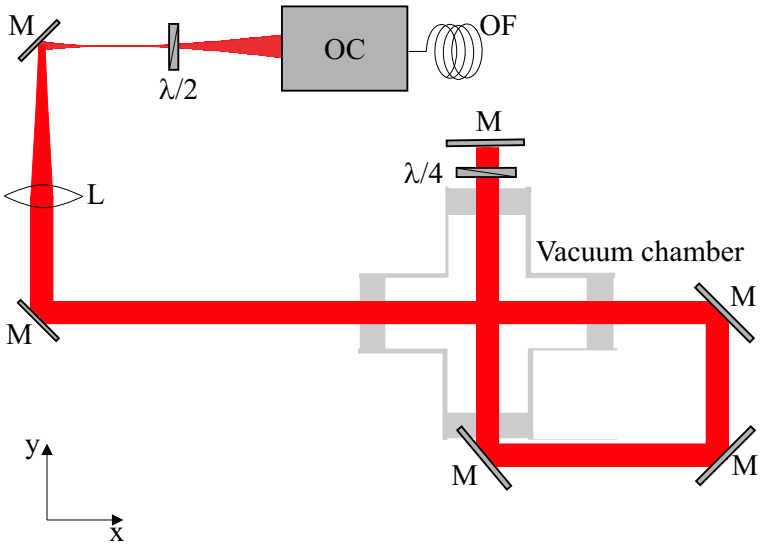

Figure 4.9: Two dimensional transverse collimation of the atomic beam. OF: optical fiber, OC: fiber out coupler, M: mirror, L: lens, PBS: polarized beam splitter, L: convergent lens, $\lambda/2$: half-wave plate, $\lambda/4$: quarter-wave plate.

polarization by 90°, allowing a *lin* $\perp$ *lin* configuration for sub-Doppler cooling. A laser beam with a power of 650 μW is superimposed to the 23 mW collimating laser beam and pumps the atoms from the $|\,F=3\,\rangle$ back to the $|\,F=4\,\rangle$-state in order to undergo laser

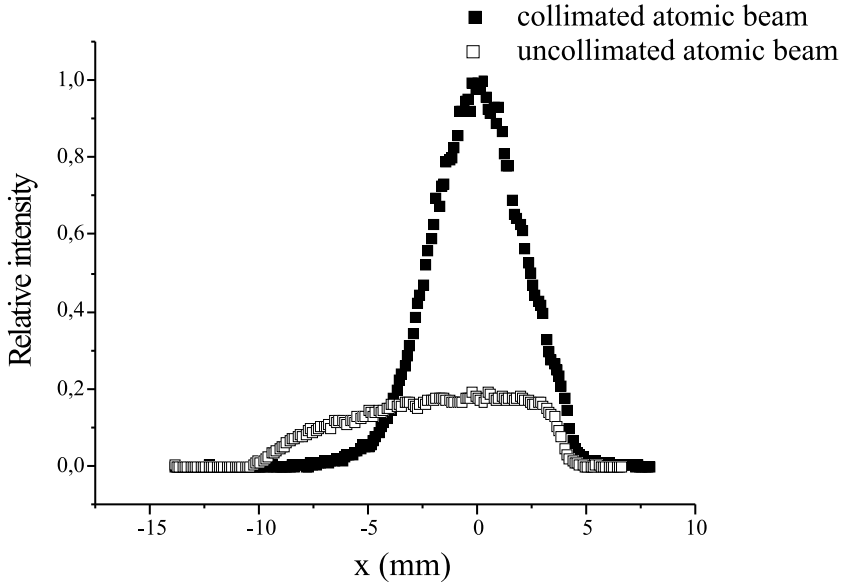

Figure 4.10: Relative intensity of atoms that have been transversely collimated. The uncollimated atomic beam is truncated by the hole in the μ-metal shielding (see Section 4.5 and by the holder of the atomic mirror.

cooling. The collimation process is not disturbed by the magnetic field generated by the MOT located 20 cm upstream.
By tilting the 2D-collimation laser beams to few degrees with respect to the $x - y$ plane, the atomic beam is deflected and hence separated from the on-axis pusher beam.

4.4.3 Results

Typical spatial profiles of the uncollimated and collimated atomic beams are shown in Figure 4.10, where the fluorescence intensity is normalized to the collimated beam maximum intensity. We see that the uncollimated beam is truncated at distances of -8.5 mm and 3.2 mm from the beam center. The first feature originates from the edge of the magnetic shielding hole, whereas the second more obvious results from the intersection of the atomic beam with a holder inside the experimental chamber. This last complication was avoided by tilting the collimated beam, which presents however, a slight truncation about 3.5 mm. We obtain the beam diameters by considering only the points where $x < 0$ and then we mirror them for $x > 0$. We find a width FWHM=(15.6 ± 2.4) mm for the uncollimated atomic beam, which is consistent with the expected theoretical calculation. The width of the collimated beam corresponding to 4.9 mm enables us to determine the atomic beam divergence, which corresponds to an angle of $\Delta\Omega = 1.2$ mrad. With a longitudinal velocity of 20 m/s, we find a transverse velocity spread $v_t = 2.4$ cm/s.

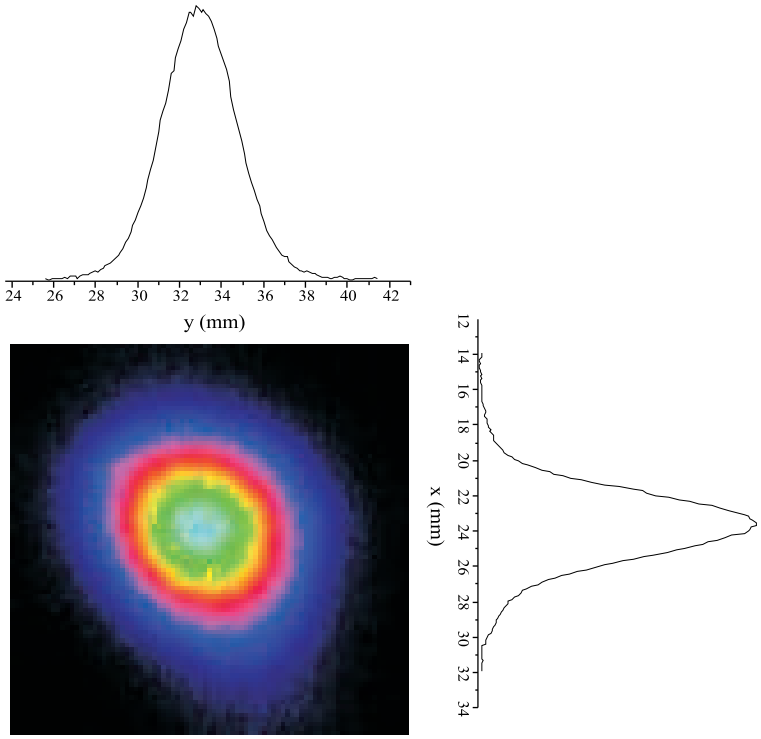

Figure 4.11: 2D-fluorescence profile of the collimated atomic beam.

The atomic beam density is also enhanced up to a factor of 5 (Figure 4.10). In Figure 4.11, we have represented the well collimated atomic beam which is tilted in order to avoid any defect in the beam.

4.5 Optical pumping

The optical pumping principle has been described in details in Section 3.1.3 of the last chapter.

4.5.1 Principle

The atoms leaving the optical collimating zone are distributed among the m_F sublevels of the $|F = 4\rangle$ ground state. The optical polarization region is protected by a magnetic shielding tube against the earth magnetic field and any other stray fields. The magnetic shielding is 100 mm long with a diameter of 33 mm. Two 8 mm diameter holes enable the atomic beam to enter and to leave the optical pumping zone, as shown in Figure 4.12. The cylindrical shielding is made of a mu-metal which has been demagnetized in a strong alternating magnetic field. The residual magnetic field inside the cylinder is smaller than 0.20 μT. Inside the shielding a pair of coils in a Helmholtz configuration generates a small homogeneous field of few mT defining the quantization axis.
A 10 mm-diameter laser beam is circularly polarized and crosses the atomic beam 140 mm upstream from the collimation stage. The σ^+-polarized laser beam with a power of 550 μm

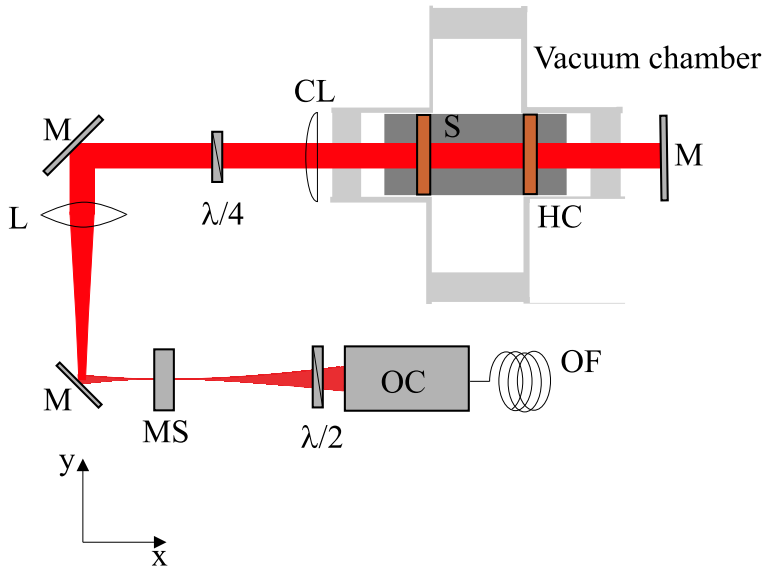

Figure 4.12: Optical pumping of the atomic beam in the dark state $|F = 4, m_F = +4\rangle$.MS: mechanical shutter, OF: optical fiber, OC: fiber out coupler, M: mirror, L: lens, CL: cylindrical convergent lens, $\lambda/2$: half-wave plate, $\lambda/4$: quarter-wave plate, HC: Helmholtz coils, S: μ-metal shielding.

is tuned to the $|F=4\rangle \rightarrow |F'=4\rangle$ transition, whereas the 250 μm pump laser to the $|F=3\rangle \rightarrow |F'=4\rangle$. After a multiple absorption-emission process, the atoms are transfered to the $|F=4, m_F=+4\rangle$ dark state. The laser beam is retroreflected avoiding all effects due to the radiation pressure, as shown in Figure 4.12.

4.5.2 Results

The distribution of atoms in the $|F=4\rangle$ hyperfine level can be probed by implementing the "Stern-Gerlach" experiment. Indeed, the atomic beam entering an inhomogeneous magnetic field is deflected depending on its internal m_F-state (see Chapter 2). To realize this effect, a 2-cm-long permanent magnet is brought near the atomic beam, 16 cm after the optical pumping region. Atoms fly over a distance of 10 cm before reaching the optical

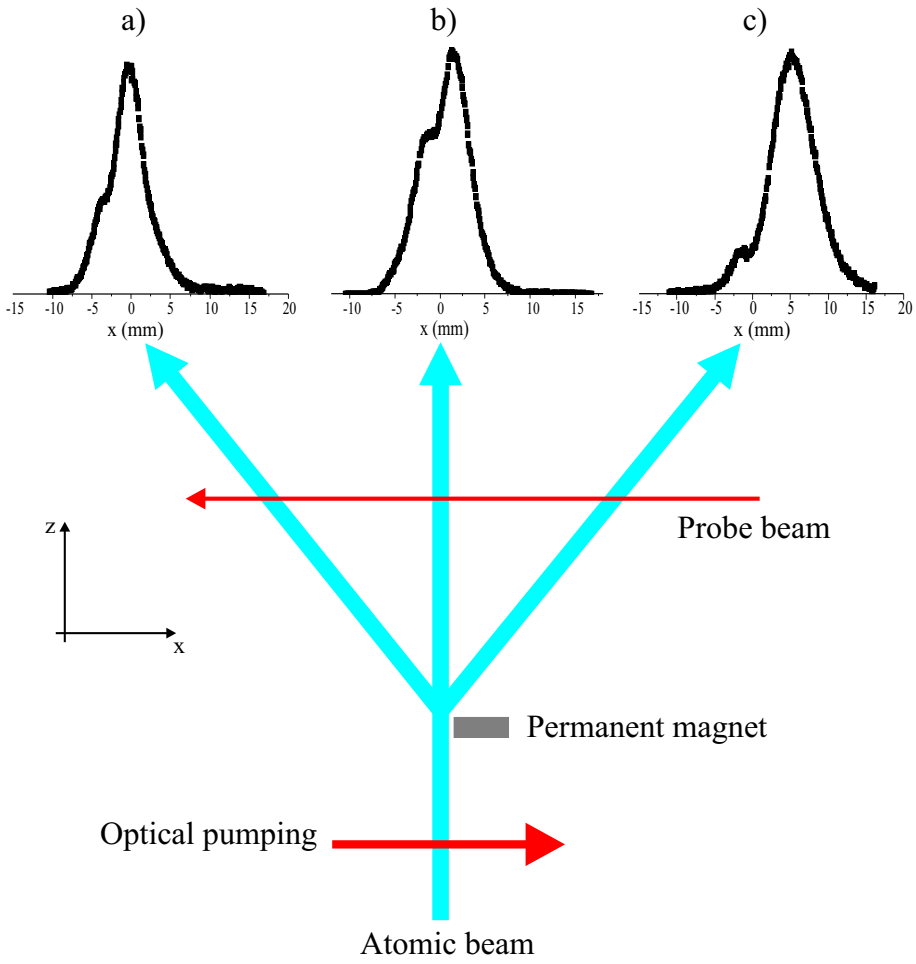

Figure 4.13: Plot of the relative flux of atoms depending on their position.a) σ^+-polarization. The atoms undergo a repulsive force. b) without optical pumping laser. The atomic beam is broadened due to the magnet. c) σ^--polarization. The atomic beam is attracted by the permanent magnet.

detection region.
Figure 4.13 b) presents the atomic distribution of the magnetic states after leaving the collimating and deflecting region. In this case, the optical pumping laser beam is shut down. The atomic beam is broadened and all m_F-states are situated between the extreme states $m_F = +4$ and $m_F = -4$. Each m_F-level could not be resolved due to the small flight distance between the permanent magnet and the probe laser.
We applied the circularly polarized laser beam and the small magnetic field created by the Helmholtz coils inside the magnetic shielding. We observed an optical pumping of atoms either in $m_F > 0$ states or in $m_F < 0$ depending on the position of the quarter wave plate. The polarization of the atomic beam is shown in Figure 4.13 a) and Figure 4.13 c) for the two positions of the quarter-half plate leading to σ^+ and σ^- laser polarization. In principle in the σ^- case, most of atoms are pumped in the $m_F < 0$ state while with the σ^+ most of them occupy the $m_F > 0$ states. Contrary to the optical polarization realized in the Zeeman-slower experiment, in this setup the low resolution does not allow to observe each m_F sub-states and this is essentially due to the small flight distance of atoms between the optical pumping zone and the detection region. However, experiments with magnetic videotapes enable us to optimize the reflected atomic beam so that most of the atoms are pumped in the $|\, F = 4, m_F = +4 \,\rangle$ state.

4.6 Atomic beam characterization

As seen in Chapter 2, the longitudinal velocity gives the maximal reflection angle for a magnetic mirror, the degree of monochromacity of the atomic beam is described by the longitudinal velocity distribution. The atomic beam profile is measured with a laser-induced fluorescence technique. Crossing the atomic beam at an angle of $(116.6 \pm 0.5)^\circ$ with respect to the direction of propagation, a CCD-camera collects the scattered photons ($|\, F = 4 \,\rangle \rightarrow |\, F' = 5 \,\rangle$) from a weak probe laser ($\varnothing \simeq 5$ mm), which intensity (1.5 mW) is chosen so that the fluorescence intensity is sufficient observable.

4.6.1 Gravitation effect

In our study, we neglect all gravitational effects and the particles, starting on an axis in the $2D$-MOT, travel on straight line trajectories. For example, an atom with initial velocity $v_{\ell i}$ moving in an atomic beam undergo a constant gravitational deceleration $\overrightarrow{g}$ over a height h. The final velocity $v_{\ell f}$ is given by $v_{\ell f} = \sqrt{v_{\ell i}^2 - 2gh}$. For $v_{\ell i} = 20$ m/s and $h = 1$ m, we find $v_{\ell f} = 19.5$ m/s. In this work, the experimental conditions are always satisfied by the inequality $\sqrt{2gh} \ll v_{\ell i}$ so that the initial velocity defines the velocity of the atomic beam. Therefore, the analysis of magnetic systems for reflection is realized by considering the motion of an atom equivalent to that of a light ray. The path l followed by an atom is simply $l = v_\ell t$, where t is the time. However for very cold atoms, the contribution of the gravity is non-negligible and has to be taken into account [17].

4.6.2 Longitudinal velocity distribution

The velocity of the atomic beam is first measured with a Doppler-induced fluorescence technique. The probe beam is frequency-scanned across the atomic beam transition ($|\,F=4\,\rangle \rightarrow |\,F'=5\,\rangle$) and induces a maximum fluorescence for a detuning of (9.6 ± 1.4) MHz corresponding to a longitudinal velocity ($v_\ell = 18.7 \pm 2.7$) m/s. Indeed, the determination of the distribution is limited by the broadened natural linewidth γ of the Cs atomic excited state [22] and it follows a resolution limit of $\Delta v_\ell = \lambda \cdot \gamma / \cos\theta\sqrt{1+s}$. With $\lambda = 852.3$ nm, $\gamma = 5.2$ MHz, $\theta = 26°$ and $s = I/I_0$, $I = 25.5$ mW/cm^2 and I_0=1.1 mW/cm^2, we find $\Delta v_\ell = 49.7$ m/s.
We investigate deeper the velocity distribution by a time-of-flight (TOF) measurement [20]. A laser light sheet realized by focusing the laser with a cylindrical lens (120 μW) and resonant with the $|\,F=4\,\rangle \rightarrow |\,F'=4\,\rangle$ transition is focused on the atomic beam and pumps atoms in the $|\,F=3\,\rangle$ ground state. The light beam is cut off periodically (square signal, period T=1.8 Hz) by a fast mechanical shutter. After a flight distance of 40 cm, a laser beam probes the transition $|\,F=4\,\rangle \rightarrow |\,F'=5\,\rangle$ of the atomic beam. A photomultiplier collects the scattered photons.
The time reference signal is given by the driver signal of the mechanical shutter. When the pump beam is turned off and on, we visualize the time dependent decreasing and increasing fluorescence signal, which informs about the arrival time of atoms in the probe laser beam. The signal is averaged on a long time scale so that a measurement can be taken. Otherwise the signal disappear totaly because the dominant contribution is the stray light from the laser beam. Although a weak TOF signal, we could extract information on the longitudinal distribution of velocity. We find a velocity spread $\Delta v_\ell = 2.4$ m/s centered on the mean velocity $v_\ell = (21.5 \pm 2)$ m/s.

Chapter 5

Atomic focusing by a curved magnetic reflector

In the previous chapter we described our new source of slow atoms enabling us to generate a well collimated atomic beam optically pumped in the states $m_F = +4$ which is repulsive in an inhomogeneous magnetic field. The atoms impinging on a curved magnetic reflector are incident at larger angles compared with those presented in Chapter 3. This offers a new possibility for focusing the atomic beam and hence to study the image-formation properties of a curved videotape. This opens new perspectives in atomic beam imaging with reflective optics.

5.1 Principle

5.1.1 Focusing with a spherical mirror

The main goal of this experiment is to focus an atomic beam by reflections on a curved reflector as sketched in Figure 5.1. Atoms moving towards a spherical magnetic mirror experience the magnetic force $\mu_0 k B_0 e^{-ky}$ which causes them to be concentrated to a common point called f (Figure 5.1 a)). The image formation of an atomic beam incident at an angle α on a cylindrical reflector with a radius of curvature R is given by Equation (A.17) in Appendix A as

$$f = \frac{R}{2} \sin \alpha, \tag{5.1}$$

where α is the angle of incidence defined by the central ray of the atomic beam and the curved reflector. The focus point $f_0 = R/2$ corresponds to the focus of atoms at near normal incidence angles, which can be reached either with higher magnetic barrier intensity B_0 or with smaller longitudinal velocity v_ℓ. The focus f is well defined providing that the chord D subtended by the angle β at the curvature center of the spherical mirror is much larger than the chord d defined by the diameter of the atomic beam arriving onto the surface of the magnetic mirror shown in Figure 5.1 b), i.e

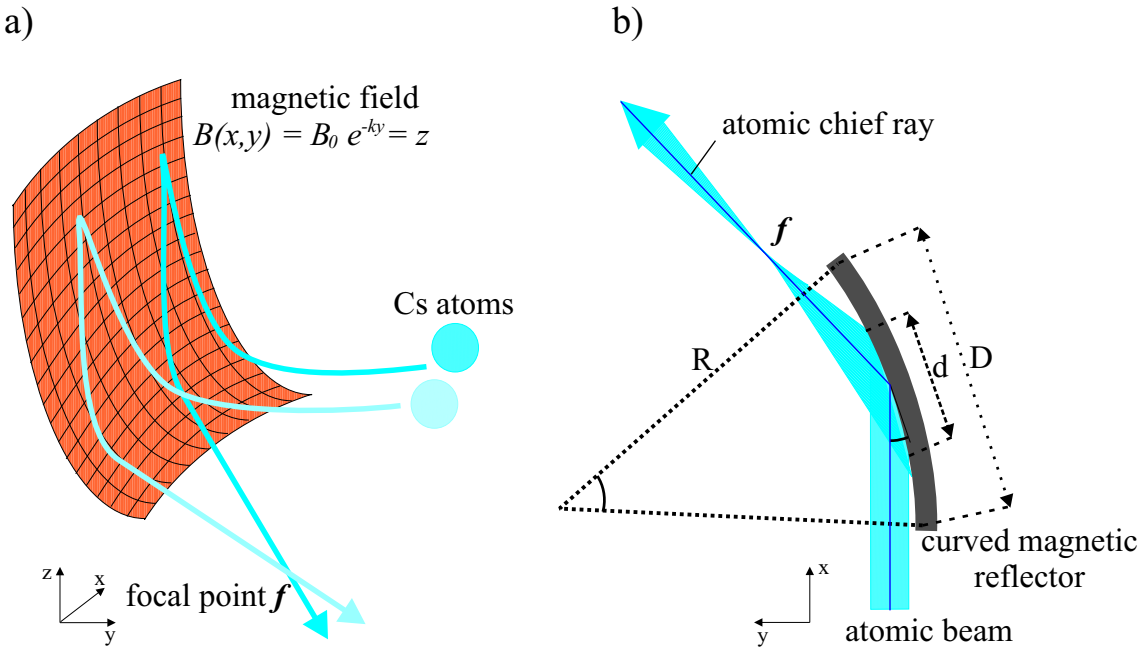

Figure 5.1: Focusing of atoms with a curved magnetic reflector. a) Atom trajectories of 2 atoms undergoing the repulsive magnetic force which cause them to cross at the point f. b) The atomic beam incident at an angle α is reflected on a mirror and focused at a distance f from the turning point on the reflector.

$$d \ll D. \tag{5.2}$$

At grazing incidence (α few mrad), the focus is not well-defined because in general the condition $d \ll D$ is not fulfilled. Other effects, like multiple reflections (see Chapter 3) also appear.
For our 2D-MOT-based atomic beam of velocity $v_\ell = 18.7$ m/s with $B_0 = 53$ mT, the maximum angle of reflection is $\alpha_{max} = 6.5°$ (see Equation (2.6)). Atoms arriving at the surface of the mirror with angles $\alpha < \alpha_{max}$ are focused. Atoms striking the reflector at larger angles hit the surface and are lost.

5.1.2 Caustic of a spherical reflector

Atoms in a collimated atomic beam arriving at small incidence angle extend over a large area on the reflector and reach the surface at different positions. Due to the curvature of the mirror each atomic trajectory is deflected at another angle depending on the point of impact onto the reflector. Thus, depending on the location of atoms in the atomic beam, we define focal points f_i with respect to the impact points of atoms on the magnetic surface. We rewrite Equation (5.1) as

$$f_i = \frac{R}{2}\sin(\alpha + \frac{\beta_i}{2}), \tag{5.3}$$

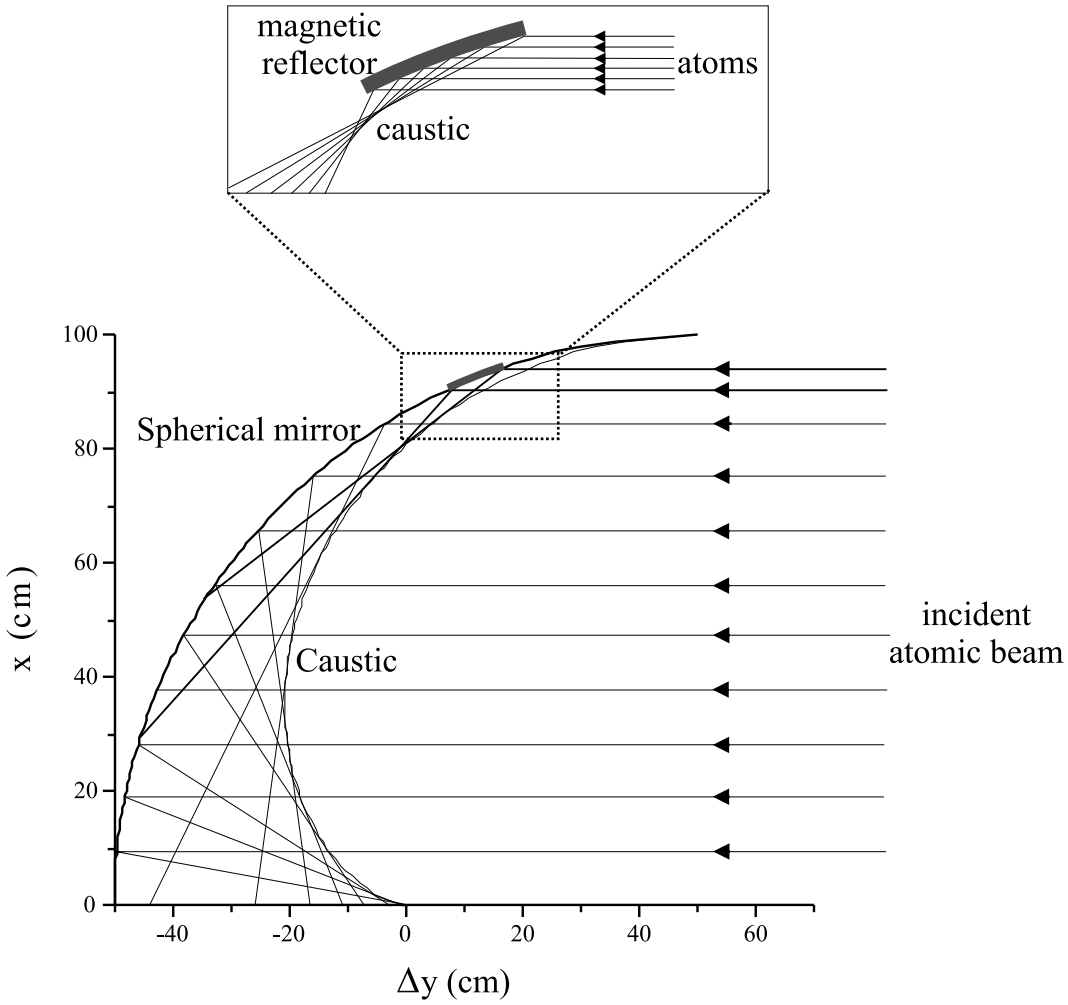

Figure 5.2: Aberrations of a spherical reflector with $R = 100$ cm. The inset shows the caustic formation for small angle of incidence.

where $\sin(\beta_i/2) = d_i/R$, R is the radius of curvature and d_i is the distance of the atom i with respect to the central atom in the atomic beam impinging on the mirror at angle an α. β_i is also the local curvature angle at which the atom i is expelled from the reflector. Consequently, $2\alpha + \beta_i = \alpha_{defl}$ where α_{defl} is the angle of the deflection of the reflected atomic beam from the incident one. Locally for a given trajectory, Equation 5.3 becomes

$$f_{loc} = \frac{R}{2}\sin(\frac{\alpha_{defl}}{2}). \tag{5.4}$$

Let's now consider our atomic beam divided into infinitely narrow parallel atomic rays. Each bunch of atom trajectory forms a separate focus in different directions in the (x, y) plane. The position of all foci given by Equation (5.3) or Equation (5.4) defines the so-called caustic. The axial distance $\Delta y = y_0 - y$ describes the displacement from the focus $f_0 = y_0 = R/2$ which is the caustic for an infinitely distant object source and is given by

[19]

$$\Delta y = \frac{R}{2}\{1 - [1 + 2(\frac{x}{R})^{2/3}]\sqrt{1 - (\frac{x}{R})^{2/3}}\}, \tag{5.5}$$

where x is the lateral coordinate of the focus points. Figure 5.2 presents the caustic formation for a collimated atomic beam incident onto the surface of a spherical mirror. The caustic function has been plotted with $R = 100$ cm. All reflected atomic trajectories are tangent to a single function described by Equation 5.5. This shows a strong concentration of atoms around this curve which gives the location point of the foci.
Let's now consider a spherical reflector with a curvature of few centimeters. Moving the reflector on the spherical curve plotted in Figure 5.2 is equivalent to vary the angle of incidence of the atomic beam. This means, on the other hand, that the caustic curve gives also the focus point evolution of the atomic beam from the paraxial approximation up to the grazing incidence regime. For example, for atomic rays incident on a 5 cm-long magnetic reflector at angles ranging from 19° to 21.5°, the caustic extends over a finite distance of ~ 9 cm. The first ray crossing the caustic is located ~ 11 cm from the point of reflection whereas the last ray reflected on the reflector crosses the caustic at a distance of ~ 14 cm. For a given length of the reflector, we observe that the extension of the caustic is reduced with larger angle of incidence. For $x \approx 0$ the function in Equation (5.5) converges towards $f_0 = 50$ cm and the image is free from any spherical aberrations as expected in the near normal incidence approximation.
The inset of Figure 5.2, which is a magnification of the reflector drawn on the spherical mirror, is more realistic in our experiments where the atomic beam is incident at small angles α. For these angles, the contribution to the caustic formation is limited to atoms reflected at points near the tangent defined by the curves of the spherical mirror and the caustic function as shown in Figure 5.2. The reflection of atoms show clearly the finite caustic formation generated by the intersection of the atomic trajectory at different points. In the three dimensional case the caustic is described as a combination of transverse and longitudinal spherical abberations.

5.1.3 Theoretical predictions

To understand further the behavior of atoms bouncing above the spherical reflector, we will consider the trajectory simulations of atoms leaving the magnetic reflector after one bounce and the case where atoms undergo multiple reflections.

Single atomic bounce

Figure 5.3 and 5.4 show the calculation of atomic trajectories where the condition (5.2) is first fulfilled and then violated. In these simulations, the slow atomic beam has a diameter of 5 mm. For the longitudinal velocity we have taken $v_\ell = 16$ m/s. We have carefully chosen the angle of curvature $\beta = 3°$ ($R = 101.2$ cm) so that the curved surface of reflection sustained by the chord d is close to the experimental conditions.
In Figure 5.3, we see that most of atoms incident at an angle $\alpha \sim 6.6°$ with respect to

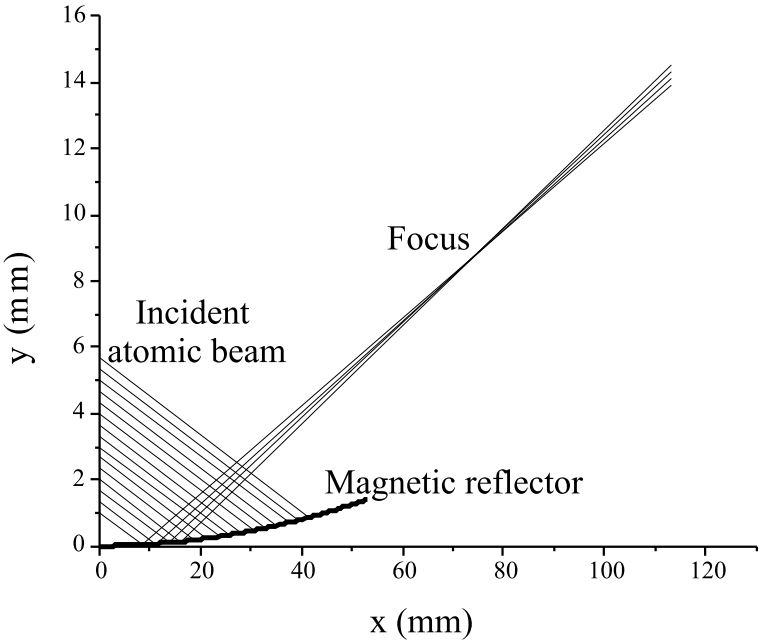

Figure 5.3: Focus of a reflected atomic beam on a spherical reflector with $R = 101.2$ cm and an angle of incidence $\alpha = 6.6°$ with respect to the x-axis. Atoms with $v_t > 2.1$ m/s stick on the mirror and are lost.

the x-axis are lost because they reach the spherical mirror with transverse velocities larger than the expected value $v_{t_{max}} = 2.1$ m/s allowed by the maximum magnetic field at the surface of the reflector (see Equation (2.6)). For a smaller parameter of impact, few atoms are still reflected and converge to a common point located at 63.6 mm from the point of reflection on the magnetic reflector. This distance corresponds to the trajectory realized by the atomic chief ray, defined as the reflected atom moving in the central part of the atomic beam. We notice the small dimension of the chord d relatively to D. Thus, by using Equation (5.4) with $\alpha_{defl} = 14.6°$, we find a focus point $f = 64.3$ mm which is consistent with the result of our simulation.

For $\alpha = 2.9°$, atoms are spread over the surface of the spherical mirror and most of them are reflected, as shown in Figure 5.4. The trajectories do not intersect anymore at the same point, each atomic ray presents a different direction of propagation. Depending on the atom's point of impact onto the reflector, the trajectories converge at different points as discussed previously in Section 5.1.2. The marginal trajectories, i.e the first and last reflected atoms, define the caustic curve where atoms are concentrated. This dark region do not enable one to find a single focus for the atomic beam. However, we can define a circle of least confusion (CLC), known also as waist, which corresponds to the minimum width of the reflected atomic beam. We have chosen the atomic chief ray corresponding to the atom which propagates in the central part of the atomic beam. Thus, this gives simply the focus f of the atomic beam. Together with the angle of deflection α_{defl}, we determine with Equation (5.4) the local radius of curvature R_{loc}. For $f = 40.5$ mm and

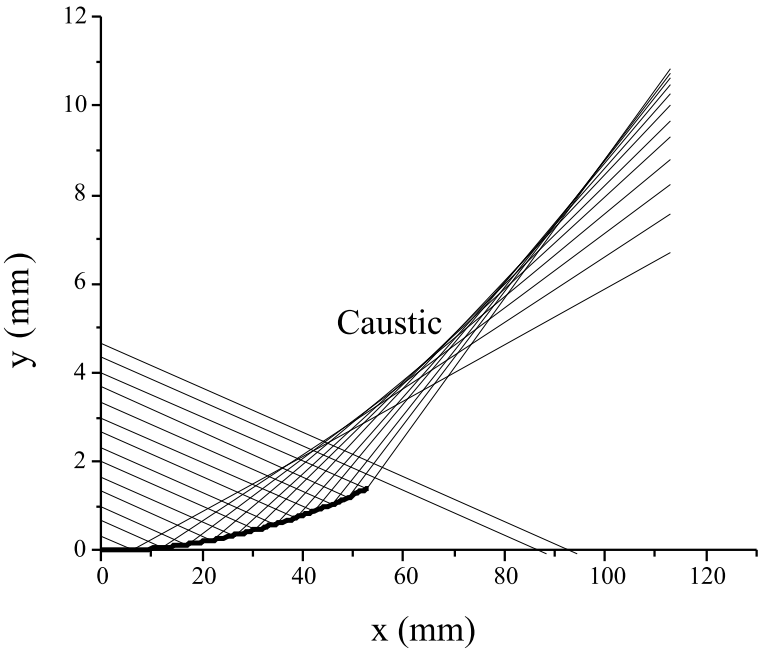

Figure 5.4: Simulation of the caustic generating from the trajectory of atoms with $\alpha = 2.9°$ and $R = 202.5$ mm.

$\alpha_{defl} = 9.6°$, we calculate $R_{loc} = 96.8$ cm which is in good agreement with the set value of 3° in our simulations for the curvature angle β of the spherical reflector.

Multiple atomic bounces

The whispering gallery regime in which atoms realize multiple bounces onto the surface of the magnetic mirror, is reached by increasing the angle of curvature of the reflector. For the simulation of the atomic trajectories, we have taken for the angle of incidence $\alpha = 70$ mrad (4°) and the angle of curvature is $\beta = 15°$ ($R = 202.55$ mm) while the atomic beam diameter is reduced to 2 mm for more clarity. Figure 5.5 shows the trajectory followed by atoms after being reflected on the curved reflector. Incident atoms with a large parameter of impact collide with the reflector and are lost. Those which survive their first reflection are focused at $f = 10.5$ mm inside the curved mirror. We can imagine how an atomic beam with a larger diameter prevent the observation of the focus because it is hidden by the incident atomic beam. We see clearly that the output atomic beam is separated into two groups of atoms. Some atoms reflect once and are deflected at $\alpha_{defl} = 12.2°$ whereas those which undergo a double reflection are deflected at a larger angle $\alpha_{defl} = 21.7°$, whose values are calculated for the atomic chief ray. In the far field region the two atomic beams diverge, which implies a broader atomic beam diameter along the direction of propagation of atoms. However the possibility to resolve separately the two atomic beams becomes more difficult as we approach closer to the extremity of the mirror. We recognize a strong concentration of atoms which are reflected twice. But it still stays not so obvious to find the minimum of the atomic beam width corresponding

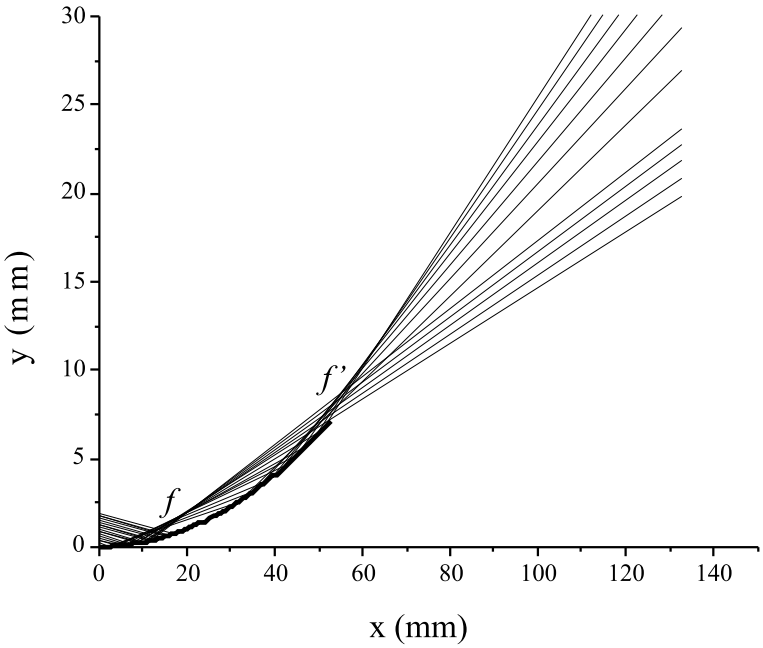

Figure 5.5: Atoms incident at $\alpha = 4°$ on the curved magnetic surface with $R = 202.6$ mm are focused by realizing one (f) or two bounces (f').

to the focus because the atomic trajectories are hidden by the transversal spreading of the atomic beam undergoing one reflection. With the simulation, we find a second focus point $f' = 11.97$ mm away from the second turning point of the atoms onto the magnetic mirror. We emphasized that Equation (5.4) is not valid for more than one bounce.

To reduce the aberrations when using magnetic spherical mirrors, it is necessary to use large incidence angles α and small atomic beam diameters or small angles of curvature β.

5.2 Experiments with the curved reflector

5.2.1 Experimental chamber

In the experimental chamber (see Figure 4.4), the atomic beam is reflected with the magnetic mirror shown in Figure 5.6. A molecular turbo pump evacuates the gas up to a residual pressure of 2×10^{-8} Torr. With the mechanical components of Figure 5.6, we found out a reduced quality of the pressure. Although the mirror assembly degas a non-negligible quantity of molecules in the vacuum environment, especially from our robust magnetic video tape into which adsorption occurs, this does not prevent us to perform the experiments.
The reflector set-up is similar to that used in the Zeeman-slowed atomic beam experiments and the same constraint on the maximum angle of reflection, due to the mechanical

construction, is still valid.

5.2.2 Magnetic reflector

The incidence angle of atoms is chosen by rotating the motor supporting the 5.5 cm long magnetic tape. With a feedthrough, we can adjust the transverse position of the atomic beam onto the mirror for a given angle as shown in Figure 5.6. By moving the rotatable table with a micrometer screw, we can define the atom's angles of incidence. A mechanical pusher enables to control the angle of curvature of the videotape, but the difficulty to read directly an absolute value of the radius of curvature leads us to implement indirect methods to reach this information. With the curved-shaped videotape, the magnetic surface depends on the quality of the mechanical surface so that any roughness provokes a distortion of the magnetic surface reducing the number of atoms in the specular reflection. The atomic beam originating from a $2D$-MOT (see Chapter 4) operates at standard characteristics during our experiments. These are given by the velocity $v_\ell = 18.7$ m/s with a width $\Delta v_\ell = 2.7$ m/s and the atomic beam divergence yields $\Delta\Omega = 1.2$ mrad. For a propagation distance of about 10 cm, we can neglect the divergence spread and consider the diameter $\varnothing = 5$ mm of the atomic beam as constant. Before being deflected on the magnetic reflector, the atoms are prepared in the $|\, F = 4, m_F = +4 \,\rangle$ state by optical pumping (see Chapter 3). A pair of coils in the Helmholtz configuration generates a hold field of few Gauss avoiding spin flips of atoms in others magnetic substates $m_F \neq +4$.

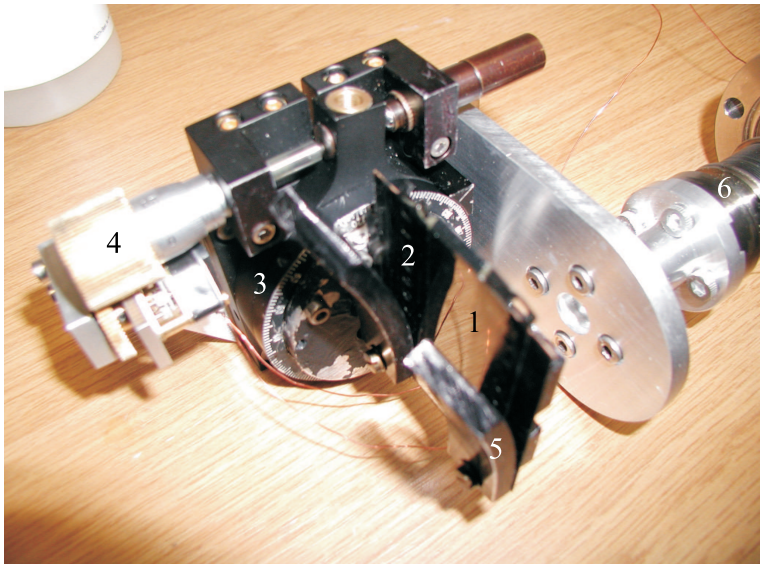

Figure 5.6: Mechanical assembly of the magnetic mirror. 1. Videotape. 2. Photographic film. 3. Rotatable table. 4. Micrometer screw. 5. Aluminum rail. 6. Mechanical vacuum feedthrough.

5.2.3 Effective surface of reflection

With the 53 mm-long magnetic mirror, the whole atomic beam with a diameter of 4.9 mm is reflected for angles above the threshold angle $\alpha_{th} = 5.3°$. There, by curving the mirror to the angle of curvature β, atoms that are closer to the end of the tape have a higher angle of incidence. All atoms in the atomic beam are reflected as long as

$$\beta + \alpha_{th} < \alpha_{max}. \tag{5.6}$$

From this condition, we deduce the maximal allowed radius of curvature R_{th} for complete reflection of the atomic beam. With $\beta = \alpha_{max} - \alpha_{thres}$ and $L = 53$ mm the length of the tape, we find $R_{th} = L/\beta = 26.5$ mm ($R_{max} = 96$ mm). For smaller R, the intensity of the reflected atomic beam decreases. To compensate for this effect, it is possible to reduce the angle of incidence $\alpha < \alpha_{th}$ and to move the relative transverse position of the mirror holder and the atomic beam. However for grazing incidence angles, we will be confronted to multiple reflections studied in the whispering gallery geometry in Chapter 3 which lead to a broad spatial distribution of the atomic beam at the output of the curved mirror. But the effect desired here is to focus atoms after possibly one reflection on the magnetic video tape.

5.2.4 Detection of atomic beam trajectories

Atoms in the atomic beam which are reflected traverse a probe laser beam with an intensity $I = 40I_s$ ($I_s = 1.1$ mW/cm^2) is the saturation intensity of Cs) at an angle of 116.6° with respect to the direction of propagation of the atoms. Scanning longitudinally and transversally the probe laser along the atomic beam reveals the track of atoms. The Doppler shift is compensated by tuning the frequency of the probe laser at the maximum fluorescence intensity for the different positions. Figure 5.7 is a sketch of the fluorescence emitted by atoms which permits to image the path of the reflected atomic beam using a CCD camera located 32 cm out of page. We call original beam the atomic beam which is not reflected, the whole original atomic beam appears when the videotape is completely moved at one side. The number of reflected atoms depends on the incidence angle of the atomic beam with respect to the magnetic mirror. For small angles, atoms which are not reflected constitute a small residual part from the whole original atomic beam.
All measurements are taken in the camera frame, i.e the system of coordinate depends on the orientation of the CCD camera. In the laboratory frame, the atomic beam propagates vertically as shown before in the Figure 4.3 of Chapter 4.
From pictures such that of Figure 5.7, we determine the angle of reflection of atoms by simply taking two points on the trajectory of the reflected atomic beam and two points on the original atomic beam. This makes easier to scale the angle of the magnetic reflector whose rotation is generated by a micrometer positioning system. Furthermore, by tracing the trajectories of the reflected beam and the original beam, we are able to find the turning point of atoms on the curved magnetic videotape. The scaled-images provide us the necessary measurements to calculate, using Equation (5.3), the local radius of curvature where atoms are reflected.

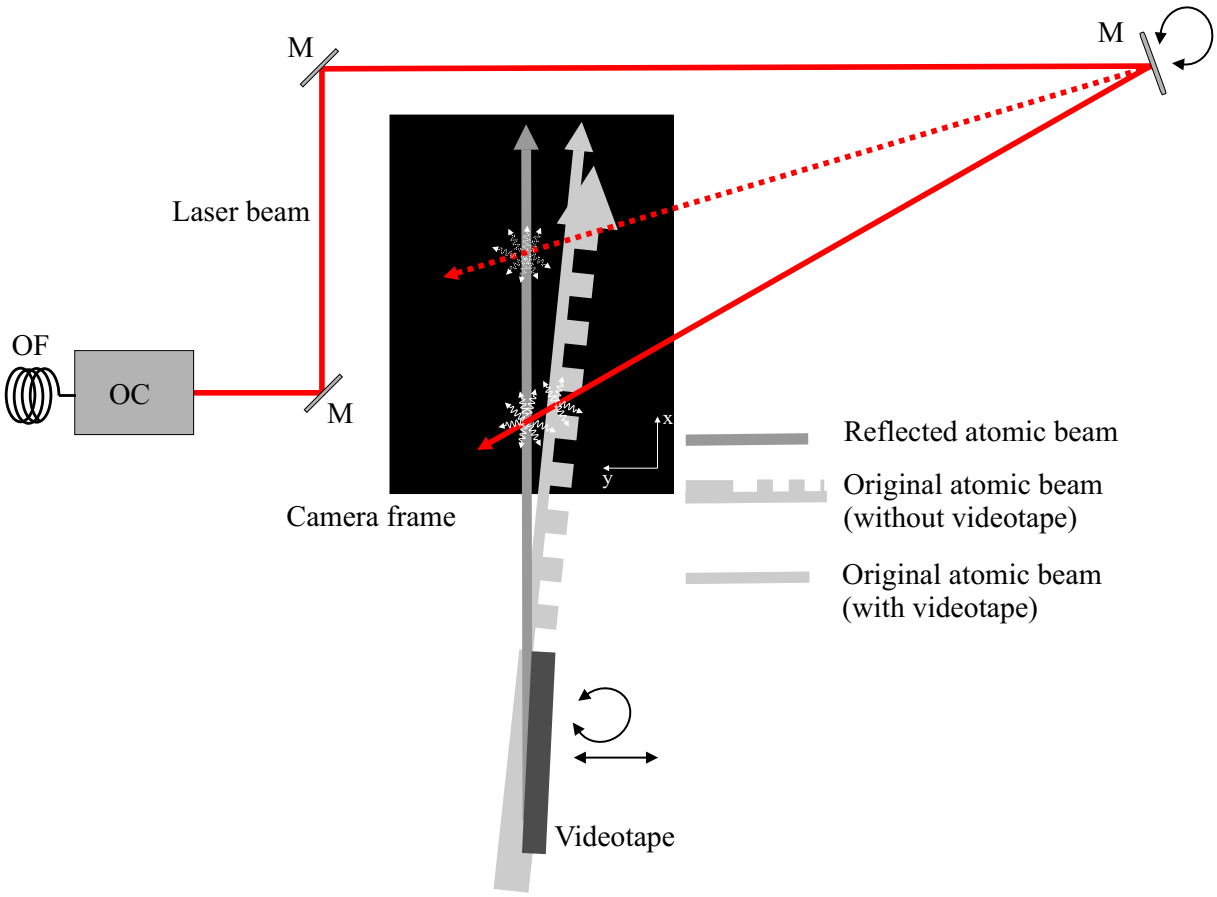

Figure 5.7: Principle of detection. We have represented the photon emission from the reflected and original atomic beams induced by the probe laser beam for two different positions of the mirror (M).

In the following, the propagation of the atomic beam corresponds to that of the Figure 5.7 which is the standard setup used for all experiments we carried out.

5.3 Results and discussions

5.3.1 Enhancement of the atomic beam density

The first attempt to concentrate the trajectories of atoms towards a common point was realized without mechanical pusher. Figure 5.8 a) is a composite of two CCD images showing the reflected and the original atomic beams. The coordinate system used in the experiments is shown in the picture. Atoms are incident at an angle of $(3.9 \pm 0.3)^\circ$ and the number of reflected atoms is small compared to the original atomic beam. First, this is due to the small angle of reflection i.e a small effective surface of the videotape onto which atoms reflect. Second, optical test of the mirror reduces the surface of reflection to 21 mm as shown in Section 5.2.2, i.e all atoms in the atomic beam are reflected for

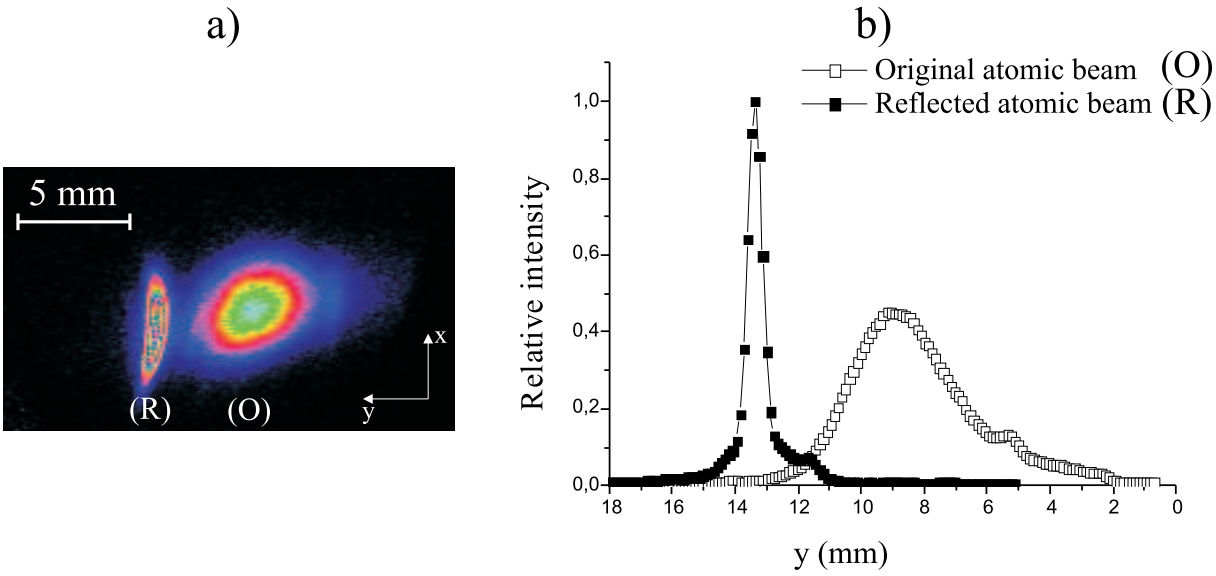

Figure 5.8: Enhancement of the atomic density in the atomic beam. a) Added images of the reflected atomic beam and original atomic beam. The label (R) is made for the reflected beam whereas (O) is for the original beam. b) Cross section along the y-axis showing the fluorescence intensity enhancement of the reflected atomic beam. The atoms are defected at $\alpha_{defl} = 7.8°$.

angles larger than $\alpha_{thres} = 13.5°$. This condition is never fulfilled because atoms incident at angles larger than $\alpha_{max} = 7.6°$ collide onto the videotape and are lost. Fortunately with only a small fraction of atoms, a compression of the initial atomic beam trajectories is realized along the propagation direction of atoms. This is illustrated in Figure 5.8 b), which shows the intensity of atoms versus their spatial position. The profiles correspond to the horizontal direction in Figure 5.8 a). The intensity is normalized to the maximum intensity of the reflected atoms. We recognize a small bump at small distances in the spatial distribution of the reflected atoms. This corresponds to a residual signal from the original atomic beam, i.e atoms that are not reflected by the videotape. The same phenomenon occurs in the distribution of atoms in the original atomic beam but due to a different reason. The reflector moved completely at one side let the atomic beam propagating freely. However, the mirror is not far enough so that a small amount of atoms located at the extremity of the atomic beam is still reflected and this results in a small enhancement of atoms at a distance of 5.3 mm. The distribution of the original atomic beam presents a slight asymmetry along the y direction originating from the radiation pressure and the angle of incidence of the probe laser beam. We see that the intensity of the reflected atomic beam increases up to a factor 2.2 with respect to the original atomic beam. This first result proves that the magnetic mirror has a natural radius of curvature and produces the expected effect. The reflector acts as a condensor lens.

We decided to reconstruct the path of atoms by moving the probe beam along the reflected atomic beam axis. From our understanding, if a focus exists, we should be able to observe

at least, a variation along the x-direction of the atomic beam diameter, which should be more important than its angular divergence. This is not easy to emphasize because the diameter of the probe beam is too large and reduces the resolution in the evolution of the atomic beam width along the propagation direction. An additional difficulty appears when atoms fly through the probe region. They undergo a strong radiation pressure which deviates them from the initial direction of reflection. Indeed, the small longitudinal velocity and hence the long interaction time in the light field contributes to the "banana" shaped atomic beam, as depicted in Figure 5.8 a). An estimation of the deviation Δd of an atom by the light field is given by

$$\Delta d \leq \frac{a_{max}}{2}(\frac{D_L}{v_\ell})^2, \tag{5.7}$$

where a_{max} is the maximum acceleration of Cs atoms, v_ℓ is the longitudinal velocity and D_L is the interaction length with the probe laser. For $a_{max} = 5.7.10^4$ m/s^2, $D_L = 5$ mm and $v_\ell = 20$ m/s, we find $\Delta d \leq 1.8$ mm.

5.3.2 Atomic beam focusing

Some modifications are realized to improve the detection system. First, we reduced the intensity of the probe beam to $I = 8I_S$ to avoid effects due to radiation pressure and then we focalized the laser beam to increase the resolution for probing the variations of the

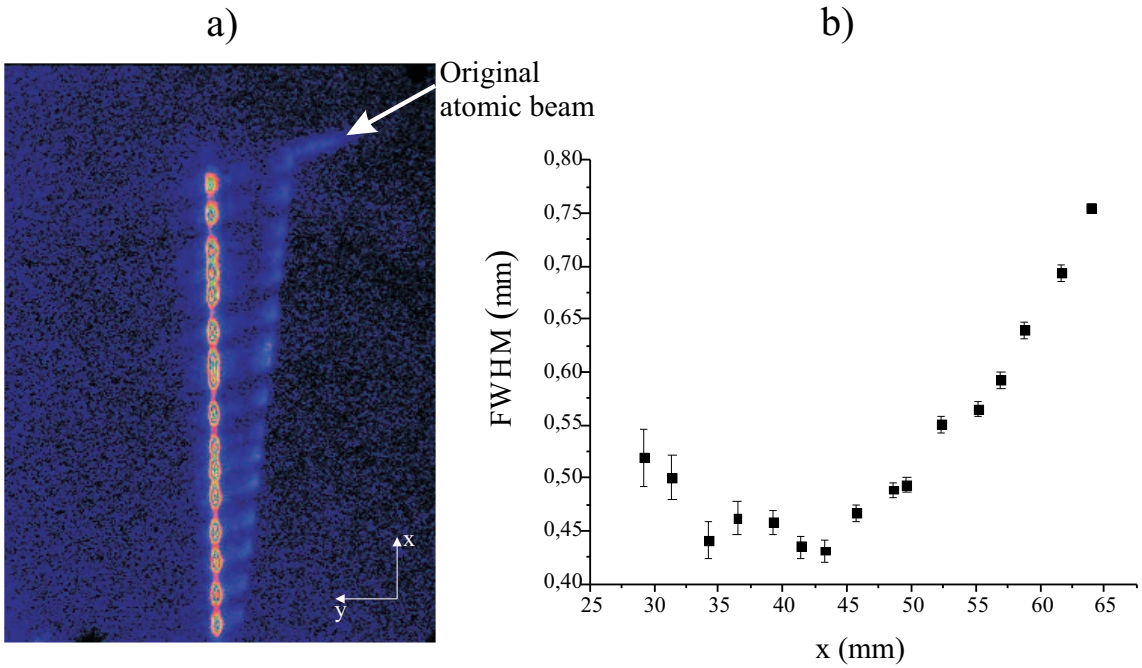

Figure 5.9: Focusing of the atomic beam. a) Added images of the reflected atomic beam and original atomic beam. b) Beam diameter of the reflected and focused atomic beam. The waist is clearly visible.

atomic beam width along the direction of propagation.

Single atomic bounce

Figure 5.9 a) is a sequence of 16 images taken with the probe laser beam at different positions and different angles along the direction of propagation, as well as an image of the original beam without the videotape. For each position, we have optimized the induced fluorescence intensity by scanning transversally and longitudinally the position of the probe laser beam with respect to the propagation direction of the atomic beam. The resulting pattern gives the path followed by the atoms. The maximum of each trace can be related by a linear fit, confirming the specular aspect of the reflected atomic beam: the videotape acts as a smooth magnetic reflector. We see clearly that not all atoms undergo a reflection on the magnetic videotape, some of them move in straight lines corresponding to a residual part of the original beam. The profiles of the straight-through beam reveal that the atomic beam has been cut by the sharp edge of the magnetic mirror. From this, we measure the deflection angle of the atomic beam which is $(6.4 \pm 1.1)°$.
In Figure 5.9 b), we have plotted the atomic beam full width at half maximum (FWHM) of the reflected atomic beam as a function of the propagation distance from the magnetic equipotential surface of the videotape. Each point in the graph has been corrected because the angle between the probe laser beam and the atomic beam presents a relative variation of 13° by scanning the probe beam along the direction of propagation of the atomic beam. The origin $x = 0$ corresponds to the impact point of atoms onto the videotape. After one bounce, the width of the atomic beam decreases along the direction of propagation up to a minimum, located 42 mm away from the point of reflection, and then increases, so

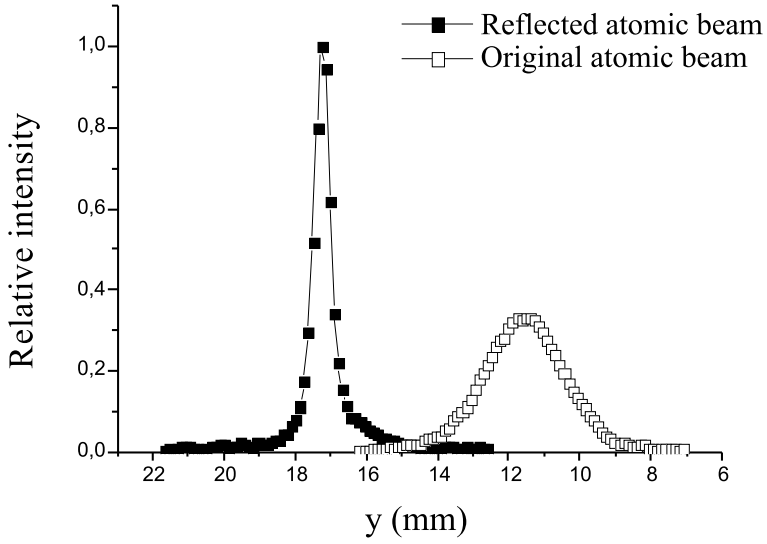

Figure 5.10: Lateral spatial compression of the trajectory of reflected atoms leading to an increase in the fluorescence intensity up to a factor 3. The atomic beam is deflected at $\alpha_{defl} = (6.4 \pm 1.1)°$.

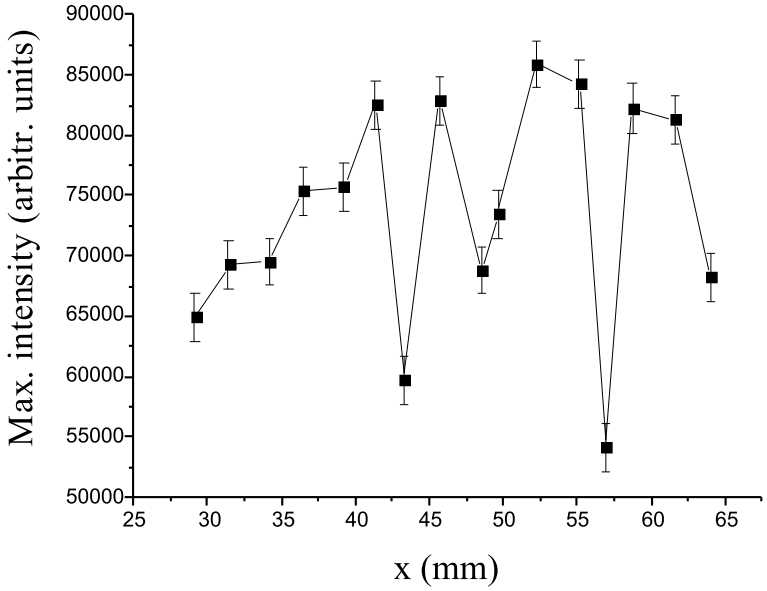

Figure 5.11: Evolution of the maximum intensity of the atomic beam along the direction of propagation.

that the atomic beam is divergent. We found the turning point of the atomic chief ray on the magnetic mirror by tracing a line following the maximum fluorescence intensity of the trajectory of the reflected atomic beam and that of the original beam. Irregularities at some points are probably due to the low ability to optimize the signal because of the small dimension of the probed region. In principle, beside a smaller width the atomic beam focusing is also accompanied by a growth in the fluorescence intensity resulting from the enhancement of the atomic beam density in the waist. Although strong variations of the deflected atomic beam maximum intensity have been measured and plotted in Figure 5.11, this did not affect the atomic beam width. All irregularities result from the instability of the $2D$-MOT, the optical collimation and the probe laser.

Thus, the graph in Figure 5.9 b) shows the typical behavior of focusing known in Gaussian optics, which is characterized by an increase in the atomic beam density in the focus region as confirmed in Figure 5.10. The profile of the reflected atomic beam corresponds to the first CCD picture at the bottom in Figure 5.9 a). The atomic trajectories are laterally confined, which increases the maximum intensity of the reflected beam up to a factor of 3.

In order to study the evolution of the atomic beam waist, we recorded new sequences of images for different angles of deflection. By slowly rotating the videotape around the previously positioned angle, we followed the variation of the focus point. Figure 5.12 a) and Figure 5.12 b) correspond respectively to a deflection angle of $(6.8 \pm 0.9)^\circ$ and $(7.8 \pm 0.9)^\circ$. The distribution of points are similar to that of Figure 5.9, however the minima of the atomic beam widths are at different positions, 28 ± 6 mm and 48 ± 7 mm resp. for Fig. 5.12 a) and Fig. 5.12 b). At first sight this is the expected behavior of the focus obtained from Equation (A.17) where for smaller angles of incidence the atomic beam waist is

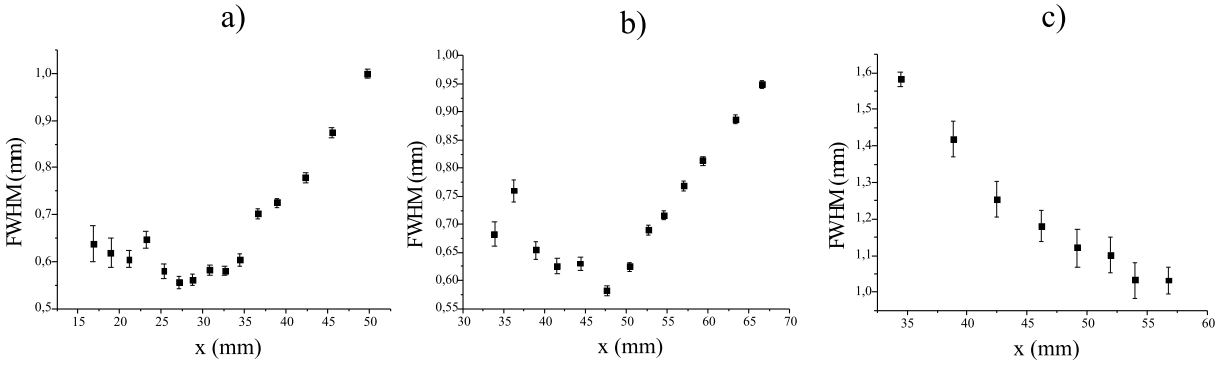

Figure 5.12: Evolution of the focusing position with different angles of deflection: a) $(6.8 \pm 0.9)°$. b) $(7.8 \pm 0.9)°$ c) $(11.1 \pm 1.3)°$.

located closer to the magnetic mirror with a spherical geometry.
Increasing further the angle of incidence up to $(11.1 \pm 1.3)°$ causes the atomic beam focus to move outside the frame of view defined by the position of the CCD camera, as represented in Figure 5.12 c). We see that the atomic beam width drops as the atoms propagate, reaching a low level at 55 ± 6 mm. A lower boundary value can be chosen for the focus point because the minimum of the atomic beam profile is not obvious to find. However interesting features can be pointed out in Figure 5.12 c). The reduction of the beam width is smaller compared with Figure 5.12 a) or Figure 5.12 b). This is precisely the behavior observed in Gaussian optics, where the Rayleigh length and the waist of a laser beam increase with the focal distance. We observed also that the fluorescence intensity is larger than that of the measured intensity for the previous angle positions. This is simply due to the larger surface of reflection that allows the capture of more atoms from the incident atomic beam.

Multiple atomic bounces

As calculated in Section 5.1.3, the formation of a focus with more than one reflection on the videotape is not excluded. Contrary to the studied whispering-gallery geometry in Chapter 3 where grazing incidence angles were dominant avoiding to find a focus point, we are able with our new source of cold atoms to focus the atomic beam for higher angles of incidence even with multiple reflections. This is carried out by mechanically pushing the videotape at one of its extremity so that the radius of curvature is small enabling a larger angle of deflection.
Figure 5.13 presents the trajectory of atoms after one and two bounces. The increasing number of atoms at the output of the reflector confirms that the curved geometry allows to catch more atoms from the initial incident atomic beam. In the far field regime, two separated atomic beams can be distinguished. Each one has a different beam width. Most of atoms are bouncing twice on the magnetic mirror and are deflected at an angle of $(8.5 \pm 0.8)°$ whereas the other part reflects once at an angle of $(7.4 \pm 0.8)°$. In the near field region however, the two beams are overlapping and do not enable us to resolve

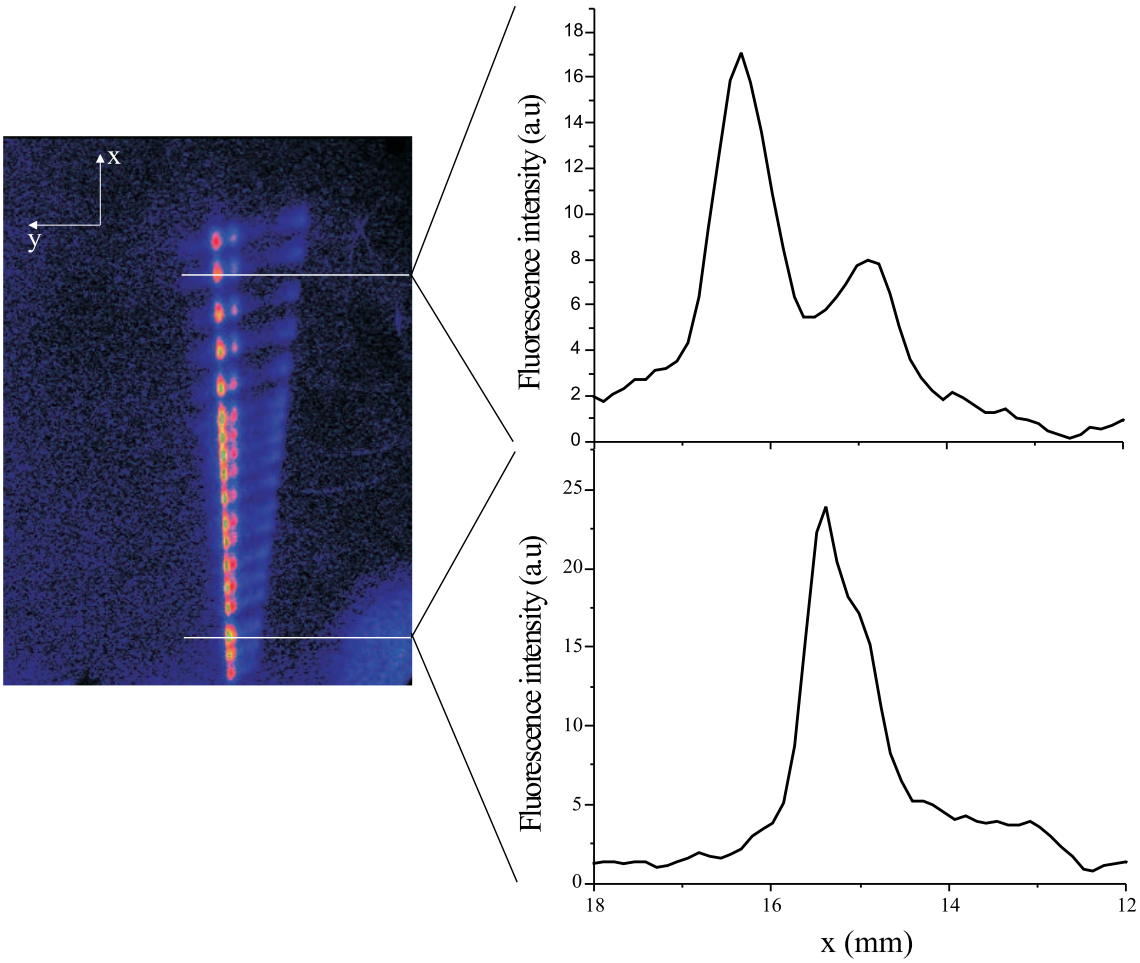

Figure 5.13: Behavior of the atomic beam width after two bounces on the magnetic videotape. Some atoms are bouncing twice whereas others bounce once. Atomic beam profiles located at 37 ± 6 mm and 67 ± 6 mm from the turning point.

them separately. Figure 5.14 shows the atomic beam width evolution versus the distance of propagation of the outer atomic beam in Figure 5.13. The graph indicates a strong irregularity in the evolution which appears 43 mm away from the turning point on the videotape. This is the frontier between the two mentioned regimes, from where the two atomic beams are resolved at large distances. In both case, we see that the width expands along the direction of propagation. The atomic trajectory intersection of the double atomic beam structure extends into the zone sustained by the center of curvature and the surface of the magnetic mirror. Due to the spatial limitation of our detection setup, we were prevented to further reconstitute the route of atoms towards the turning point onto the videotape. Thus, similarly to the large deflection angles, we can only evaluate an upper boundary value for the atomic beam waist located at 31.8 mm.
By pressing further the phosphor bronze sheet above $\alpha_{defl} = (10.8 \pm 1.6)°$, the angle

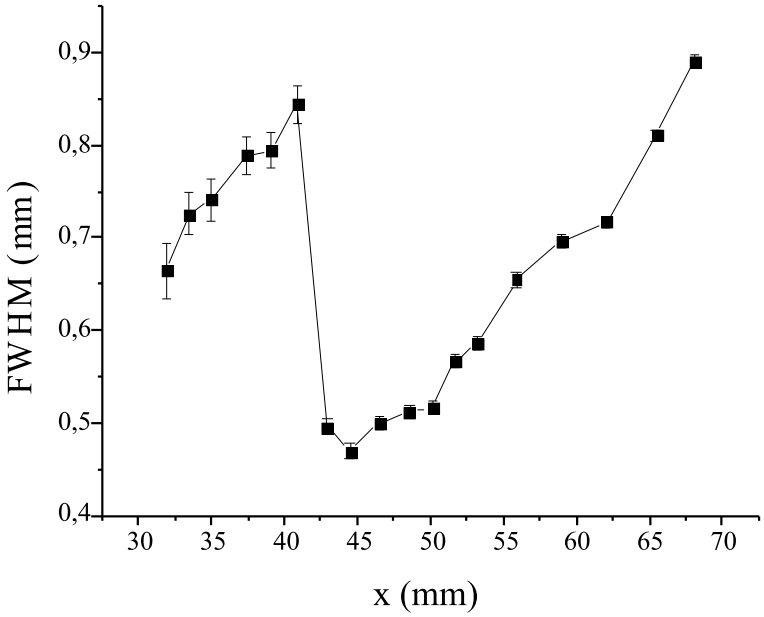

Figure 5.14: Width evolution of the outer atomic beam (2 bounces) of Fig. 5.13. The irregularity about 43 mm results from the possibility to resolve each beam individually.

of deflection increased but at the same time the atomic flux dropped drastically so that reasonable measurements could not be made.

5.3.3 Properties of the reflector

As a check of our understanding, we performed a wide range of measurements conducting to different angles of deflection. For a given angular position of the videotape, its relative transverse position to the atomic beam was chosen in order to maximize the fluorescence intensity of the deflected atomic beam. The chief atomic ray is defined as the atomic trajectory which propagates through the maximum of the atomic beam profiles. As explained in Section 5.2.4, from the recorded images we map out in the $x - y$ plane the coordinates of the atom's turning point on the reflector for each angle of deflection, as illustrated in Figure 5.15. The x-position gives the relative position of the chief atomic ray along the videotape, whereas y is the relative transverse position of the mirror holder. We recall that the origin (0,0) is taken on the camera frame. The numbers 1 to 9 increasing with the atom's angle of deflection is set for a given reflection of the atomic beam. For each point (x, y), we have sketched the chief ray trajectory of the deflected and original atomic beam. In principle the original atomic beam propagates along a fixed direction. However, we see in Figure 5.15 that its position varies depending on the point of impact onto the videotape. Indeed not all atoms are reflected and the diameter of the deflected beam is reduced to a fraction of the incident atomic beam. This implies a different atomic chief ray for each reflection. The numbers 8 and 9 are the extreme points defining the extension of the diameter of the atomic beam. We find 4.5 mm which is in good agreement with

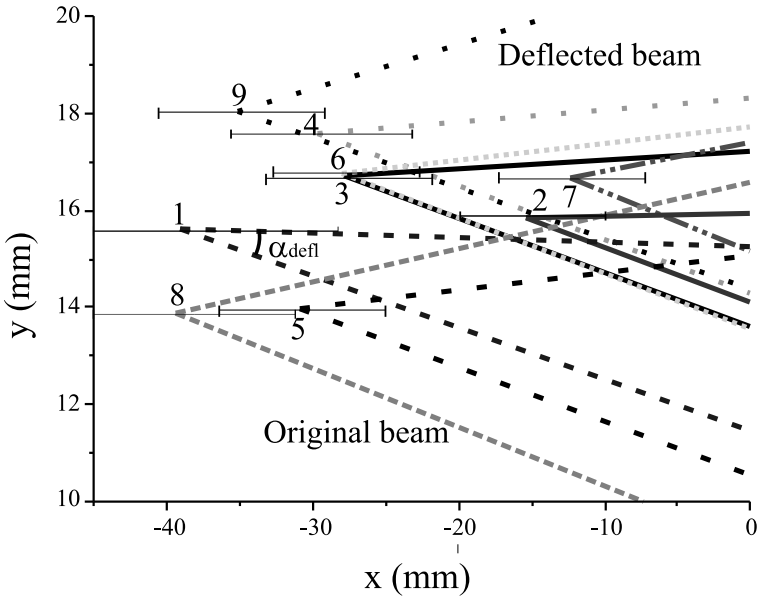

Figure 5.15: Turning points of the atomic beam in the $x - y$ plane for different angles of deflection α_{defl}. The increasing curves correspond to the reflected atomic beam while the decreasing correspond to the original atomic beam.

the measured diameter of the atomic beam in Chapter 4 where $\varnothing = 4.9$ mm. With the turning points on the videotape plotted in Figure 5.15 we can follow the positions and orientations of the magnetic reflector during the experiment. All reflections are accomplished in a region covering less than 30 mm from the total length of the videotape.
As discussed in Section 5.1.2, the angle of reflection depends on the position of atoms arriving onto the videotape. This means that for a given orientation of the reflector, the atomic beam incident in regions located at the end of the reflector undergoes a larger deflection. Pushing the mirror at one extremity will also increase the reflection angle of the atomic beam because the local radius of curvature decreases. Additionally with multiple bounces, large deflection angles are easily reached. For example in Figure 5.15 the points 1, 5 and 8 respectively deflected at $(5.5 \pm 1.2)°$, $(8.4 \pm 0.8)°$ and $(10.8 \pm 1.6)°$ originate from the same angular position of the mirror holder but for a different curvature. In these cases, the atoms reflect at different positions along the videotape which is adjusted by moving transversally the reflector. For 5 and 8 the atomic chief rays of the second bounce have been plotted. Points 3 and 6 correspond to atoms being reflected on the tape at the same point of impact however with different angles of incidence. From this distribution of points we determine the focal distance for each trajectory and deduce the radius of curvature for each atomic chief ray.

Radius of curvature

In Table 5.1, we have reported the number of the measurement N, the angle of deflection α_{defl}, the focus distance f_{loc} and the local radius of curvature R_{loc} calculated with

Equation (5.4).

Measurement N	α_{defl} (°)	f_{loc} (mm)	R_{loc} (cm)
1	5.5 ± 1.2	40 ± 12	164.9 ± 45.8
2	6.8 ± 0.9	28 ± 6	94.9 ± 21.3
3	7.4 ± 0.8	42 ± 6	130.9 ± 21.7
4	7.8 ± 0.9	48 ± 7	129.4 ± 23.1
5	8.4 ± 0.8	35 ± 6	95.5 ± 15.4
6	8.5 ± 0.8	48 ± 5	141.5 ± 18.9
7	10.4 ± 1.1	37 ± 5	81.8 ± 14.4
8	10.8 ± 1.6	43 ± 8	91.6 ± 19.0
9	11.1 ± 1.3	55 ± 6	113.5 ± 18.8

Table 5.1: Measurement of the atomic beam at different angles of incidence. R_{loc} is deduced from the experimental parameters α_{defl} and f_{loc}.

The curvature of the magnetic reflector is simply determined by representing the local radius of curvature as a function of the position x of the turning points of atoms, as depicted in Figure 5.16. We see that the radius of curvature decreases along the position onto the videotape. This is consistent with the extremity of the reflector at large distances

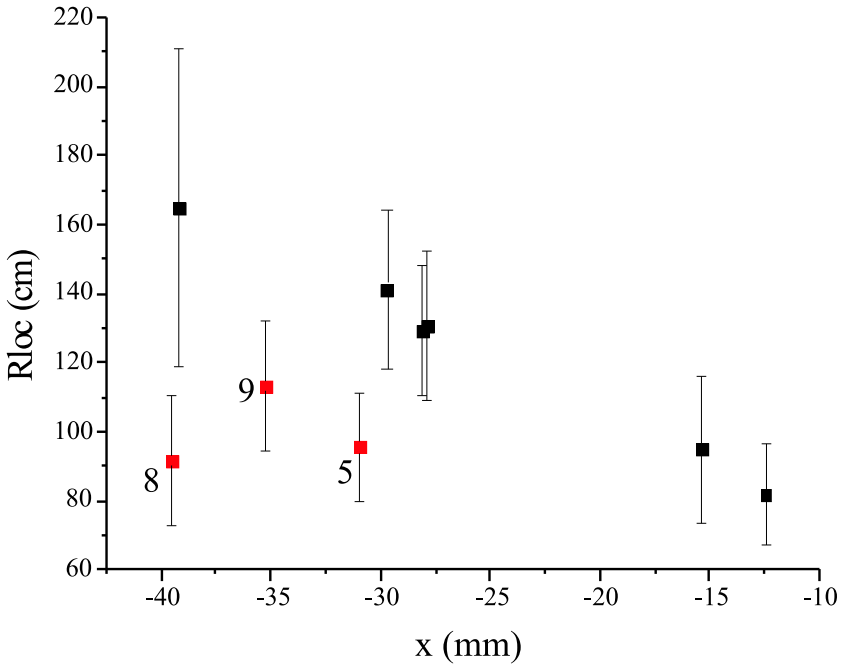

Figure 5.16: Radius of curvature of the videotape deduced from the focal distance of the curved reflector.

which is subjected to the pressure of the mechanical pusher. Due to the elasticity property of the phosphore bronze sheet, the videotape presents a natural curvature after using the mechanical pusher several times. The measurement 9 corresponds to the estimated focus distance for large deflection angles extending outside the field of the camera frame, whereas for smaller curvature the points 5 and 8 are found with an upper boundary estimation leading to minimum radii of curvature. In reality the radius of curvature is well below the value represented in Figure 5.16.

Red laser examination

The previous results are confirmed by the investigations carried out by reflecting the red laser beam onto the videotape. The mechanical pusher acting onto the videotape does not allow to determine directly the radius of curvature of the videotape. However, one way to overcome this problem is to measure during the experiments with the atomic beam the relative positions of the screw moving the mechanical pusher with a micrometer precise ruler. The zero position of the screw is defined when the pusher is just in contact with the flexible magnetic mirror without pushing it. Later, after building down the magnetic mirror holder from the experimental chamber, we reproduce on the optical table the same condition as in the experiment with the pusher acting on the reflector. A red laser beam is expanded with a telescope up to a diameter of 5 mm and illuminates at normal incidence a large area of the magnetic videotape which is quite reflective in the visible. We have first investigated the optical quality of the surface with the setup presented in Figure 5.17. Specular reflections are limited in a given area which is 21 mm-long while the mechanical length of the videotape is 53 mm. Outside this region, the reflections are strongly diffuse. This is probably due to some deformations which appeared at the extremity of the tape after using several times the mechanical pusher.
Depending on the pressure applied in the extremity of the mirror as shown in Figure 5.17,

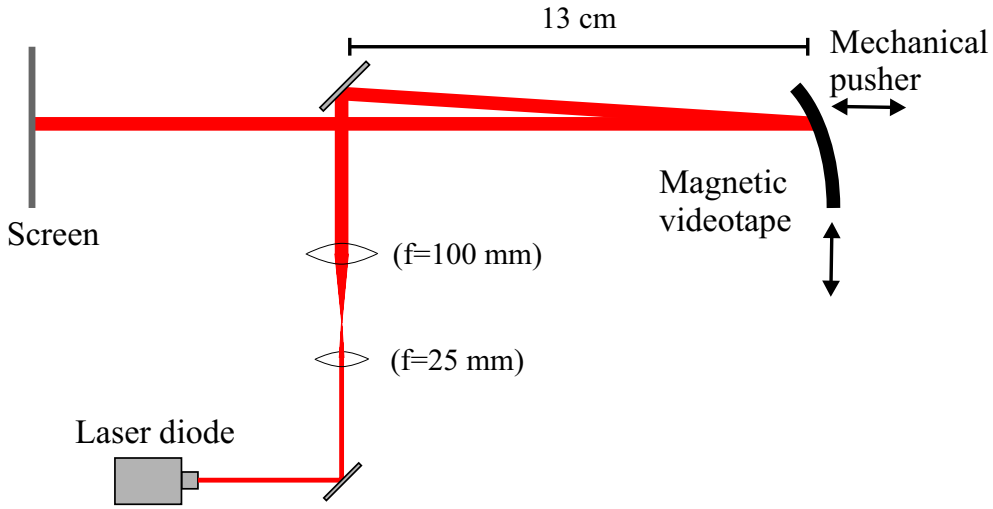

Figure 5.17: Investigation of the radius of curvature of the videotape.

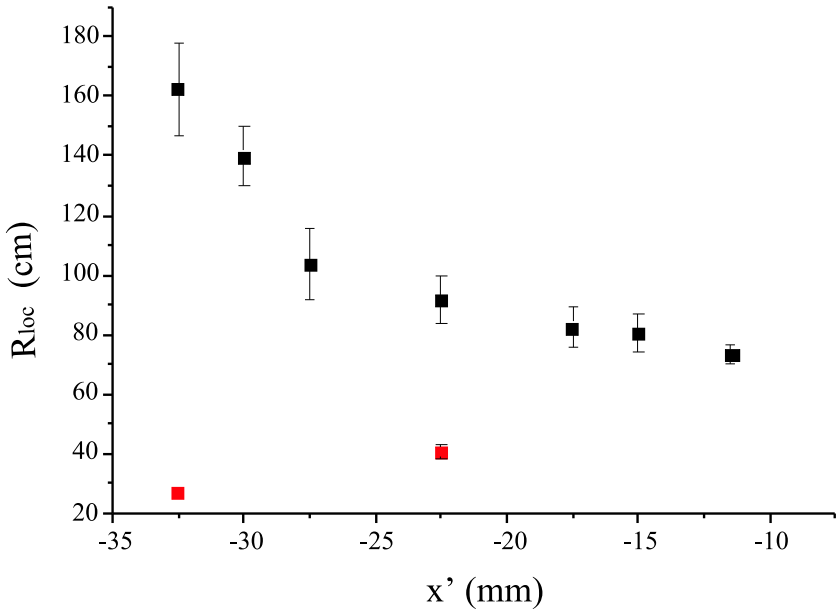

Figure 5.18: Determination of the radius of curvature R_{loc} of the videotape by shining at normal incidence a red laser diode onto its surface. The points at 27.4 cm and 40.5 cm correspond to reflections with the mechanical pusher for the points 5 and 8 of Figure 5.16.

the focus position f_r of the laser beam travel towards the surface of the reflector with smaller radius of curvature R. We tilt the incident red laser beam ($\alpha \sim 90°$) so that the minimum (waist) of the beam can be distinguished. The Rayleigh length of the red laser increases when R increases, which implies a larger uncertainty on the determination of the focus localization. With $f_r \sim R/2$, it is easy to deduce the curvature of the videotape.

The resulting radius of curvature versus the position onto the videotape is presented in Figure 5.18. Here, the origin is taken at one of the extremities of the reflector where the curvature is smaller. The reported data are in good agreement with those of Figure 5.16. The radius of curvature in both cases varies in the same domain where the upper limit is around 160 cm and the lower about 80 cm. As expected, with the mechanical pusher and the red laser beam at normal incidence, the focus is closer to the surface of the videotape so that the radius of curvature reaches low values. In this case, we have chosen to illuminate the surface in such a way that the distance between the points 5 and 8 is approximately 10 mm as found in Figure 5.16 and we expect that the two lowest values of the radius of curvature in Figure 5.18 correspond to the experimental conditions for the point 5 and 8 in Figure 5.16 realized with the atomic beam. We see that there is no substantial difference in the effective surface of reflection found with the two methods; 28 mm with the atomic beam and 21 mm by using the red laser diode. The single difference lies in the alignment of the atomic beam and the videotape which is not precisely known. This prevents an absolute comparison between the data obtained with the atomic beam and the red laser beam because the chosen origins along x and x' are different.

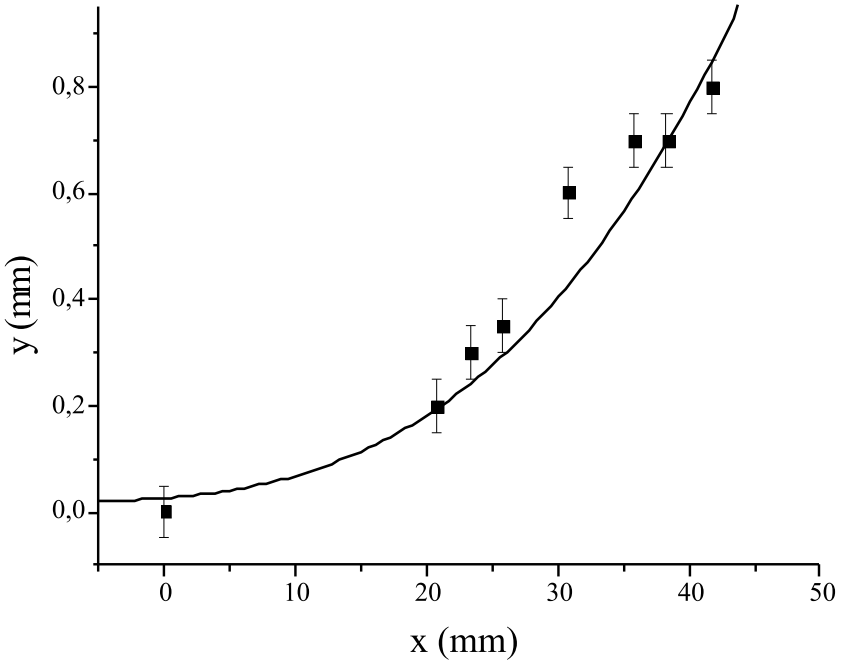

Figure 5.19: Shape of the videotape fitted with the function of Equation (5.8).

Shape of the reflector

The variation of the radius of curvature along the videotape shows that the shape of the reflector is not spherical. The measurement of the mechanical shape of the reflector is reported in Figure 5.19. The data are plotted in the $x - y$ plane. The origin (0,0) corresponds to the first extremity of the videotape. The distribution of points is fitted with the function

$$y = 6 \cdot 10^{-6}(x + 10)^3. \tag{5.8}$$

First the radius of curvature is large and then decreases as the function increases according to the results of Figure 5.16 and Figure 5.18.
To confirm the results of the foci obtained experimentally with the videotape, we performed simulations with the function of Equation (5.8) as a reflector. We neglect the small offset contribution in Equation (5.8) because this is equivalent to a small translation of the magnetic reflector in the y direction and can be easily compensated by changing the impact parameter of the atoms. Figure 5.20 shows the calculation of the atom trajectory leading to a focus after one bounce onto the reflector. Atoms are incident at an angle of 4° and deflected at $\alpha_{defl} = 12°$. The atomic beam is imaged at a distance $f = 33$ mm away from the point of reflection. For the divergence of the atomic beam we have taken into account a Gaussian distribution of the transverse velocity with a width of $\Delta v_t = 2$ cm/s. We have chosen a beam diameter of 2 mm for $x = 0$ because the investigation of the optical surface in Section 5.2.2 indicates that specular reflectivity is achieved in a region smaller than the full mechanical length of the videotape. This means that in our experiments only

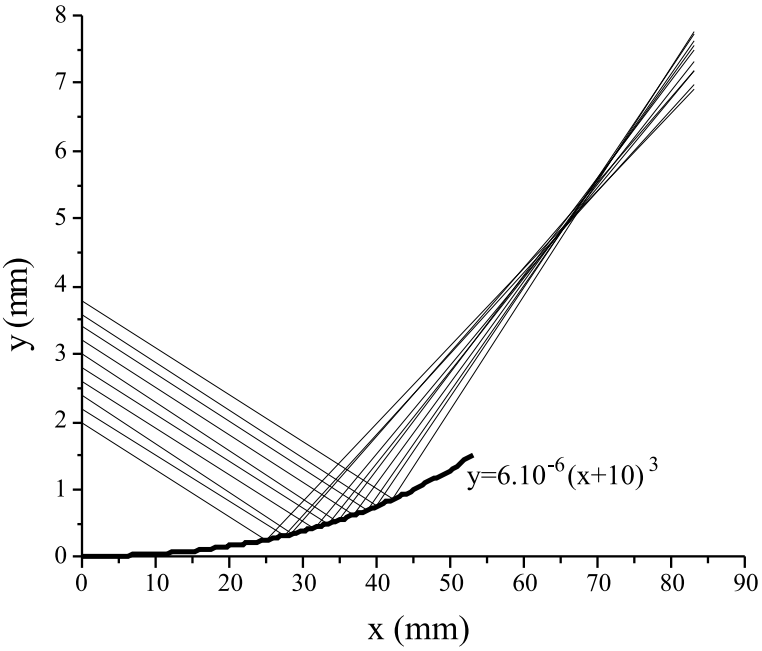

Figure 5.20: Atomic beam simulation of the focus realized after reflecting on the reflector given by Eqt. (5.8). The atoms are deflected at $\alpha_{defl} = 12°$ and focus at $f = 33$ mm.

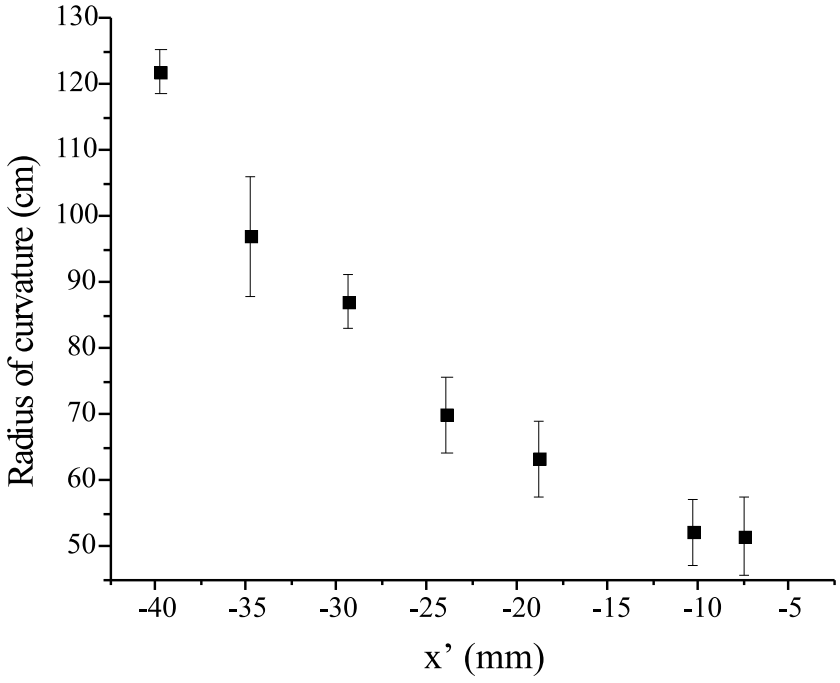

Figure 5.21: Calculation of the radius of curvature of the function of Equation 5.8.

a small fraction of the 5 mm atomic beam cross-section is reflected.
With our assumptions we calculate the trajectories of the atomic beam for different point of impact onto the curved reflector and deduce the deflection angle as well as the focal distance of the atomic chief ray trajectory. This allows us to determinate the local radius of curvature of the reflector as reported in Figure 5.21. The radius of curvature R_{loc} is plotted as a function of the atom's turning point onto the reflector. The origin $x' = 0$ corresponds to the end extremity of the videotape as already pointed out in Figure 5.18. The data points are located between $R_{loc} = 122$ cm and $R_{loc} = 50$ cm. This distribution is in good agreement with the fit of Equation (5.8): R_{loc} decreases along x' while the function in Figure 5.19 increases with a larger curvature. The comparison with R_{loc} found from the experiments shows that the radius of curvature deduced from the simulations is very close to those obtained with the atomic beam and the red laser beam. The shape of the reflector is well described with Equation (5.8) with a good approximation. The small discrepancy between experiment and theory arises from the ability of measuring the shape of the reflector. Indeed, the sub-millimeter variation of the shape along the x-axis shown in Figure 5.19 requires a more accurate method for the measurement.

5.3.4 Spherical aberration: the caustic

The calculations in Section 5.1 predict that the focus of an atomic beam produces always aberrations, except for the paraxial approximation. The spherical aberration described by a caustic represents the spatial region where the atomic trajectories are strongly concentrated. We already mentioned that the caustic length is important for small angles of incidence of the atomic beam.
To investigate experimentally the caustic, we chose to follow the behavior of the reflected atomic beam width along its direction of propagation. For this purpose, we decided to expand the diameter of the probe laser beam up to 5 mm. In this way, atoms spend enough time in the light field so that small contributions to the aberration can easily be resolved. For different points along the direction of propagation, the transverse profiles of the atomic beam are reported in Figure 5.22. The intensity of atoms is normalized to the point which induces the higher fluorescence intensity. Thus, this relative intensity is plotted as a function of the x and y axis as defined is Section 5.2.4. The letters along the x axis represent the position of the laser beam with respect to the turning point of atoms in the magnetic field created by the videotape.
The profile of the reflected atoms show a maximum of intensity and a minimum of the width located 25.8 mm away from the magnetic reflector. We take this position as the focus f of our curved videotape. The strong asymmetry of the profiles reveals the property of the caustic as discussed in Section 5.1.2. In the near field regime, the trajectory followed by atoms depend on their point of impact onto the reflector. Below f, the slowly decreasing part of the distribution along y corresponds to atoms which are reflected at large angles i.e atoms reflecting at small curvatures while small deflection angles of atoms contribute to the asymmetrical behavior of the profiles for distances above f. In the frame system of the reflected atomic beam, a small amount of atoms drift from the atomic ensemble. This is the residual part of the original atomic beam, i.e atoms which are not

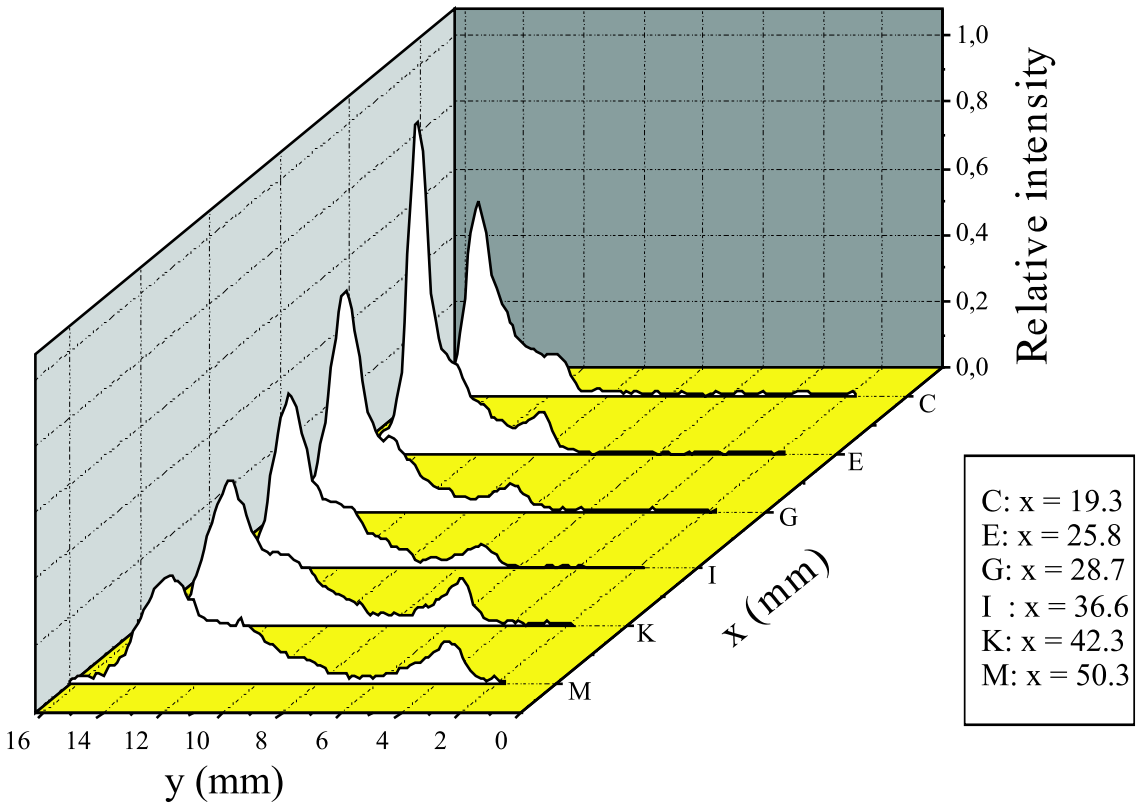

Figure 5.22: Aberration imaging of a spherical reflector. The inset shows the caustic formation for small angle of incidence.

reflected. We notice in this case that the number of atoms is roughly constant along the direction of propagation. From the graph, we deduce the angle of reflection of the atomic ray chief which is $\alpha_{defl} = 7.8°$. With Equation (5.3), the calculated radius of curvature is $R = 75.9$ cm.

The investigation of the reflectivity of the magnetic videotape with a red laser diode discussed in the previous section shows an effective surface of reflection limited to a length of 21 mm. It follows that the atoms arriving at the outer parts of the 53 mm-long reflector are lost and this reduces the contribution to the spherical aberration. By this way, we approach the condition of Equation (5.2) which lead to a smaller extension of the caustic.

Chapter 6

Conclusion and outlook

We have shown through this thesis that videotapes can be used as a high-quality atomic beam reflector for reflective atom optics. We have developed a new technique for mounting the videotape so that the shape can be reliably made flexible and the reflecting surface can conform closely to the desired geometry. In order to perform the experiments, we have prepared two types of atomic beams.
With the first, the Zeeman-slowed atomic beam, atoms at grazing incidence and traveling at 60 m/s were reflected onto the videotape. We have used the atom beam itself to calibrate the strength of the magnetic field at the surface of the tape. In analogy with the x-ray optics in which optical components at grazing-incidence are well-known, we have demonstrated that a curved videotape can deflect atoms at angles as large as 23° in a whispering-gallery configuration. We have shown that with an adequate angle of incidence the number of reflections realized by the atomic beam can be counted.
The second beam arises from a cold atomic source, the $2D$-MOT. The atoms are extracted with a pusher laser beam which is separated from the atomic beam by slowly tilting the optical collimating stage or the pusher beam itself. With this setup, we were able to obtain a well-collimated and optically pumped slowed atomic beam propagating at 20 m/s. This enables with one bounce to reflect atoms onto the videotape at angles of incidence up to 7°. Thus, we have demonstrated the focusing of the atomic beam with the natural curvature of the videotape at different angles of deflection. We have shown that focusing is not limited to atoms which bounce once but can also be realized with multiple bounces. The focal length depends on the point of impact of atoms onto the curved reflector. We have deduced the radii of curvature of the videotape from the angles of deflection and the corresponding focal lengths. The values found were in good agreement with the measurements of the radii of curvature determined with a red laser beam at normal incidence onto the reflector. We have confirmed the experimental results by first measuring approximatively the shape of the videotape and found that the function $\sim x^3$ describes it well. We have performed simulations with the atomic beam incident at different parameters of impact and have calculated the radii of curvature at these points along the videotape. Finally, we have shown that spherical aberrations, i.e the caustic, concentrate the atomic trajectories along a well-defined curved. We have emphasized

that a more localized focal point can be reached either with small angles of curvature β of the videotape or with large incidence angles α and small atomic beam diameters.
Thus, the reduction of the caustic length requires eventually a compression of the atomic beam by moving the optical collimation system closer to the mechanical hole in the aluminum mirror in the glass cell or with a compression stage which is composed of magnetic and light forces [84]. Larger angles of incidence can be enhanced by further reducing the longitudinal velocity of the atomic beam. This can be realized by adding a laser beam which counterpropagates the pusher beam with a different detuning. Also by increasing the thickness of the videotape, we can improve the surface field strength and hence the maximal transverse velocity allowing the reflection of atoms by the magnetic mirror.

These results pave the way for new experiments with the videotape as a tool for atom optics. Although magnetic mirrors based on permanent magnetization are passive and do not allow temporal variations of the magnetic potential, it has been shown in a recent PhD-thesis [74] that the reflective magnetic surface of the videotape can be adapted by the addition of a suitable external field. For example, the principle of the atomic grating [85, 86] can be applied for the diffraction of atomic beams. We expect in that way to produce monochromatic atomic beams.
The videotape can also be used as a deflector for atoms between two experimental chambers and do not require heavy materials for guiding atoms as in [87]. The extension of the whispering-gallery geometry to a storage ring for neutral atoms opens new prospects in ring-based atomic interferometry [88, 89]. This configuration provides also new possibilities to create ultra-cold atomic beams. For example, atoms can be continuously loaded in the ring, and both the longitudinal and transversal velocity distributions of atoms can be cooled in the ring.
A straightforward application of the atomic beam imaging shown in this work is the atomic lithography. Generating structures in the sub-micrometer domain has increased the interest in exploring various methods for the production of any patterns [34]. In our lab, it has been shown recently that a thermal atomic beam focused by means of a refractive magnetic lens enables to write micrometer-sized samples. With a cantilever used as a shadow mask, sub-micrometer dimensions are expected to be reached. By replacing the refractive lens with a reflective element like the videotape, we take advantage of the possibility to eliminate the chromatic aberrations. Even if other aberrations appear, we can easily correct them due to the high flexibility of the videotape allowing to shape the reflector in any geometry [19]. With these assumptions reflective atomic nanofabrication could be a serious candidate to compete with refractive atomic lithography.

Appendix A

Geometrical atom optics

Most of the well-established notions in the geometrical optics may be transfered to the case where the light ray is replaced by the atomic ray. As long as the effect of the gravitational force on the motion of the atom is neglected, as it is the case in our experiments, the trajectory of the atom is simply a straight line.
With pure geometrical considerations, we consider the reflection of an atomic beam on the surface of a magnetic spherical reflector at different angle of incidence. Thus, we propose to derive the formula which lead to the relation of conjugation for a reflected atomic beam.

A.1 Paraxial approximation

Figure A.1 illustrates the reflection of an atom by a concave mirror. The vertical x-axis and the horizontal y-axis defines the plane, where atoms are free to move. The origin (0,0) is the node of the mirror. The atom with velocity v_ℓ cross the symmetry axis y at some point y_1 from the origin. The atom strikes the reflector at the point (x_0, y_0). The angle of incidence α with respect to the horizontal is

$$\tan\alpha = \frac{x_0}{y - y_0}. \tag{A.1}$$

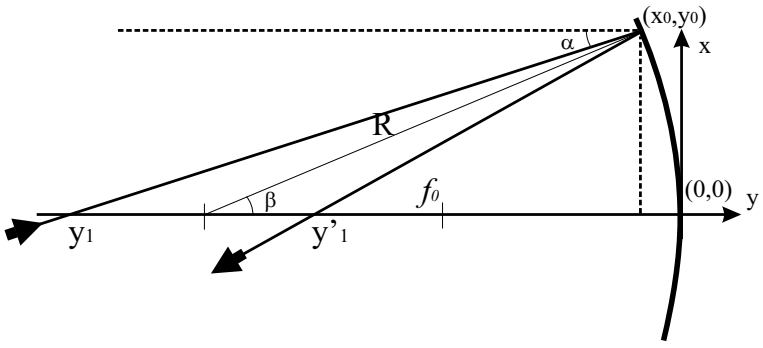

Figure A.1: Image formation by a concave mirror of point y_1 on the y-axis.

The normal at this point makes an angle β to the y-axis as

$$\sin\beta = \frac{x_0}{R}, \tag{A.2}$$

where R is the radius of the mirror. The atom is reflected at an angle $(2\beta - \alpha)$ with respect to the horizontal and reaches after one bounce the y-axis at a point y_1'.
In the paraxial regime, we approximate $x_0 \ll R$ and $x_0 \ll y_1, y_1'$, which imply α and β as small angles. It is now easy to show that

$$\alpha + 2\beta\alpha = \frac{x_0}{y_1} + \frac{x_0}{y_1'} = \frac{2x_0}{R}. \tag{A.3}$$

We recognize the formula giving the conjugate relation for a mirror,

$$\frac{1}{y} + \frac{1}{y'} = \frac{2}{R}. \tag{A.4}$$

For $\alpha = 0$, $y \to \infty$ so that the primary focal point is defined as the point image for which the object is incident at infinity, so we have

$$f_0 = \frac{R}{2}. \tag{A.5}$$

This expression is valid as long as the magnetic barrier is high enough so that atoms with velocity $v_t < v_{tmax}$ are still reflected. We note, however for x_0 far from the symmetry axis that the focal point varies along y as

$$f = R[1 - \frac{R}{2\sqrt{R^2 - x_0^2}}]. \tag{A.6}$$

A.2 Off-axis angles of incidence

At near-normal incidence a concave spherical mirror can be used to form a good image of a point object on the symmetrical axis. This is no longer the case as the object is moved away from the symmetry axis and aberrations are important for large incidence angles relatively to the normal-axis.
Let's consider Figure A.2, in which an atomic beam at small angle of divergence θ is reflected on the mirror from a point source S. The image I of S is located at a distance v from the origin O, whereas $SO = u$. The beam spread on a distance $NO = k$ on the surface of the reflector and θ is small enough so that $k \ll R$. The angle of incidence α is defined with respect to NO. The center of curvature C is related to the chord NO with $k = 2R\sin(\beta/2)$ and γ is the angle at I.
In the triangle SON, we see that

$$2R\sin\frac{\beta}{2}\sin\alpha = SN\sin\theta \tag{A.7}$$

and

$$u - 2R\sin\frac{\beta}{2}\cos\alpha = SN\cos\theta. \tag{A.8}$$

The ratio of the equality (A.7) and (A.8) gives

$$\tan\theta = \frac{2R\sin\frac{\beta}{2}\sin\alpha}{u - 2R\sin\frac{\beta}{2}\cos\alpha}. \tag{A.9}$$

Using small angle approximations $\gamma, \theta \ll 1$, the triangle SON gives

$$\theta = \frac{2R\sin\frac{\beta}{2}\sin\alpha}{u - 2R\sin\frac{\beta}{2}}, \tag{A.10}$$

In ION we make the same procedure and it follows

$$2R\sin\frac{\beta}{2}\sin(\alpha+\beta) = IN\sin\gamma \tag{A.11}$$

and

$$v + 2R\sin\frac{\beta}{2}\cos(\alpha+\beta) = IN\cos\gamma. \tag{A.12}$$

The corresponding ratio is

$$\tan\gamma = \frac{2R\sin\frac{\beta}{2}\sin\alpha\cos\beta(1+\frac{\tan\beta}{\tan\alpha})}{v + 2R\sin\frac{\beta}{2}\cos(\alpha+\beta)} \tag{A.13}$$

where $\sin(\alpha+\beta) = \cos\beta(1+\tan\beta/\tan\alpha)$.
and by the same way as for Equation (A.10), we find

$$\gamma = \frac{2R\sin\frac{\beta}{2}\sin(\alpha+\beta)}{v + 2R\sin\frac{\beta}{2}\cos(\alpha+\beta)}. \tag{A.14}$$

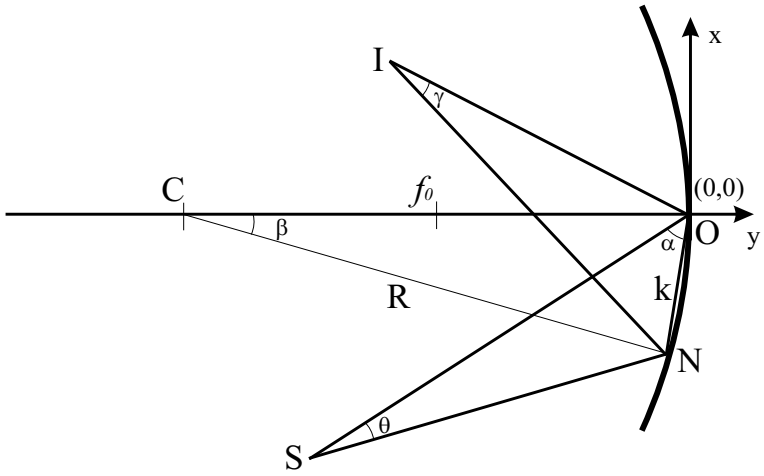

Figure A.2: Off-axis image formation by a circular mirror.

From the law of reflection, where $\gamma + \theta = 2\beta$ [90], we obtain with equations (A.10) and (A.14)

$$\frac{1}{u - 2R\sin\frac{\beta}{2}\cos\alpha} + \frac{\cos\beta(1 + \frac{\tan\beta}{\tan\alpha})}{v + 2R\sin\frac{\beta}{2}\cos(\alpha+\beta)} = \frac{2\beta}{2R\sin\frac{\beta}{2}\sin\alpha}, \tag{A.15}$$

which for small β reduces to the image-mirror equation

$$\frac{1}{u} + \frac{1}{v} = \frac{2}{R\sin\alpha}. \tag{A.16}$$

With $u \to \infty$, the focal point f is

$$f = f_m = \frac{R}{2}\sin\alpha. \tag{A.17}$$

For $\alpha = \pi/2$, we find the particular condition of equation (A.5). For a wide variety of angles α, the image points form a parabola. In the three dimensional case, f_m is known as the meridian focal length and the phenomenon of astigmatism occurs. Instead of a point image, two mutually perpendicular line images are formed. Thus, the second focal length is the sagittal focal length f_s .

Bibliography

[1] W. Gerlach and O. Stern, *Der experimentelle Nachweis des magnetischen Moments des Silberatoms*, Z. Phys. (8), 110–111 (1921)

[2] O. Frisch, *Experimenteller Nachweis des Einsteinschen Strahlungsrckstoßes*, Z. Physik (86), 42 (1933)

[3] H. Friedburg and W. Paul, *Optische Abbildung mit neutralen Atomen*, Naturwissenschaften (38), 159–160 (1951)

[4] H. Metcalf and P. van der Straten, *Laser Cooling and Trapping*, Springer (1999)

[5] F. Shimizu, *Specular reflection of very slow metastable neon atoms from a solid surface*, Phys. Rev. Lett. **86**(5), 987–990 (2001)

[6] O. Carnal, M. Sigel, T. Sleator, H. Takuma and J. Mlynek, *Imaging and focusing of atoms by a fresnel zone plate*, Phys. Rev. Lett. **67**(23), 3231–3234 (1991)

[7] M. Boustimi, J. B. M. Ducloy, J. Reinhardt, F. Perales, C. Mainos, V. Bocvarski and J. Robert, *Mestastable rare gas atoms scattered by nano- and micro-slit transmission gratings*, Eur. Phys. J. D (17), 141–144 (2001)

[8] V. Balykin, V. Letokhov, Y. Ovchinnikov and A. Sidorov, *Quantum state selective mirror reflection of atoms by laser light*, Phys. Rev. Lett. **60**(21), 2137–2140 (1988)

[9] J. Bjorkholm, R. Freeman, A. Ashkin and D. Pearson, *Observation of focusing of neutral atoms by the dipole forces of resonance-radiation pressure*, Phys. Rev. Lett. **41**(20), 1361–1364 (1978)

[10] J. Dowling and J. Gea-Banacloche, *Evanescent light-wave atom mirrors, resonators, waveguides, and traps*, Adv.At.Mol.Opt.Phys. (37), 1–94 (1996)

[11] P. Desbiolles, M. Arndt, P. Szriftgiser and J. Dalibard, *Dissipative atom optics*, J. Mod. Opt. (44), 1827 (1997)

[12] W. Kaenders, F. Lison, A. Richter, R. Wynands and D. Meschede, *Imaging with an atomic-beam*, Nature (375), 214–216 (1995)

[13] W. Kaenders, F. Lison, I. Müller, A. Richter, R. Wynands and D. Meschede, *Refractive components for magnetic atom optics*, Phys. Rev. A **54**(6), 5067–75 (1996)

[14] T. Roach, H. Abele, M. Boshier, H. Grossman, K. Zetie and E. Hinds, *Realization of a Magnetic Mirror for Cold Atoms*, Phys. Rev. Lett. **75**(4), 629–632 (1995)

[15] I. Hughes, P. Barton, T. Roach and E. Hinds, *Atom optics with magnetic surfaces: I. Storage of cold atoms in curved 'floppy disk'*, J. Phys. B: At. Mol. Opt. Phys. (30), 647–658 (1997)

[16] I. Hughes, P. Barton, T. Roach and E. Hinds, *Atom optics with magnetic surfaces: II. Microscopic analysis of the 'floppy disk' mirror*, J. Phys. B: At. Mol. Phys. (30), 2119–2132 (1997)

[17] C. Saba, P. Barton, M. Boshier, I. Hughes, P. Rosenbusch, B. Sauer and E. Hinds, *Reconstruction of a Cold Atom Cloud by Magnetic Focusing*, Phys. Rev. Lett **82**(3), 468–471 (1999)

[18] M. Born and E. Wolf, *Principles of Optics*, Oxford:Pergamon, 6th edition (1980)

[19] D. Korsch, *Reflective optics*, Academic Press (1991)

[20] P. Molenaar, P. V. der Straten, H. Heideman and H. Metcalf, *Diagnostic technique for Zeeman-compensated atomic beam slowing: Technique and results*, Phys. Rev. A **55**(1), 605–14 (1997)

[21] M. Schiffer, M. Christ, G. Wokurka and W. Ertmer, *Magneto-optical preparation of a slow, cold and bright Ne^* atomic beam*, Opt. Commun. (134), 423–30 (1997)

[22] F. Lison, P. Schuh, D. Haubrich and D. Meschede, *High-brillance Zeeman-slowed cesium atomic beam*, Phys. Rev. A **61**(013405), 1–9 (1999)

[23] W. DeGraffenreid, J. Ramirez-Serrano, Y.-M. Liu and J. Weiner, *Continuous, dense, highly collimated sodium beam*, Rev. Sc. Instr. **71**(10), 3668–76 (2000)

[24] H. Chen and E. Riis, *Cold atomic beam from a rubidium funnel*, Appl. Phys. B (70), 665–70 (2000)

[25] E. Raab, M. Prentiss, A. Cable, S. Chu and D. Pritchard, *Trapping of Neutral Sodium Atoms with Radiation Pressure*, Phys. Rev. Lett **59**(23), 2631–34 (187)

[26] Z. Lu, K. Corwin, M. Renn, M. Anderson, E. Cornell and C. Wieman, *Low-Velocity Intense Source of Atoms from a Magneto-optical Trap*, Phys. Rev. Lett **77**(16), 3331–34 (1996)

[27] K. Dieckmann, R. Spreeuw, M. Weidemüller and J. Walraven, *Two-dimensional magneto-optical trap as a source of slow atoms*, Phys. Rev A **58**(5), 3891–95 (1998)

[28] K. Kim, K. Lee, H. Noh and W. Jhe, *Cold atomic beam produced by a conical mirror funnel*, Phys. Rev. A **64**(013402), 1–5 (2001)

[29] A. Camposeo, A. Piombini, F. Cervelli, F. Tantussi, F. Fuso and E. Arimondo, *A cold cesium atomic beam produced out of a pyramidal funnel*, Opt. Commun (200), 231–239 (2001)

[30] J. Yin, Y. Zhu and Y. Wang, *Evanescent light-wave atomic funnel: A tandem hollow-fiber, hollow-beam approach*, Phys. Rev. A **57**(3), 1957–66 (1998)

[31] P. Berthoud, A. Joyet, G. Dudle, N. Sagna and P. Thomann, *A continuous beam of slow cold cesium atoms magnetically extracted from a 2D magneto-optical trap*, Europhys. Lett **41**(2), 141–46 (1998)

[32] P. Cren, C. Roos, A. Aclan, J. Dalibard and D. Guéry-Odelin, *Loading of a cold atomic beam into a magnetic guide*, Eur. Phys. J. D (20), 107–16 (2002)

[33] J. Schoser, A. Batär, R. Löw, V. Schweikhard, A. Grabowski, Y. Ovchinnikov and T. Pfau, *Intense source of cold Rb atoms from a pure two-dimensional magneto-optical trap*, Phys. Rev. A **66**(023410), 1–10 (2002)

[34] D. Meschede and H. Metcalf, *Atomic nanofabrication: atomic deposition and lithography by laser and magnetic forces*, J. Phys. D: Appl. Phys. (36), R17–R38 (2003)

[35] E. Majorana, *Atomi Orienti in Campo Magnetico Variabile*, Nuovo Cimento **9** (1932)

[36] B. Cagnac and J. Pebay-Peyroula, *Modern Atomic Physics: Quantum Theory and its Applications*, Macmillan Physics Text (1975)

[37] N. Ramsey, *Molecular Beams*, Oxford University Press, 1985th edition (1956)

[38] D. Schroeder, *Astronomical optics*, Academic press (2000)

[39] V. Vladimirskii, *Magnetic Mirrors, Channels and Bottles for Cold Neutrons*, Soviet Physics JEPT **12**(4), 740 (1961)

[40] G. Opat, S. Wark and A. Cimmino, *Electric and Magnetic Mirrors and Gratings for Slowly Moving Neutral Atoms and Molecules*, Appl. Phys. **B54**, 396 (1992)

[41] A. Sidorov, R. McLean, W. Rowlands, D. Lau, J. Murphy, M. Walkiewcz, G. Opat and P. Hannaford, *Specular reflection of cold caesium atoms from a magnetostatic mirror*, Quantum Semiclass. Opt. (8), 713–725 (1996)

[42] F. Lison, *Atomlithographie und reflexive Atomoptik mit laserpräparierten Atomen*, Ph.D. thesis, University of Bonn (1998)

[43] E. Hinds and I. Hughes, *Magnetic atom optics: mirrors, guides, traps and chips for atoms*, J. Phys. D (32), R119–146 (1999)

[44] W. Cain, A. Payne, M. Baldwinson and R. Hempstead, *Challenges in the Practical Implementation of Perpendicular Magnetic Recording*, IEEE Transactions on Magnetics **32**(1), 97–102 (1996)

[45] R. New, R. Pease and R. White, *Lithographically patterned single-domain colbalt islands for high-density magnetic recording*, J. Magn Magn Mat. (155), 140–45 (1996)

[46] A. Sidorov, R. McLean, D. Gough, T. Davis, A. Akulshin, G. Opat and P. Hannaford, *Micron-scale magnetic structures for atom optics*, Compt. Rendus Ser. IV (2), 565–72 (2001)

[47] D. Lau, A. Sidorov, G. Opat, R. McLean, W. Rowlands and P. Hannaford, *Reflection of cold atoms from an array of current-carrying wires*, Eur. Phys. J. **D**(5), 193–199 (1999)

[48] M. Drndic, K. Johnson, J. Thywissen, M. Prentiss and R. Westervelt, *Micro-electromagnets for atom manipulation*, Appl. Phys. Lett. (72), 2906–08 (1998)

[49] M. Drndic, *Properties of microelectromagnet mirrors as reflectors of cold Rb atoms*, Phys. Rev. A **60**(5), 4012–15 (1999)

[50] K. Johnson, M. Drndic, J. Thywissen, R. Westervelt and M. Prentiss, *Atomic deflection using an adapative microelectromagnet mirror*, Phys. Rev. Lett. (81), 1137–1141 (1998)

[51] A. Hubert and R. Schäfer, *Magnetic Domains:The Analysis of Magnetic Microstructures*, Springer-Verlag: Berlin-Heidelberg (1998)

[52] P. Rosenbusch, J. Retter, B. Hall, E. Hinds, F. Lison, D. Haubrich and M. Meschede, *Reflection of cold atoms by a cobalt single crystal*, Appl. Phys. B (70), 661–663 (2000)

[53] W. Szmaja, *The thickness dependence of the magnetic domain structure in cobalt monocrystal studied by SEM*, J. Magn. Magn. Mater. (153), 215–223 (1996)

[54] B. Grieb, *Aufbau der System und Gefüge der Verbindungen von optimierten Hartmagneten auf Fe-Nd-B-Basis mit den Substituten D_y, Al, Ga, oder C*, Ph.D. thesis, University of Stuttgart (Germany) (1991)

[55] A. Sidorov, R. McLean, F. Scharberg, D. Gough, T. Davis, B. Sexton, G. Opat and P. Hannaford, *Permanent-magnet microstructures for atom optics*, Acta Phys. Pol. (33), 2137 (2002)

[56] E. Beaurepaire, J.-C. Merle, A. Daunois and J.-Y. Bigot, *Ultrafast Spin Dynamics in Ferromagnetic Nickel*, Phys. Rev. Lett **76**(22), 4250–53 (1996)

[57] R. Bertram, H. Merimeche, M. Mützel, H. Metcalf, D. Haubrich and D. Meschede, *Magnetic whispering-gallery mirror for atoms*, Phys. Rev. A **63**(053405), 1–5 (2001)

[58] W. Phillips and H. Metcalf, *Laser Deceleration of an Atomic Beam*, Phys. Rev. Lett **1**(48), 596–99 (1982)

[59] R. Watts and C. Wieman, *Manipulating atomic velocities using diode lasers.*, Opt. Lett. **11**(5), 291–293 (1986)

[60] V. Bagnato, G. Lafyatis, A. Martin, E. Raab, R. Ahmad-Bitar and D. Pritchard, *Continuous stopping and trapping of neutral atoms.*, Phys. Rev. Lett. (11), 2194 (1987)

[61] R. Swenumson and U. Even, *A continuous flow reflux oven as the source of an effusive molecular Cs beam*, Rev. Sci. Instrum **53**(4), 559–61 (1980)

[62] D. L. (Ed.), *CRC Handbook of Chemistry and Physics*, CRC Press, Boca Raton, 81th edition (2000)

[63] M. Hamilton, *An introduction to stabilized lasers*, Contemp. Phys. **30**(1), 21–33 (1989)

[64] C. Wieman and L. Hollberg, *Using diode lasers for atomic physics*, Rev. Sci. Instrum. **62**(1), 1–20 (1991)

[65] K. MacAdam, A. Steinbach and C. Wieman, *A narrow-band tunable diode laser system with grating feedback, and a saturated absorption spectrometer for Cs and Rb*, Am. J. Phys. **60**(12), 1098–1111 (1992)

[66] D. Haubrich and R. Wynands, *A modified commercial Ti:sapphire laser with 4 kHz rms linewidth*, Opt. Commun (123), 558–62 (1996)

[67] R. Wynands, *Frequenzmessung und -synthese mit Halbleiterlasern*, Ph.D. thesis, University of Munich (1992)

[68] R. Bertram, *Atomstrahlumlenkung mit Magnetbändern*, Diploma thesis, University of Bonn (2000)

[69] J. Dalibard and C. Cohen-Tannoudji, *Laser cooling below the Doppler limit by polarization gradients*, J. Opt. Soc. Am. **B**(6), 2023–45 (1989)

[70] P. Ungar, D. Weiss, E. Riis and S. Chu, *Optical molasses and multilevel atoms:theory*, J. Opt. Soc. Am. B **6**(11), 2058–71 (1989)

[71] D. Weiss, E. Riis, Y. Shevy, P. Ungar and S. Chu, *Optical molasses and multilevel atoms: experiment*, J. Opt. Soc. Am. **B**(6), 2072 (1989)

[72] B. Masterson, C. Tanner, H. Patrick and C. E. Wieman, *High-brightness, high-purity spin-polarized cesium beam*, Phys. Rev. A **47**, 2139–45 (1993)

[73] Quantegy Europa Ltd., Commerce Park, Theale, RG7 4AB, *AMPEX 398 Betacam SP Videocassettes*, (Phone:01189302208) (1998)

[74] P. Rosenbusch, *Atom Optics with an Adaptable Magnetic Reflector*, Ph.D. thesis, University of Sussex (Great-Britain) (2000)

[75] P. Hansen and J.-P. Krumme, *Magnetic and magneto-optical properties of garnet films*, Thin Solid Films (114), 69–107 (1984)

[76] BYLA GmbH, 65594 Runkel, *Byla GmbH: Datenblatt BYLAPOX 7285* (1999)

[77] T. Dresel, G.Häusler and H. Venzke, *Three dimensional sensing of rough surfaces by coherence radar*, Appl. Opt. **31**(7), 919–925 (1992)

[78] U. Poulsen and K. Mølmer, *Atomic reflection from a magnetic mirror: Beyond the adiabatic approximation*, Eur. Phys. J. D (11), 151–157 (2000)

[79] P. Lett, W. Phillips, S. Rolston, C. Tanner and C. Westbrook, *Optical molasses*, J. Opt. Soc. Am. B **6**(11), 2084–2107 (1989)

[80] A. Steane, M. Chowdhury and C. Foot, *Radiation force in the magneto-optical trap*, J.Opt.Soc.Am. B **9**(12), 2142–58 (1992)

[81] C. Townsend, N. Edwards, C. Cooper, K. Zetie, C. Foot, A. Steane, P. Szriftgiser, H. Perrin and J. Dalibard, *Phase-space density in the magneto-optical trap*, Phys. Rev. A **52**(2), 1423–39 (1995)

[82] C. Gabbanini, A. Evangelista, S. Gozzini, A. Lucchesini, A. Fioretti, J. Müller, M. Colla and E. Arimondo, *Scaling laws in magneto-optical traps*, Europhys. Lett **37**(4), 251–56 (1997)

[83] C. Monroe, W. Swann, H. Robinson and C. Wieman, *Very Cold Trapped Atoms in Vapor Cell*, Phys. Rev. Lett **65**(13), 1571–74 (1990)

[84] J. Nellessen, J. Werner and W. Ertmer, *Magneto-optical compression of a monoenergetic sodium atomic beam*, Opt. Comm. (78), 300–308 (1990)

[85] P. Rosenbusch, B. Hall, I. Hughes, C. Saba and E. Hinds, *Manipulation of cold atoms using a corrugated magnetic reflector*, Phys. Rev. A (61), 31404–1–4(R) (2000)

[86] P. Rosenbusch, B. Hall, I. Hughes, C. Saba and E. Hinds, *Reflection of cold atoms by an adaptable magnetic reflector*, Appl. Phys. B (70), 709–720 (2000)

[87] A. Goepfert, F. Lison, R. Schütze, R. Wynands, D. Haubrich and D. Meschede, *Efficient magnetic guiding and deflection of atomic beams with moderate velocities*, Appl. Phys. B (69), 217–222 (1999)

[88] F. Crompvoets, H. Bethlem, R. Jongma and G. Meijer, *A prototype storage ring for neutral molecules*, Nature (411), 174–176 (2001)

[89] J. Sauer, M. Barrett and M. Chapman, *Storage ring for neutral atoms*, Phys. Rev. Lett. **87**(27), 270401 1–4 (2001)

[90] A. Michette, *Optical systems for soft X rays*, Plenum press, New York (1986)

And at the end of the road...

This nice adventure started as soon as Prof. Meschede gave me the opportunity to join his team. I will never forget the freedom I had to manage my projects. During the last years, I have discovered this very fascinating world of quantum optics. Thanks to Prof. Klempt for undertaking the "Korreferat" task.
In a forest, there is sometimes no path and I am very grateful to Dietmar Haubrich for helping me to find a way and for explaining me how to overcome some difficulties. I appreciated his strong experimentalist skills and the fruitful discussions we had.
I shared the "Bremser"-lab with Mario Mützel for years. Thanks a lot for helping with the simulations. I will never forget his words of encouragement during the hard times. I would like to thank Martin Müller for his patience during the last months, it helped a lot to have the lasers for the last measurements. With my first and last diploma student, Ralph Bertram, we learned how to construct very smooth magnetic reflectors and we succeeded in the whispering gallery experiment up to the last breath.
Other people contributed to enhance my knowledge, especially the "single atom"- group with the very good tips as I was struggling with my first MOT, the "BEC"-group and the PM story. I enjoyed to know about the new results of the "Indium"-group, finally the indium has been cooled! Unfortunately the "dark resonance"-group left the 2nd floor and with it the best fighter against stray magnetic fields. I have not written the names of more than thirty members of the different laboratories because I fear to commit injustice by forgetting somebody.
The mechanical shop provided me important state-of-the-art elements for building my experiment. Thanks to Herrn Neff from the Institute of Physics with the realization of the design for the magnetic mirror holder.
I would like to thank the third floor with the administrative team and their continuous good mood, the previous secretary Dagmar Eichler-Becker, the new Annelise Miglo and also Fien Lathumahina and Ilona Jaschke.
Thanks to Ulrich Rasbach and Dietmar Haubrich for reading in details the manuscript.

Avant de finir ces lignes, merci à tous de près ou de loin qui ont contribué à mon épanouissement que ce soit en Allemagne, en France ou en Algérie. Une grande pensée à mon épouse Sana qui m'a énormement soutenue et a longuement patienté pendant mes dernières expériences au labo. Nous sommes prêts à poursuivre ensemble notre chemin éternel isA. Egalement un grand merci à mes parents pour l'éducation que j'ai pu apprécier malgré leurs peu de moyens. Quoique je fasse, je ne serai trop reconnaissant pour la confiance qu'ils ont placée en moi et spécialement pour les décisions importantes concernant certains tournants dans ma vie.

Thanks, merci, Danke!

An Eides Statt versichere ich, daß ich diese Arbeit selbst und ohne jede unerlaubte Hilfe angefertigt habe, daß diese oder eine ähnliche Arbeit noch keiner anderen Stelle zur Prüfung vorgelgen hat.